

EXPLORING DYNAMIC EVENTS IN THE SOLAR CORONA

A DISSERTATION SUBMITTED TO THE GRADUATE DIVISION OF THE
UNIVERSITY OF HAWAI'I AT MĀNOA IN PARTIAL FULFILLMENT OF THE
REQUIREMENTS FOR THE DEGREE OF

DOCTOR OF PHILOSOPHY

IN

ASTRONOMY

DECEMBER 2011

By

Cooper James Downs

Dissertation Committee:

Ilia Roussev, Chairperson

Noé Lugaz

Igor Sokolov

Jeffrey Kuhn

Rolf Kudritzki

Steven Businger

We certify that we have read this dissertation and that, in our opinion,
it is satisfactory in scope and quality as a dissertation for the degree of
Doctor of Philosophy in Astronomy.

DISSERTATION

COMMITTEE

Chairperson

© Copyright 2011
by
Cooper James Downs
All Rights Reserved

To my wife Allie, my mother, and my father

Acknowledgements

First and foremost I am forever grateful to Prof Ilia Roussev for giving me his unending support over the course of this project. From the beginning he took care to instill in me a sense of independence in my ideas and efforts, encouraging me to push the boundaries of my own expectations. I would also like to thank Dr Noé Lugaz for his dedication and willingness to provide detailed feedback and comments on my pursuits as well as a steady stream of the latest research notes from the broader field.

Of course none of this would have been possible without the innovative research and willing collaboration of the entire Space Weather Modeling Framework team. I am forever grateful for the confidence placed in me by Dr Igor Sokolov to open a shared channel for research and development. I would also like to graciously acknowledge Dr Bart van der Holst for our countless fruitful discussions on the inner workings of the framework and his continuing efforts to inform me of the most recent developments.

I am indebted to the remaining committee members, Prof Jeff Kuhn, Prof Rolf Kudritzki, and Prof Steven Businger who willingly gave their time and effort to support and critically evaluate this work.

I would also like to thank Dr Ofer Cohen, Dr Angelos Vourlidas, Prof Tamas Gombosi, and Dr Gábor Tóth who were instrumental in fostering useful discussions and provided invaluable feedback and comments within an collaborative atmosphere.

This work was primarily supported under the NASA Earth and Space Science Fellowship (NESSF) Program: NASA grant NESSF08-Helio08F-0007. Partial support also provided by grants: NSF ATM-0639335 (CAREER) and NASA NNX08AQ16G (LWS).

Most of the testing and model development computations were performed on the computing cluster located at the Institute for Astronomy Advanced Technology Research Center. The final simulations for Chapters 5 and 6 were conducted on high performance resources generously provided by the Hawaii Open Supercomputing Center.

SOHO EIT images courtesy of The SOHO EIT Consortium; SOHO is a project of international cooperation between ESA and NASA.

Yohkoh data courtesy of the NASA-supported Yohkoh Legacy Archive at Montana State University.

The SECCHI data used here were produced by an international consortium of the Naval Research Laboratory (USA), Lockheed Martin Solar and Astrophysics Lab (USA), NASA Goddard Space Flight Center (USA), Rutherford Appleton Laboratory (UK), University of Birmingham (UK), Max–Planck–Institut for Solar System Research (Germany), Centre Spatiale de Liège (Belgium), Institut d’Optique Théorique et Appliquée (France), and Institut d’Astrophysique Spatiale (France). This work was supported by NASA.

SDO/AIA data products are courtesy of NASA/SDO and the AIA, EVE, and HMI science teams.

Abstract

With the advent of modern computational technology it is now becoming the norm to employ detailed 3D computer models as empirical tools that directly account for the inhomogeneous nature of the Sun-Heliosphere environment. The key advantage of this approach lies in the ability to compare model results directly to observational data and to use a successful comparison (or lack thereof) to glean information on the underlying physical processes. Using extreme ultraviolet waves (EUV waves) as the overarching scientific driver, we apply this observation modeling approach to study the complex dynamics of the magnetic and thermodynamic structures that are observed in the low solar corona. Representing a highly non-trivial effort, this work includes three main scientific thrusts: an initial modeling effort and two EUV wave case-studies.

First we document the development of the new Low Corona (LC) model, a 3D time-dependent thermodynamic magnetohydrodynamic (MHD) model implemented within the Space Weather Modeling Framework (SWMF). Observation synthesis methods are integrated within the LC model, which provides the ability to compare model results directly to EUV imaging observations taken by spacecraft. The new model is then used to explore the dynamic interplay between magnetic structures and thermodynamic energy balance in the corona that is caused by coronal heating mechanisms.

With the model development complete, we investigate the nature of EUV waves in detail through two case-studies. Starting with the 2008 March 25 event, we conduct a series of numerical simulations that independently vary fundamental parameters thought to govern the physical mechanisms behind EUV waves. Through the subsequent analysis of the 3D data and comparison to observations we find evidence for both wave and non-wave mechanisms contributing to the EUV wave signal.

We conclude with a comprehensive observation and modeling analysis of the 2010 June 13 EUV wave event, which was observed by the recently launched Solar Dynamics Observatory. We use a high resolution simulation of the transient to unambiguously characterize the globally propagating front of EUV wave as a fast-mode magnetosonic wave, and use the rich set of observations to place the many other facets of the EUV transient within a unified scenario involving wave and non-wave components.

Table of Contents

Acknowledgements	ix
Abstract	xi
Table of Contents	xiii
List of Tables	xvi
List of Figures	xvii
List of Abbreviations	xx
Publications	xxi
Chapter 1: Scope of the Dissertation	1
Chapter 2: Dynamic Events in the Solar Corona	5
2.1 Our Sun	6
2.2 Magnetic Influences on The Solar Atmosphere	8
2.3 Observing the Corona in the EUV	12
2.4 Thermodynamic Considerations in the Low Corona	14
2.5 Coronal Mass Ejections	17
2.5.1 Theoretical Models of CMEs	18
2.6 EUV waves	22
2.6.1 EUV Wave Explanations/Theories	23
2.6.2 EUV Waves: Where Do We Stand?	30

Chapter 3: Magnetohydrodynamics: Overview and Applications to Space Plasmas	33
3.1 Overview of MHD	33
3.1.1 The MHD equations	34
3.2 Computational Methods for MHD	38
3.2.1 Finite Volume Methods	38
Chapter 4: The Low Corona Model	45
4.1 Introduction and Background	46
4.2 The Simulation Tool	48
4.2.1 SWMF	48
4.2.2 Including Additional Thermodynamic Terms	49
4.2.3 Boundary Conditions	54
4.2.4 Geometric Considerations	56
4.2.5 LOS image synthesis	57
4.3 Model Runs	59
4.4 Detailed Analysis	64
4.4.1 Temperature structure of low corona	64
4.4.2 Magnetic structure of low corona	65
4.4.3 EUV and Soft X-Ray comparison	66
4.4.4 Thermodynamic Comparison	67
4.5 Conclusion	72
Chapter 5: Case Study 1: 2008 March 25 EUV wave	73
5.1 Introduction and Background	74
5.2 Observations	75
5.2.1 The 2008 March 25 EUV wave event	75
5.2.2 Time-Distance limb diagrams	78
5.3 Numerical Model	80

5.3.1	Line-of-sight image synthesis	81
5.3.2	Heating Model	82
5.3.3	Eruption Model	85
5.4	Model Runs	87
5.5	Discussion	97
5.6	Conclusions	104
Chapter 6: Case Study 2: 2010 June 13 EUV Wave		107
6.1	Introduction	108
6.2	Observations of the 2010 June 13 EUV Wave Event	110
6.2.1	AIA image reduction methods	114
6.3	Numerical Model	115
6.3.1	Pre-Event Conditions	116
6.3.2	Eruption Model	120
6.4	EUV Wave Simulation Results	123
6.4.1	Comparison to EUV observations	124
6.4.2	Analysis of the 3D data	133
6.5	Discussion and Conclusions	141
6.5.1	Relevance to Proposed ‘Non-Wave’ Mechanisms	142
6.5.2	A Unified Wave/Non-Wave Picture:	145
Chapter 7: Conclusion		149
Chapter 8: Extensions and Future Work		151
Appendix A: Resolving the Transition Region in a 3D MHD Model .		157
Appendix B: Details of EUV image synthesis		163
Appendix C: Interpreting synthesized EUV images from 3D models		173
References		177

List of Tables

4.1	LC Model Heating Parameters For Runs A-D	61
5.1	Eruption Parameters for Each Model Run	88
6.1	A Comparison of EUV Imagers	110
B.1	Relevant Dynamic Timescales in the Corona	170

List of Figures

2.1	The Many Faces of the Solar Atmosphere	9
2.2	Schematic of the Solar Corona and Transition Region	10
2.3	EUV spectrum of the Solar Corona	13
2.4	EUV images of the Solar Corona	13
2.5	Thermal Budget for Heating an Hydrostatic Atmosphere	16
2.6	White Light Images of CMEs	19
2.7	The Erupting Fluxrope Model of CMEs	19
2.8	Observed Features of an EUV Wave	23
2.9	The Current Shell Model For EUV waves	27
2.10	The Reconnection Front Model For EUV waves	28
2.11	The Field Line Stretching Model for EUV waves	29
3.1	Illustration of Face Fluxes in a Finite Volume Scheme	40
3.2	Illustration of Adaptive Mesh Refinement	42
3.3	Illustration of a generalized grid transformation	43
4.1	Generalized Radial Grid for Resolving the Transition Region	57
4.2	EUV Comparison of Runs A-D to Observations	60
4.3	Effect of Active Region Heating on the Current Sheet	63
4.4	Magnetic Field and X-Ray Synthesis Comparison	65
4.5	Magnetic Topology Comparisons: PFSS, SC Model, LC Model	66

4.6	LC Model compared to the SC Model: EUV Synthesis	68
4.7	EUV Flux Comparisons for Selected Slices	69
4.8	Temperature Maps at Selected Heights	70
4.9	Density Maps at Selected Heights	71
5.1	The 2008 March 25 EUV Wave	76
5.2	Time-Distance Diagrams: Schematic and Observations	78
5.3	Time-Distance Diagram of the Northern Front	79
5.4	Temperature Response of the EUVI and XRT Instruments	83
5.5	Pre-Event Conditions for 2008 March 25: Model Compared to Observations	86
5.6	EUV Wave Evolution: Run A	90
5.7	Time-Distance Diagrams: Runs A-D	92
5.8	Time Dependent Flux Ratios: Runs A-D	95
5.9	Time-Distance Diagrams Highlighting the Northern MHD Wave . . .	99
5.10	Time-Distance Diagrams Highlighting the Secondary Enhancement .	100
5.11	Streamer Response to Perturbation: Runs A and D	101
5.12	The Fast-Magnetosonic Speed in the Vicinity of the EUV Wave . . .	103
6.1	SDO AIA Observations of the 2010 June 13 EUV Wave	112
6.2	STEREO EUVI-A Observations of the 2010 June 13 EUV Wave . . .	113
6.3	Pre-Event Conditions for 2010 June 13: Model Compared to Observations	117
6.4	Temperature Response of the EUV Filters on the AIA Instrument . .	119
6.5	Pre-Event Conditions for 2010 June 13: Tri-Color Comparison of Model and Observations	121
6.6	Magnetic Topology of AR 11079 and the Imposed Shearing Motion .	123
6.7	Tri-Color Visualization EUV Wave Transient: Model and Observations	125
6.8	Tri-Color Time-Distance Diagram of the EUV transient: Model and Observations	128

6.9	Running Flux Ratio Comparison for Selected Locations Along $r = 1.2R_{\odot}$	130
6.10	Base Flux Ratio Comparison for Selected Locations Along $r = 1.2R_{\odot}$	132
6.11	The Density Perturbation From AIA and STEREO-A Perspectives: Correlation with the Fast-Magnetosonic Speed	135
6.12	Observation and model comparison for the STEREO EUVI-A perspective	135
6.13	Phase, Velocity, and Current Snapshots of the MHD Perturbation . .	139
8.1	Polarization Synthesis for 2010 June 13	153
A.1	Length Contours for Balancing Heat Conduction and Radiative Losses	159
A.2	Length Contours for Balancing Heat Conduction and Radiative Losses	162
B.1	The EUV Spectrum as a Function of Temperature	165
B.2	Schematic Illustration of LOS integration through a 3D grid	166
B.3	Los intersection of a general spherical AMR block	167
B.4	Line Formation timescales for Fe IX 171, Fe XII 193, and Fe XIV 211Å	169
C.1	2D EUV Filter Ratio Paths: Effect of an Unresolved DEM Distribution	176
C.2	Effect of DEM Modification on LOS Synthesis Results	176

List of Abbreviations

3D three-dimensional

AR active region

AIA Atmospheric Imaging Assembly

AMR Adaptive Mesh Refinement

CME coronal mass ejection

EIT Extreme ultraviolet Imaging Telescope

EUV extreme ultraviolet

EUVI Extreme-UltraViolet Imager

EUV wave extreme ultraviolet wave

LC Low Corona

LOS line-of-sight

MHD magnetohydrodynamics

SDO Solar Dynamics Observatory

SECCHI Sun Earth Connection Coronal and Heliospheric Investigation

SOHO Solar and Heliospheric Observatory

STEREO Solar TERrestrial RELations Observatory

SXT Soft X-ray Telescope

XRT X-Ray Telescope

Publications

A list of all publications to date related to this thesis work is given below.

1. **Downs, C.**, Rousev, I. I., van der Holst, B., Lugaz, N., Sokolov, I. V. & Gombosi, T. I., *Toward a Realistic Thermodynamic Magnetohydrodynamic Model of the Global Solar Corona*, 2010, The Astrophysical Journal, 712 1219
2. **Downs, C.**, Rousev, I. I., van der Holst, B., Lugaz, N., Sokolov, I. V. & Gombosi, T. I., *Studying Extreme Ultraviolet Wave Transients with a Digital Laboratory: Direct Comparison of Extreme Ultraviolet Wave Observations to Global Magnetohydrodynamic Simulations*, 2011, The Astrophysical Journal, 728, 2
3. **Downs, C.**, Rousev, I. I., van der Holst, B., Lugaz, N., Sokolov, I. V. & Gombosi, T. I., *Understanding SDO/AIA Observations of the 2010 June 13 EUV Wave Event: Direct Insight From a Global Thermodynamic Magnetohydrodynamic Simulation*, 2011, The Astrophysical Journal, In Prep¹
4. Cohen, O., Attrill, G. D. R., Schwadron, N. A., Crooker, N. U., Owens, M. J., **Downs, C.**, & Gombosi, T. I., *Numerical simulation of the 12 May 1997 CME Event: The role of magnetic reconnection*, 2010, Journal of Geophysical Research, 115
5. Lugaz, N., **Downs, C.**, Shibata, K., Rousev, I. I., Asai, A., & Gombosi, T. I., *Numerical Investigation of a Coronal Mass Ejection from an Anemone Active Region: Reconnection and Deflection of the 2005 August 22 Eruption*, The Astrophysical Journal, 738, 127
6. Garraffo, C., Cohen, O., Drake, J. J., & **Downs, C.**, *The Effect Of Limited Spatial Resolution Of Stellar Surface Magnetic Field Maps On MHD Wind And Coronal X-Ray Emission Models*, 2011, The Astrophysical Journal, In Prep

¹This work is contained in Chapter 6 and will be submitted shortly after this draft

Chapter 1

Scope of the Dissertation

Our primary goal in this dissertation is to extend and improve a realistic model of the global three-dimensional (3D) corona and, in doing so, develop a rigorous, yet flexible tool for conducting of global simulations of dynamic events. Although this model is applicable to a number of unresolved science topics involving the corona, the primary science investigation of this dissertation is focused on the nature of extreme ultraviolet waves (EUV waves); globally propagating coronal transients observed in the EUV spectral regime. A critical component of this work is the coupled observation and modeling approach: i.e. making sure that the model results are consistent with observations (EUV and soft X-Ray images in this context), and using these results to get at the underlying physics of EUV waves. The effort can be outlined in three major research categories, namely: *Model development*, encompassing the implementation of the additional physics and considerations needed to accurately describe the dynamics of the low corona. *Data analysis*, including synthesizing observables for a handful of instruments from model data as well as creating illuminating processing methods. And *case-studies*, targeted scientific studies documenting the thorough application of the model and data processing techniques to specific EUV wave events.

Chapter 2 gives a general background of the sun, solar corona, and solar eruptions, and is intended to provide a context that frames the current issues and limitations in our understanding of EUV waves. The Sun as an astrophysical object is incredibly unique due to its proximity to us. The ability to view the magnetized Solar atmosphere with unprecedented detail is both a blessing and a curse, as the complex evolving structures that we observe so well are often quite difficult to explain with simple models or prescriptions.

Because this work features an extensive amount of modeling, it would be incomplete without a description of the fundamental equations and methods used. Chapter 3 provides a brief overview of the magnetohydrodynamics (MHD) equations and their utility to the study of space plasmas. We conclude this chapter with broad discussion of their role in 3D computer modeling methods.

The first of the three main scientific efforts, Chapter 4 documents the steps taken for the successful development and validation of the Low Corona (LC) model, a 3D thermodynamic MHD model, which is the backbone of this entire research effort. In a relevant scientific application, we use this new model to study the global implications of various coronal heating models and explore the dynamic interplay between magnetic structures and thermodynamic energy balance in the corona.

With the LC model in hand, we turn directly to the study of EUV waves in Chapter 5. Observed in detail by the STEREO-A and B spacecraft pair, the 2008 March 25 event represents a prototypical EUV wave transient and was an ideal candidate at the time for our first case-study. Using the LC model as an effective digital laboratory, we simulate the time-dependent observational signature of four different versions of a realistic solar eruption. We explore the effect of three key parameters on the resulting observational signal of the EUV transient (ambient

magnetic field, eruption strength, eruption handedness), and find evidence for both wave and non-wave elements at play.

The results of our definitive case-study are presented in Chapter 6. In 2010 we saw the launch and commissioning of a revolutionary observational tool: the Atmospheric Imaging Assembly (AIA) onboard the Solar Dynamics Observatory. Leveraging the observational capabilities of AIA towards the study of EUV waves, we perform a high resolution simulation of the 2010 June 13 event and proceed with a coupled observational and modeling analysis of the multi-faceted EUV wave signatures that are observed. In addition to finding strong evidence supporting the fast-mode wave hypothesis for globally propagating EUV wave fronts, we also document a clear separation between the wave and non-wave components. We conclude this chapter with a discussion of the implication of these results to theory of EUV waves, and provide perspective on their role within a unified framework.

In Chapter 7 we conclude with summation of the scientific results of this work and a short discussion of their broader impact.

Chapter 2

Dynamic Events in the Solar Corona

Abstract

The solar atmosphere continues to be one of the most rich and dynamic environments studied in modern astrophysics. Spanning many orders of magnitude in density and temperature while inextricably linked to the complex system of magnetic fields, the Sun displays a myriad of interesting phenomena from sunspots in the solar photosphere to coronal mass ejections (CMEs)—the most energetic events in the solar system. As an astrophysical object our Sun is most unique. The physical domains of the Solar atmosphere span a broad range of research areas from, plasma physics, the theory stellar structure, to high energy physics. At the same time, its proximity allows for an unprecedented amount of detail in observations. As our experimental sensitivity grows so does our need for theoretical models and considerations that can explain them, old paradigms must be replaced by the new and still many unanswered questions remain. In this chapter we review the fundamental properties of the Solar Corona including observations and the theoretical underpinnings of dynamic events such as CMEs and extreme ultraviolet waves (EUV waves).

2.1 Our Sun

The study of the Sun has a unique place in the field of Astronomy. In a broad sense of the universe, one that includes the veritable jungle of interesting astronomical objects such as erupting stars, black holes, super massive galaxies, and cosmic strings, the Sun is absurdly boring. One of the most common spectral types in existence, G2V, the stellar parameters describing the sun (mass, size, color, luminosity, lifetime, etc.) are completely average, middle ground in every way. The Sun, just like its billions of nearly identical relatives in our local galaxy alone, has been just about the same for four and a half billion years and will remain so for another five billion give or take. But, the catch of course, is that the Sun has one fundamental characteristic that differentiates it from every other stellar object in existence: a tiny chunk of rock in orbit *only* 150 million kilometers away, full of inquisitive people.

And it is this feature, the fact that it is so close, that makes a world of difference to the study of the Sun and its significance to us. Instead of appearing as most stars do in the galaxy, as solitary points of light with even the most technologically advanced telescopes, the Sun exhibits rich and complex features over a range of scales, scales visible to even the naked eye under the right conditions. Instead of appearing as a perfectly symmetric sphere that can be fully described with one coordinate, we observe up close the imperfections of the Sun, seeing with crystal clarity its inhomogeneities. Features like the bubbling surface that is continuously pockmarked with concentrations of magnetic field, the wisp-like extensions of the Corona and Solar Wind, and Solar Storms: dynamic bursts of material and radiation, some of which impact our own upper atmosphere. Most importantly it is these features that serve to introduce new and unique mysteries to study. It is this proximity that is one of the most paradoxical themes in the study of our nearest star: while we are treated

to an unprecedented view of the solar atmosphere afforded by front row seats from Earth, it is this view that offers up a litany of complex and dynamic astrophysical structures, which are often ambiguous in their interpretation.

Taking a tour of the Sun and Solar atmosphere, we first begin our journey at the core of the Sun. It is here, over the first $0.2 R_{\odot}$ or so that the fusion process powering the sun occurs, representing a finely tuned engine, feeding the layers above with just enough energy to support themselves against the ever present force of gravity. Then comes the radiative zone which extends out to around $0.7 R_{\odot}$ and is so named because radiative transfer is the most efficient means of transporting energy over its range of conditions. Heliosismic measurements that probe this region show that the radiative zone rotates as a solid body and it is thought to be relatively devoid of internal motions.

As we leave the radiative zone we enter the convective zone which extends out all the way to the stellar surface. At the interface between these two regions (referred to as the tachocline) the energy transfer mechanism changes abruptly as the adiabatic index of the stellar material becomes unstable to convection. This has many interesting implications for the Sun. First, because material in the convective zone is convectively unstable, it enacts a state akin to boiling water on a stove. Local fluid elements become hotter than their surroundings and expand, decreasing their density and causing buoyant rising. Under these conditions there is not enough of a restoring force to stop this rise locally, and the element will rise until it thermalizes with its surroundings at some point (a length referred to as the convective scale height). This implies that the convective zone is inherently dynamic and inhomogeneous at any one point in time; always in a state of flux. All at once fluid elements are heating, rising, cooling, and being replaced by the flows of neighboring material.

The second important feature of the convective zone is that it rotates differentially with latitude; material at the equator rotates about 25% faster than material at the poles. This creates a strong velocity shear at the tachocline and has important implications for the generation and support of magnetic fields in the Sun. At the end of the convective zone, radiation again becomes important and a boundary layer forms, the photosphere, which effectively marks the surface of the Sun and the start of the “Solar Atmosphere” we typically define it.

2.2 Magnetic Influences on The Solar Atmosphere

The Solar magnetic field is supported by a dynamo process that occurs at the interface region between the radiative zone and the convective zone (around $0.7 R_{\odot}$). Although there is not one fully complete or universally accepted model of the Solar Dynamo, the basic features of all theories invoke the plasma motions at the shear layer to induce a self sustaining dynamo cycle that continuously produces magnetic flux through electromagnetic induction. What is important for this discussion, however, is that the field produced here makes its way through the turbulent convective zone, being continuously guided by the roiling plasma motions until it encounters the solar surface. It is at this surface that the magnetic field begins to leave its indelible mark on the appearance of the Sun. Shown in Figure 2.1 are images of the Solar atmosphere at four wavelengths, which illustrate its four main regions; the photosphere, the chromosphere, the transition region, and corona. Before describing each region individually, it is important to appreciate their contrasting features. Looking at the full disk (top panels) we see that magnetic features that are more or less invisible in broadband light (left) become more and more pronounced as we transition to the corona (right). This serves to emphasize an overarching theme in the study of

the Solar Atmosphere: *The presence of magnetic fields introduces inhomogeneity and anisotropy on large and small scales!*

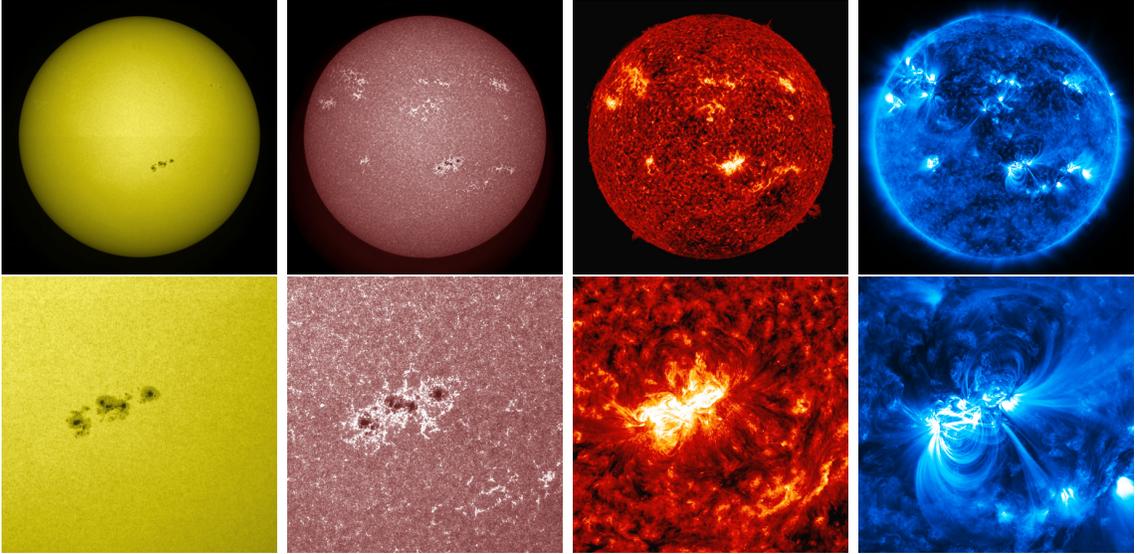


Figure 2.1: The many faces of the solar atmosphere as seen in four different wavelengths on 2011 February 14. From left to right: the photosphere in broadband visible light (centered on 4500\AA), the chromosphere seen in the ultraviolet ($\lambda \sim 1700\text{\AA}$), the upper chromosphere and transition region (He II 304\AA line), and the corona around 10^6 K (Fe IX 171\AA line). At both large and small scales, each regime exhibits unique features, feature which depend on the unique thermodynamic and magnetic conditions present there. Images captured by the Atmospheric Imaging Assembly onboard the Solar Dynamics Observatory and provided online (<http://sdowww.lmsal.com/>).

We can characterize regions of the solar atmosphere visually like in Figure 2.1, and also by tracking the following parameters: First the plasma β , which is defined as the ratio of thermal pressure to magnetic pressure ($\beta = 8\pi P_{gas}/B^2$) and characterizes the degree to which a plasma is magnetically dominated or vice versa ($\beta \gg 1$ implies plasma motions move the magnetic field along with it, while $\beta \ll 1$ implies that plasma is confined to move *along* the magnetic field). And second the thermodynamic parameters: the electron temperature, T_e , and number density, n_e as a function of height above the photosphere. This is shown qualitatively for a typical parameter range in Figure 2.2 (adapted from (Aschwanden 2004)).

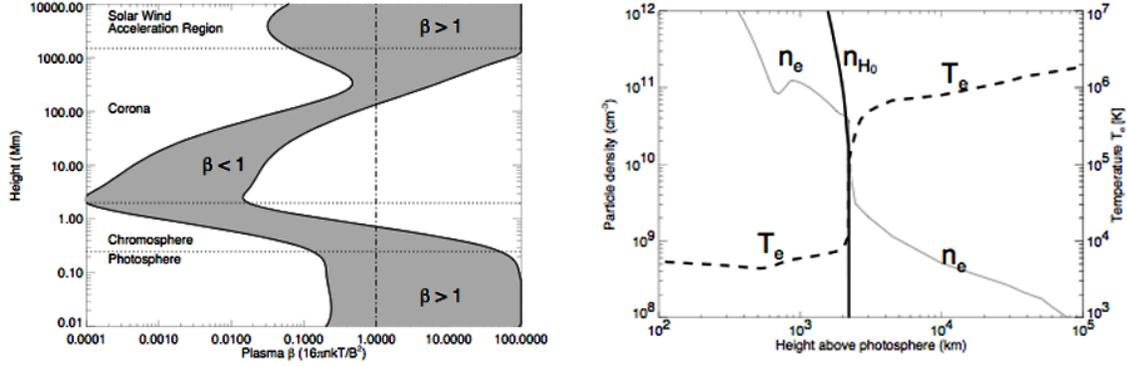


Figure 2.2: Left: Qualitative dependence of the plasma β with height in the Solar atmosphere. Right: Qualitative dependence of electron density and temperature with height above the photosphere. Note the step drop in density and sharp increase in temperature that marks the transition region from the Chromosphere to Corona. Figures adapted from Chapter 1 of Aschwanden (2004).

In the photosphere (Figure 2.1 left panels), where the thermal pressure is still quite large compared to the magnetic pressure (high β), only the strongest fields penetrate the surface and form sunspots (groups of sunspots are referred to as active regions (ARs)). Smaller concentrations of magnetic field move with the roiling convective motions and are channeled into the interface regions between the convective bubbles. When studying the magnetic field of structures beyond the corona, the photosphere forms an effective boundary condition, channeling the base (footpoints) of the magnetic field along this surface.

As we move out further we arrive at the chromosphere (left-middle panels). Here the temperature rises slightly to the tens of thousands of Kelvin, due mainly to radiative processes as the density falls off at its characteristic gravitational scale height. The combination of falling density and higher ionization fraction as the temperature rises implies that the magnetic field becomes more and more a player in the dynamics that we observe. Observational consequences are seen as the extended bright regions known as ‘plages’ which indicate regions of enhanced temperature and

density channeled by the magnetic field. Note that small scale pockets of activity are now visible all over the surface (unlike the visible photosphere).

With the atmosphere continuing its inexorable drop in density, we soon arrive at the thin layer known as the transition region, marking (as its name suggests) the transition between the cool temperatures of the chromosphere and the extreme temperatures of the solar corona (right-middle panels). Almost fully magnetically dominated now, we see a carpet of sharply contrasted structures forming dark and bright channels on larger scales than before. This highly dynamic region is subject to continuous change, perturbed by magnetized flows from below and by the heat conducted down from above.

Finally we arrive at the Solar Corona, which makes up the outermost atmosphere of the Sun (right panels). Most striking in comparison to the lower regions are the extended wisp-like structures, structures that curve and arc at the whim of the solar magnetic field. The three most defining characteristics of the corona are that of an extremely hot, highly rarefied, and magnetized plasma. To an extremely good approximation this dictates that material and energy are confined to flow along the direction of the space-filling magnetic field, providing a new twist on the effect of gravitational stratification compared to a classical atmosphere model. Forever lost is the ability to describe the collective structure of the corona with a single atmospheric model, instead each individual strand of plasma obeys its own set of rules, rules based on the local set of dynamic and thermodynamic drivers along the loop defining its magnetic connectivity.

The corona also extends into interplanetary space, its flow along open magnetic channels eventually becoming what is known as the Solar Wind. Somewhat perplexing at the outset, it was shown in a seminal paper by Parker (1958) that the corona cannot be in hydrostatic equilibrium, but must instead achieve large, supersonic

outflow velocities (500 to 1500 km/s) within a few solar-radii to be dynamically stable (primarily a result of the high thermal conductivity and the falloff of gravitational potential).

As the solar wind flows outward its density falls off more slowly than the magnetic field ($\sim 1/r^2$ vs $\sim 1/r^3$) and the plasma becomes fluid dominated again (high β). Now the Solar Magnetic field takes the role of being carried along with the flow eventually sharing its indelible coronal imprint as it passes Earth's orbit and continues onward.

2.3 Observing the Corona in the EUV

Due naturally to its temperature range in the millions of Kelvin, coronal plasma emits primarily in the EUV and soft X-ray regime. Unlike the photosphere, where the majority of radiative energy is output in the form of broadband blackbody radiation, most of the radiative energy of the corona is concentrated in the peaks of optically thin emission lines. This can be seen clearly by examining the spectral features of the sun in the EUV shown in Figure 2.3.

Because the formation and strength of emission lines depends strongly on the local thermodynamic properties of the emitting plasma, specific EUV emission lines (e.g. the commonly imaged Fe 171, 195, and 284Å lines) provide natural tracers of material at distinct temperature ranges and are used as a probe of the thermodynamic state of the corona. To give a visual sense of the contrast between different emission lines, images of the most commonly imaged EUV spectral lines as well as soft X-Rays are shown in Figure 2.4. Each bandpass filter is observing the same optically thin density structures, but starkly different features are seen depending on the local temperature characteristics of the particular region. The relatively cool extended coronal hole becomes more contrasted as we go up in temperature (left to right) while at the

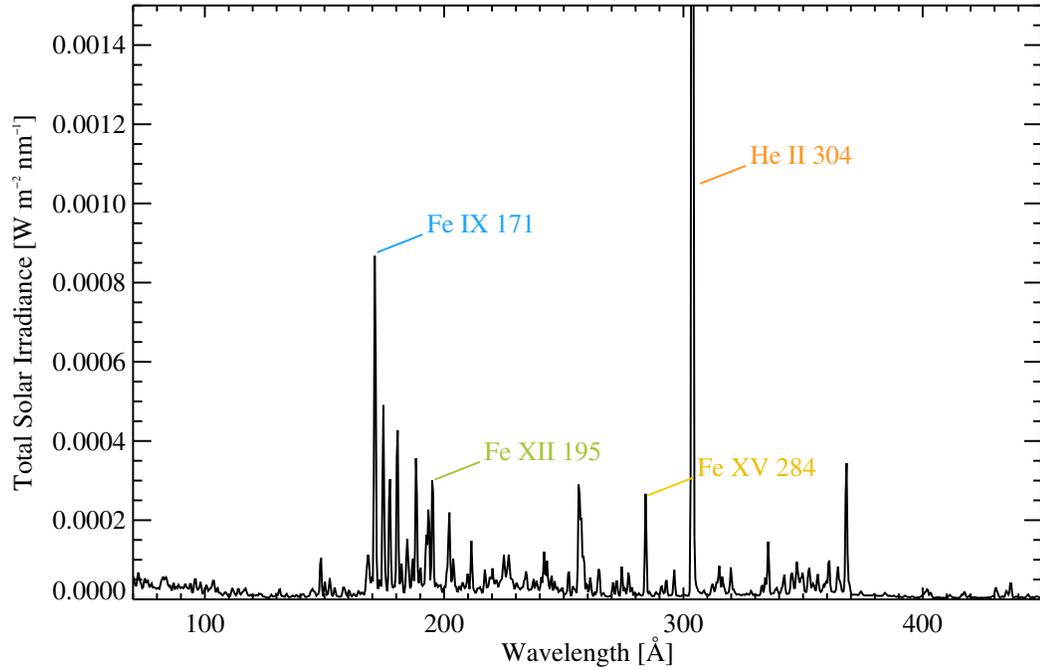


Figure 2.3: Total EUV irradiance spectrum of the sun in the for 2010 June 13. Marked are some commonly imaged emission lines, Fe IX 171Å (Blue), Fe XII 193Å (Green), Fe XV 284Å (Yellow), and He II 304Å (Red). Data from the EVE experiment (Eparvier et al. 2004) obtained from the Level 3 merged spectra provided by the EVE team.

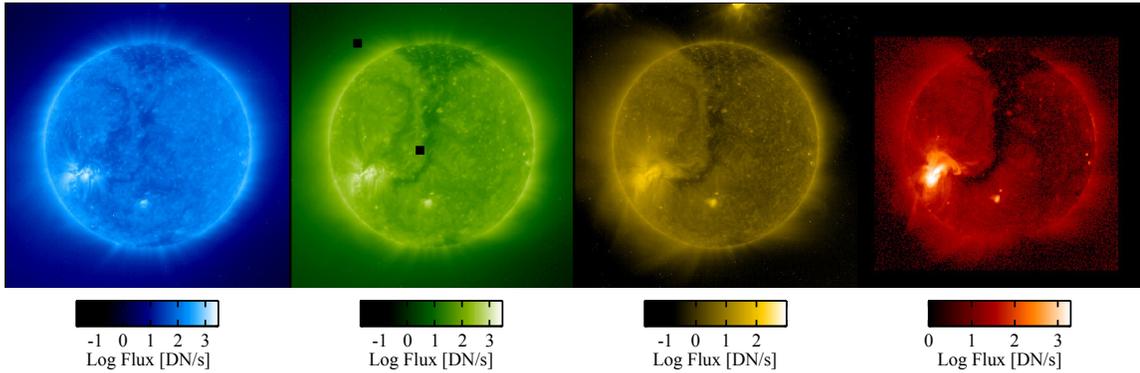


Figure 2.4: The Solar Corona as seen in multiple EUV filters and Soft X-Rays on 1996 Aug 27. This filter sequence shows how the appearance of the corona changes depending on the temperature of formation of a given emission line or bandpass. From left to right SOHO EIT 171Å, 195Å, 284Å filters, and SXT AlMg composite filter. The temperature sensitivity of each line features a somewhat broad (~ 0.3 MK) width approximately centered on 1.0, 1.4, 2.0 MK respectively, while the SXT AlMg filter is most responsive to temperatures above 2.0 MK.

same time hot plasma in the proximity of the active region becomes comparatively brighter. Additionally, because coronal loops are largely thermally isolated due to the low plasma β and field-aligned thermal conduction, EUV spectral lines provide a key tracer for the underlying magnetic field structure and geometry, especially in dense closed-field active regions (e.g. the loop structures seen at high resolution in the bottom right panel of Figure 2.1).

The extremely low density (hence optically thin nature of the emission lines) makes the life of the astrophysicist studying the corona quite different than that one studying traditional stellar atmospheres dominated by optically thick radiative transfer. Being optically thin for all but a small majority of cases (e.g. extended prominence material), this means that every viewer line-of-sight of sight (LOS) that passes through the corona is observing the entire range of material emission along it, rather than a specific point in 3D space. This fundamentally blurs both the 3D spatial information and thermodynamic information that is contained in the viewing angle, and makes for the unfortunate fact that interpreting EUV observations (particularly those of dynamic events) becomes quite difficult. Of course spectroscopic studies, ones where the entire spectrum along a LOS is resolved, can help tremendously for certain aspects, but the trade-off is a significant loss in spatial and temporal resolution, which is often required when studying solar eruptions.

2.4 Thermodynamic Considerations in the Low Corona

The Solar Corona is hot, real hot in fact, routinely exhibiting average temperatures between 1 – 2 million degrees Kelvin in the quiescent corona, a puzzling condition

considering the surface of the sun just below is nearly a thousand times cooler. Sometimes referred to as the ‘holy-grail of Solar Physics’ the question of just physically how the corona attains these high temperatures has remained the subject of stark debate ever since it was posed over five decades ago. The competing theories can be roughly broken down into two classes:

- *Reconnection Processes*: Mechanisms involving the dissipation of magnetic energy at the base of the corona and transition region. Building upon the original framework described by (Parker 1972), these models typically invoke the churning motions of the photosphere to twist and braid the vertical field extending into the corona until it must simplify its topology, releasing energy (e.g. Low (2010)).
- *Wave Processes*: A competing class of theories involving the dissipation of magnetic wave energy flowing up from below through a variety of wave-particle or turbulence mechanisms. Wave processes have long been used to accurately describe the properties of the solar wind, and their application towards the heating of the corona has recently gained tremendous popularity due to improved observational and theoretical techniques (e.g. De Pontieu et al. (2007); Cranmer (2010); McIntosh et al. (2011)).

It is far from the goal of this work to solve this particular physical origin mystery however. What is relevant for our purposes is the *resulting effect* that the distribution of coronal heating has on structures that we observe in the corona. If one assumes that coronal heating exists on some level (as it most certainly does!) then the physical implication of an eventually hot corona is not surprising.

This can be outlined with the following simple thermodynamic argument illustrated in Figure 2.5: The hydrostatic approximation for an isothermal

chromosphere at $T=2 \times 10^4$ K gives exponential falloff as a function of height. Because of the relatively short pressure scale height at these temperatures, $h_0 \approx 1200$ km, the thermal energy content, nkT (black line), falls quickly with distance compared to coronal scales ($1R_\odot = 6.96 \times 10^5$ km). If one assumes a heating mechanism is present with some characteristic energy deposition, say $\approx 10^{-5}$ ergs $\text{cm}^{-3} \text{s}^{-1}$, a lower limit for heating near the base of the quiet corona (dotted line), then this term will eventually dominate over a relatively short distance. This eventual reversal will lead to an increased temperature, increasing the scale-height, with the system eventually settling on coronal conditions where the long-scale height and high heat conductivity allows for the slow transition to solar wind outflow that is observed.

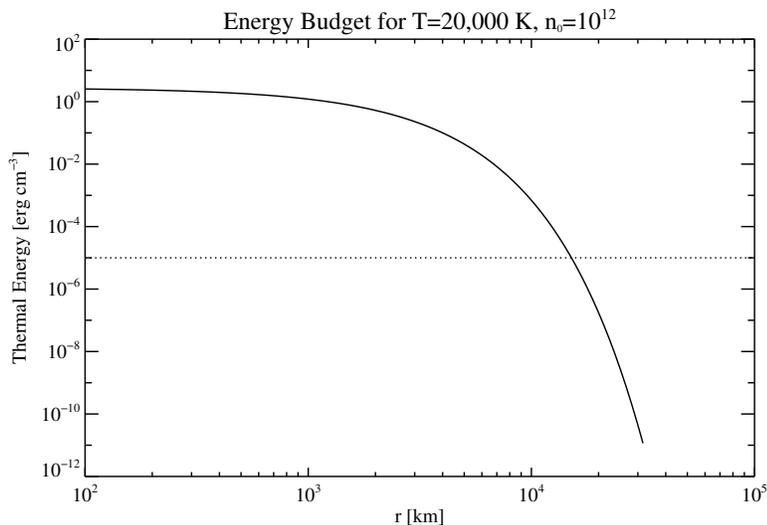


Figure 2.5: A simplified thermodynamic argument for the formation of a hot Corona. Assuming a hydrostatic, plane-parallel atmosphere at $T = 2 \times 10^4$ K, $n_e = 10^{12} \text{ cm}^{-3}$, the density (black line) falls quickly with distance compared to coronal scales. The heating timescale for a fixed volumetric heating rate ($\approx 10^{-5} \text{ ergs cm}^{-3} \text{ s}^{-1}$, dotted line) will be unimportant at the base but will soon come to dominate.

Of course the dynamics are ultimately more complex, but the point remains that given *some* heating mechanism present in a cool atmosphere, a corona is likely to form in some fashion (barring strong stellar outflows of course). It is however

the specific details of this mechanism (i.e. its strength and distribution across the magnetic atmosphere) that will determine the resulting stratification of features that we observe.

Furthermore, coronal heating does not exist on its own in a thermodynamic vacuum. Its heating effects are mediated and balanced mainly by two thermodynamic processes: radiative losses (energy sink) and electron heat conduction (energy distributor). These three energy terms that work in tandem to generate the myriad of structures observed in the corona. For a given field line or loop, concentrated heating near the base and along the loop heats the material to high temperatures. Electron heat conduction acts as an energy distributor, conducting thermal heat flux efficiently along the loop, working to make the coronal portion largely isothermal. Radiative losses act as an energy sink, mediating the heat input (conductive flux or coronal heating), which, depending on the stability conditions, sometimes allows for steady dynamic equilibrium (typically for hotter and longer loops), or sometimes ensuring unstable collapse (often for short cool loops). Furthermore, because the strong magnetic field enforces energy to flow along rather than across field lines, this permits hot and cool loops to exist nearly co-spatially in the corona, each loop being a relatively independent atmosphere reacting to the local heating conditions near its base. It is the combination of balance between these thermodynamic terms and the strong anisotropy and inhomogeneity introduced by the magnetic field, that make the solar corona such a rich and unique regime of study.

2.5 Coronal Mass Ejections

With the basic properties of the Corona established, we turn to the large-scale ubiquitous transient events that are observed there: Coronal Mass Ejections (CMEs).

Commonly referred to as ‘Solar eruptions’ due to their propensity to spew coronal material at high speeds throughout the solar system, CMEs are the single-most powerful manifestation of the energy contained in the magnetic fields of the corona.

Spanning many orders of magnitude in the relevant magneto-hydrodynamic parameters, CMEs convert inordinate amounts of magnetic energy (10^{31-32} ergs) into bulk motion, thermal energy, and energetic particles. The dynamic properties of CMEs vary significantly from event to event, with CMEs typically traveling between 200 – 2500 km/s while releasing large amounts of solar material ($\sim 10^{16-17}$ g) and magnetic flux ($\sim 10^{21-23}$ Mx) into the solar system (Gosling et al. 1990). A sense of their geometric scale and extended features can be gleaned from coronagraph images that observe the corona at large distances off of the limb shown in Figure 2.6. Most directly relevant to us is that the scale of CMEs becomes quite significant as they propagate outwards, effectively plowing through large volumes of the interplanetary medium. This also implies that CMEs directed towards Earth have a high chances of interacting with the Earth’s Magnetosphere (which they do regularly!).

2.5.1 Theoretical Models of CMEs

The study of CMEs and their physical mechanisms remains as one of the most scientifically rich and exciting fields of Solar Astrophysics. Ever since the legendary observation of an extreme event by Lord Richard Carrington in 1859, we have sought to understand their physical nature, and many questions remain. For a clear and thorough review of CMEs and their mechanisms please see the recent review by Chen (2011).

To put them in simplest terms CME models look to turn a stable magnetic equilibrium into a catastrophically unstable one. This typically involves finding a

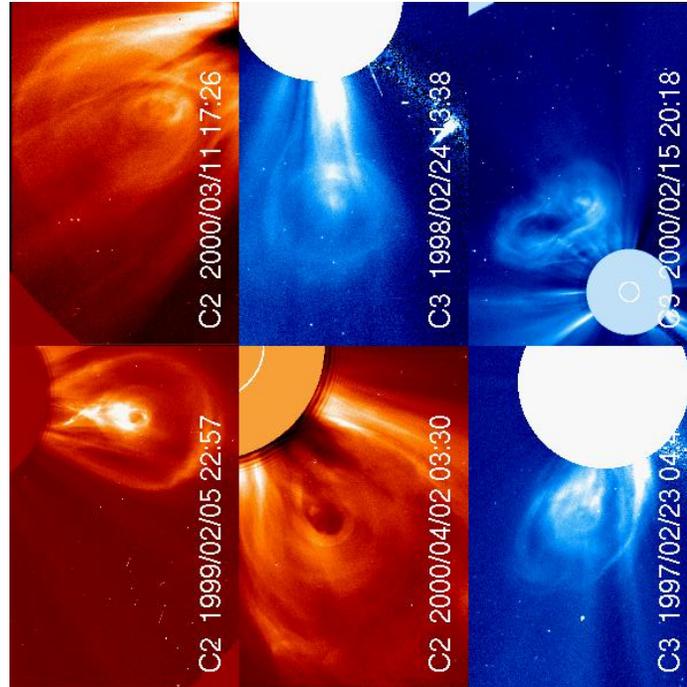


Figure 2.6: Examples of CME eruptions captured by the LASCO C2 and C3 coronagraphs aboard the SOHO satellite. The bright features are created by the enhanced density of the CMEs internal structure, which scatter more visible light than the surrounding solar wind. A sense of geometric scale is from the inner white circular line, which represents the size of the Sun. Images made available by the SOHO science team <http://sohowww.nascom.nasa.gov/>.

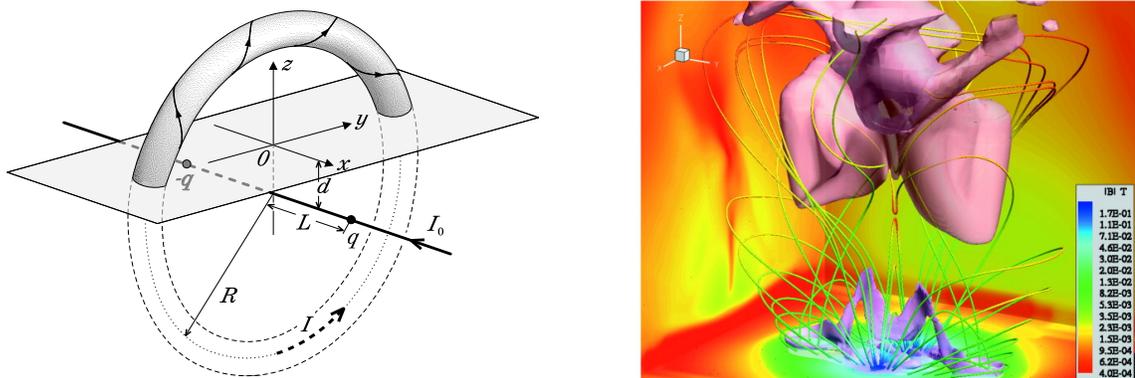


Figure 2.7: *Left:* figure from Titov & Démoulin (1999) showing an analytic model for an unstable flux-rope configuration. The twisted appearance is generated from a line current, a pair of magnetic charges (polarity centers) and current along the flux tube itself. *Right:* figure from Roussev et al. (2003a), showing the subsequent eruption of this flux rope within a 3D MHD model. The evolving configuration undergoes reconnection below and accelerates plasma outwards.

configuration that possesses a balance point between two competing forces (magnetic pressure, gravity, and/or magnetic tension) and finding condition that admits a runaway eruption. This process almost universally involves magnetic reconnection, which provides a mechanism to change magnetic topology (field lines changing their connectivity) and to quickly convert excess potential energy contained in the magnetic field into other forms of energy (i.e. the kinetic energy of the bulk CME, thermal heating, accelerated particles, etc.).

The simplest class of models that achieves the catastrophic eruption goal is that of a kink or torus unstable twisted flux-rope. This is illustrated graphically in Figure 2.7 both for an analytic out-of-equilibrium model (Titov & Démoulin (1999), left) and for a numerical implementation of this model that studied the eruption characteristics (Roussev et al. (2003a), right). Theoretical models for flux-rope eruptions come in many incarnations and flavors (e.g. Amari et al. (1999); Olmedo & Zhang (2010); Aulanier et al. (2010)) but all involve the basic features of a bipolar region formed by an emerged flux tube whose buoyancy is suspended by the surrounding coronal magnetic field. The extent to when the twist is realized before or after emergence varies between models, but typically the twist is realized through shearing motions in the photosphere (e.g. Manchester et al. (2004); Roussev et al. (2007); Aulanier et al. (2010)) and eventually causes the crossing point to catastrophic instability.

A twisted flux-rope topology is not so unrealistic either. Magnetic field generated by the dynamo at the tachocline must make it up to the solar surface and twisted flux bundles are expected to form (e.g. Fan (2008)). As field rises, solar rotation and the churning turbulent motions of the convection zone do two things: First, like oil and water, the gas pressure dominated plasma motions cause the magnetic field to be confined in relatively thin, intense channels, forming what is known as a flux-tube or flux-rope (since it has some finite width/radius). Second large scale

shear flows imposed by differential rotation and convection wind up the field along its axis, the twist often enabling the kink instability (unbalanced magnetic tension) causing portions to rise. On some level, the polarity centers of all sunspots and active regions are formed this way, however, it is the *extent* to which a flux-tube is twisted as it emerges from the surface that can differentiate its appearance and behavior significantly. The turbulent motions of the convective zone can easily break down all or parts of an emerging flux-tube, giving the often mottled structure of active regions or the appearance of unipolar sunspots when the other polarity has become dispersed into smaller scale structures.

CME models become more complicated when more polarities are involved. The famous breakout model (Antiochos et al. 1999) uses the interaction between a sheared arcade and the large-scale dipole component of the sun to generate a flux-rope *during* the eruption process (as opposed to before for a simple flux-rope). However, for our purposes the many theories of coronal mass ejections boils down to the same fundamental concept: *collective motion of the strong magnetic field regions at the base of the corona stress and perturb the delicate equilibrium above, perturbations which may ultimately lead to the spectacular eruptions that we observe as CMEs.*

2.6 EUV waves

Now that the broad discussion of CMEs is complete, we can finally turn to the primary science driver of this dissertation: *the study and interpretation of large-scale coronal transients known as EUV waves*. Originally coined ‘EIT waves’ (Moses et al. 1997) because they were first observed by the Extreme ultraviolet Imaging Telescope (EIT) (Delaboudinière et al. 1995) onboard the Solar and Heliospheric Observatory (SOHO) spacecraft¹, they are characterized by a diffuse rim of enhanced EUV emission expanding isotropically outward from an eruption site located within a coronal active region. This characteristic behavior is seen in Figure 2.8, which show a sequence of running flux difference images of an EUV wave recorded from two viewing angles by the STEREO A and B spacecraft (Patsourakos et al. 2009). One of the most interesting observable features of EUV waves is their global extent: observed to propagate large distances away from the eruption site in a short period of time, often covering the transverse distance of the observable solar disk or more in under an hour. Additionally, their isotropic nature is fully three-dimensional, creating a hemispherical or ‘dome-shape’ when observed off of the solar limb (Veronig et al. 2010). When they are observed, EUV waves can always be associated with a CME event and the relative intensity of the wave is correlated with the strength of the CME (Biesecker et al. 2002), though the converse is not true (not all CMEs generate EUV waves). Early observations of EUV waves also found that they are occasionally spatially and temporally related to Moreton waves in the chromosphere (Khan & Aurass 2002), which suggested a possible relation between the two. Additionally, shocks formed by EUV waves (when propagation exceeds the local magnetosonic

¹For clarity in the ensuing discussion, we choose to adopt the Cohen et al. (2009) convention of referring to these phenomena as ‘EUV waves’, a general term, one which naturally includes observations from the modern generation of EUV imagers, rather than the conventional term “EIT waves”; a specific reference to the EIT instrument

speeds) can provide an acceleration mechanism for SEPs and associated radio bursts as they travel away from the eruption site (Klassen et al. 2000; Ma et al. 2011; Kozarev et al. 2011).

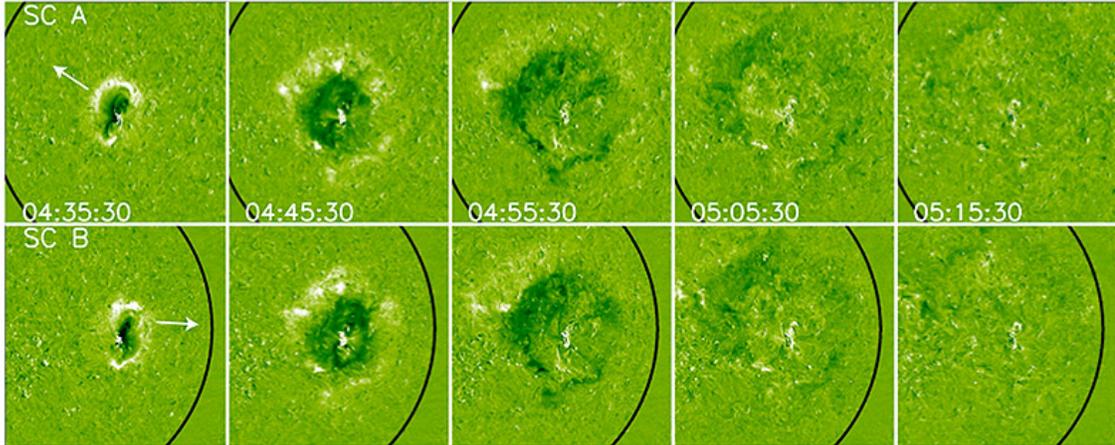


Figure 2.8: A prototypical EUV wave event observed by the STEREO A and B spacecraft on 7 December 2007. The false color running flux difference images show an expanding EUV enhancement propagating nearly isotropically away from the erupting source region. Figure reproduced from (Patsourakos et al. 2009).

2.6.1 EUV Wave Explanations/Theories

One of the most compelling aspects of EUV waves, is that there is no universal consensus on a physical explanation for the large-scale propagating front². Although the exact number of scenarios differs depending on who you ask, they can be broken down into two main groups: (i) MHD waves and (ii) non-wave/non-linear mechanisms (though some theories invoke combinations of the two). We summarize the main aspects of each here, particularly those relevant to the research conducted in this

²In reference to an idiosyncratic convention of the study of EUV waves, we wish to make clear that the terminology “EUV wave” is universally adopted by the community even though not all members believe that it is indeed a wave. In discussing the ensuing theories, please note that “EUV wave” refers to the bright, large-scale perturbation and does not imply judgment that this is necessary a physical wave.

project. For more details please see recent reviews by (Wills-Davey & Attrill 2009; Gallagher & Long 2010; Chen 2011).

EUV Waves as Fast Mode MHD Waves

The most popular interpretation of EUV waves is that they represent coherent fast-magnetosonic wavefronts propagating in the coronal plasma. Originally postulated long before observations existed (Uchida 1968), many modern observational studies support this view (e.g. Thompson et al. (1999); Wu et al. (2001); Warmuth et al. (2005); Long et al. (2008); Veronig et al. (2008); Patsourakos et al. (2009); Veronig et al. (2010)). Just like sound waves propagate in air, a magnetized plasma also admits wave propagation. However, due to the anisotropy introduced by the presence of a magnetic field, there are three distinct wave modes that are admitted (rather than just longitudinal waves in the case of air). The modes include an incompressible wave that propagates strictly parallel to the magnetic field, the famous Alfvén Wave (Alfvén 1942), as well as two compressible modes known as the Slow-Mode and Fast-Mode Magnetoacoustic Waves. The nature of these waves is discussed in more detail in Chapters 5 and 6 but the most important property to note here is that fast-mode magnetosonic waves are the *only* MHD wave mode that can propagate easily in directions perpendicular to the magnetic field. This means that fast-mode waves can easily satisfy the ‘global extent’ requirement set by the observed EUV wave fronts. Additionally, just like ordinary sound waves, fast-mode waves propagate at a characteristic sound speed that depends on the local conditions of the medium (magnetic field strength, orientation, density, and temperature in this case).

The properties of fast-mode waves in the corona make them an entirely logical explanation for EUV waves. First, the typical propagation speed of an EUV wave is around $200 - 400 \text{ km s}^{-1}$, which is plausibly of the order of the fast magnetosonic

speed in the quiescent closed field regions of the corona in which they are observed to propagate (estimates of fast-mode speeds typically range between 200 – 600 km/s depending on the assumption of average quiet sun field strength, temperature, and mass density). The simple fact that the average fast-magnetosonic speed is around the same speed as the average speed of EUV wave fronts is quite appealing indeed. For some events this is a curse however, as the dependence on local sound speed also sets *a minimum* propagation speed for EUV waves as fast mode waves. The plasma temperature alone in the quiet corona sets a floor of 150 – 200 km/s and a few events have been reported to move slower than this (Wills-Davey et al. 2007). This requirement is also called into question by Yang & Chen (2010), who find a negative correlation of magnetic field strength with derived EUV wave speeds for two events, which is opposite to the expected result for a purely fast-mode MHD wave.

The wave nature of EUV waves is also often invoked to explain the reflection of these fronts off of regions with large gradients in magnetosonic speed, such as interface between quiet-Sun and open field regions (coronal holes) with large ambient values of c_f (Gopalswamy et al. 2009; Schmidt & Ofman 2010). Also a recent study involving simultaneous observations of an EUV wave from multiple locations (Patsourakos & Vourlidas 2009) offered the observed lack of co-spatiality of the erupting CME cavity and EUV wave transient as further confirmation of the fast-mode wave scenario.

Non-Wave Theories of EUV waves

However, the fast-mode wave interpretation is not the only game in town. One of the major difficulties in interpreting EUV waves is the fact that their signature is simultaneously coupled with the dynamic evolution of the structure of the corona (as must be the case for CMEs). This is further limited due to inherent image projection effects when observing the three dimensional structure of the event (Ma

et al. 2009). As instability sets in during a CME, interaction of the erupting field with the overlying flux systems and the impingement of expanding plasma on the surrounding environment are necessary by-products. This zeroth order change of the environment complicates the interpretation of these transients as simply a linear first order transient (fast-mode wave) over the background field (Attrill et al. 2009). For example, observations of the 2007-May-19 EUV wave transient produced what was supposedly a strong case for fast-mode wave reflection (Gopalswamy et al. 2009). However a year later the same set of images was processed using methods that highlight the zero order changes in the corona, and the case argued against the wave hypothesis (Attrill 2010)! The main categories of non-wave theories are discussed below:

The Current shell Model

The first relevant non-wave theory to be discussed is the ‘current-shell’ model originally proposed by Delannée et al. (2008). Employing an idealized erupting flux rope, this model correlates the large-scale evolution of the non-linear current shell formed by the CME to the hemispherical ‘dome-shape’ of the EUV wave (see diagram in Figure 2.9). Representing the contribution of the changing magnetic field in the induction equation (Equation 3.4), this model utilizes the fact that localized currents are expected to be formed as a result of the magnetic evolution of an erupting flux-rope. These currents are then thought to generate an observable EUV transient by heating the coronal plasma as they dissipate. This model is attractive because it provides an explanation both the large-scale isotropic extent of EUV waves (yellow surface), and for the more rare ‘S-wave’ secondary features (red surfaces) that are observed for some intense EUV wave events (Biesecker et al. 2002).

A major difficulty of this model however is the fact that it requires that the CME/coronal arcade possess physical extents of a solar radii or more relatively close to the surface. In the case of both Delannée et al. (2008) and the most recent application of this model (Schrijver et al. 2011) the size of the idealized flux-rope model was simply dimensionalized to match the extent of the EUV wave. For more realistic CME models however, the sheer size requirement that the CME extend to large transverse scales in the low corona presents a significant physical challenge.

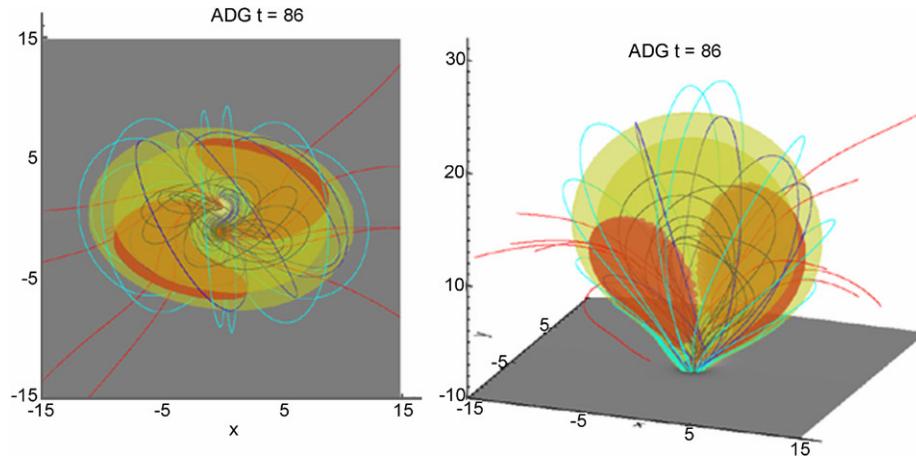


Figure 2.9: Diagram illustrating the appearance of the expanding current shell from (Delannée et al. 2008). In this scenario a large erupting flux rope CME produces an hemispherical ‘shell’ of MHD currents (yellow and red surfaces) that heat the coronal plasma as it expands outward. The projection of this structure is thought to produce the EUV wave appearance.

The Reconnection Front Model

This explanation explicitly invokes magnetic reconnection as a means of producing the EUV wave transient, and is shown schematically in Figure 2.10. Initially proposed by Attrill et al. (2007a), this model posits that successive reconnection events occur between favorably aligned quiet-Sun field and the legs of the expanding magnetic structures of the CME as it erupts. These successive reconnection events dissipate

magnetic energy, conducting thermal energy upwards along connected magnetic field lines, ultimately creating the collective front that is observed (Attrill et al. 2007b). Reconnection is an ideal candidate for explaining the apparent heating of the front visible in multi-wavelength studies (Attrill et al. 2009; Dai et al. 2010; Downs et al. 2011). Like the current shell model however, the primary drawback of this interpretation is the requirement that the physical extent of the CME span large transverse distances relatively low in the solar corona.

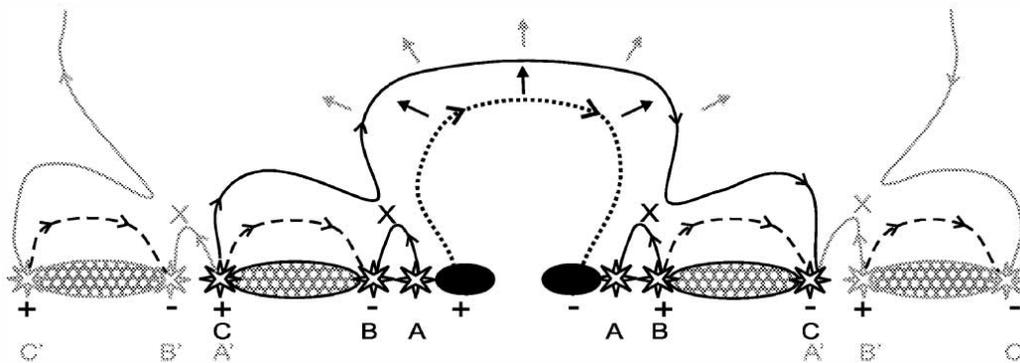


Figure 2.10: Illustration of the reconnection front model reproduced from Attrill et al. (2007a). As a CME erupts it impinges on the surrounding magnetic arcade. This causes the expanding CME arcade to reconnect with small scale quiet sun loops that are favorably oriented to this structure (marked by X's). This is thought to both enable CME expansion and generate the hot bright EUV wave front.

The Fieldline Stretching Model

One model that attempts to combine both wave and non-wave mechanisms is the ‘field-line stretching’ model originally proposed by Chen et al. (2002) and subsequently studied by Chen et al. (2005); Wang et al. (2009); Chen, F. et al. (2011) (among others). In an effort to unify coronal signatures with Moreton waves (fast-mode waves traveling at high speeds in the chromosphere) the field-line stretching model proposes that a coronal Moreton wave (a.k.a. a fast-mode wave) is launched during the eruption and propagates freely in all directions under coronal conditions. The EUV signature

however is not produced by this the coronal Moreton wave (argued to be relatively undetectable) and instead it is the subsequent expansion of the CME and surrounding of the arcade that creates this signature. The enhanced emission produced by the ‘stretching’ of field pulled along with the CME and its subsequent compression on the surrounding regions. It is this key physical distinction that differentiates the field-line stretching model from the more common fast-mode wave theories: it is not the fast-mode wave itself that produces the emission but the subsequent relaxation of the corona in response to the CME. This is also a distinct interpretation from the current shell model (Delannée et al. 2008) both because it invokes a precursor wave and because the EUV signal is thought to be produced primarily by plasma *compression* and not direct heating by field-aligned magnetic currents (though both must exist at some level).

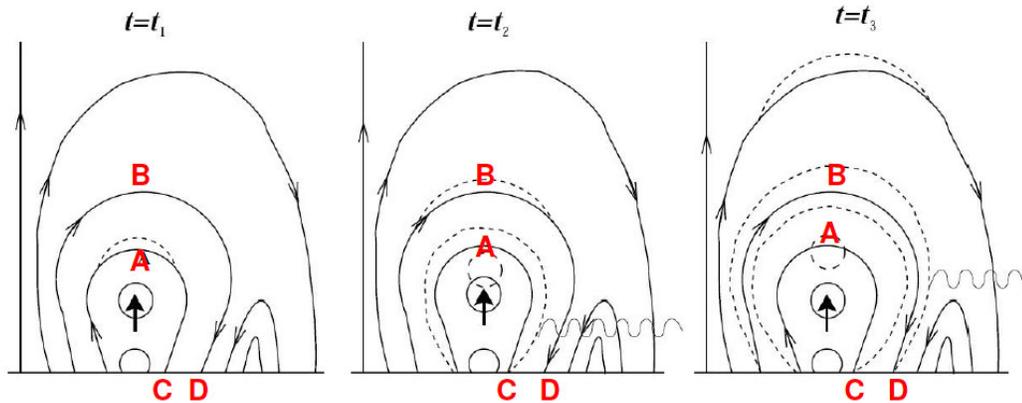


Figure 2.11: Diagram from Chen et al. (2002) showing the field line stretching model for EUV waves. In this model the coronal component of the chromospheric moreton wave (a fast mode wave) propagates ahead of the EUV wave disturbance. The observable “front” of the EUV wave is the result of field lines in the erupting arcade stretching/compressing (dotted lines) which enhances the local density and temperature, causing increased EUV emission (squiggly lines).

Slow-Mode Models

Some other models invoke non-linear MHD modes (e.g. the slow mode shock component of a Moreton wave (Wang et al. 2009) and the slow-mode soliton wave described by Wills-Davey et al. (2007)) to explain the diffuse front of EUV waves. The unusual nature of the slow-mode wave and its non-linear mechanisms is also their downfall however, as a physical demonstration of the utility is usually extremely dependent on finely tuned set of conditions (which the corona is loath to provide).

Combined Models

Often times when studying complex phenomena, competing theories may both contain pieces of the puzzle. Sure enough, evidence combining these elements has been recently found observationally (Patsourakos & Vourlidas 2009; Patsourakos et al. 2010b) and in numerical experiments that resolve a fast-mode wave component and a component related to coronal restructuring due to the CME itself (Cohen et al. 2009). This particular concept is addressed extensively in this work.

2.6.2 EUV Waves: Where Do We Stand?

As will become evident throughout this work, it is the authors interpretation that much of the EUV wave controversy stems from the fact that up until recently it has been difficult to both interpret EUV observations (many ambiguities) and to create models that can be directly applied to observed events. Up until the launch of the Solar Dynamics Observatory in 2010, EUV imaging observations have simply not provided a strong enough constraint on the plausible physical scenarios that describe EUV waves. This, combined with the relative uncertainty in coronal magnetic field strength due to limitations inherent in observation and extrapolation methods, has

made it difficult to strictly prove fast-mode wave theories or to rule out possible non-wave mechanisms to explain the large-scale EUV transient. Much progress has been made through time-dependent MHD models of EUV waves (e.g. Wu et al. (2001); Chen et al. (2002); Delannée et al. (2008); Cohen et al. (2009); Schmidt & Ofman (2010)), but in these works the observable implications must be treated indirectly because they are fundamentally missing realistic density and temperature stratifications (for one reason or another).

In order to contribute meaningfully to this debate, a study exploring this phenomenon must necessarily have the following properties:

- The contribution of both wave and non-wave scenarios can be examined within the same framework in an unbiased manner. This requires that the full non-linear dynamics of the eruption are captured, (i.e. not assuming linear waves a-priori like Patsourakos et al. (2009)), and the use of idealized eruption models that pre-impose specific properties is avoided (e.g. Delannée et al. (2008)).
- Furthermore, it is not only required that the conditions modeled represent a parameter space that is actually relevant to observations, but that they can be verified and validated through direct comparison to observables. This is absolutely critical for both narrowing the parameter space explored by the study but also lending credence to the results.

It is these key points that we attempt to account for head on over the three year course of the dissertation research presented here.

Chapter 3

Magnetohydrodynamics: Overview and Applications to Space Plasmas

3.1 Overview of MHD

In an ideal world of modeling, one of unlimited capability and resources, we would imagine studying complex space plasma systems by following in explicit detail the individual evolution of their constituent particles. Under these perfect conditions, the ensemble behavior that generates solar flares and CMEs could be perfectly captured without worry that the underlying physics are flawed. Of course, in reality this is absurdly unfeasible, a single CME may contain upwards of 10^{40} particles. In truth, producing realistic theoretical models of phenomena is always a sort of balancing act, one where the researcher must walk the the fine line that separates analytic or computational feasibility with physical accuracy.

Perfect examples of this perspective and process are found in the field of fluid mechanics and its extensions such as MHD. Here, the necessary complexity reduction is achieved in the transition from following the evolution of specific particles to that of their ensemble averages. Instead of tracking particles, we follow the their macroscopic

variables: i.e. density, bulk velocity, pressure. This process that best summed up as going from a *microscopic* perspective to a *macroscopic* one. The fundamental difference between classical fluid mechanics and MHD is that the presence of the magnetic field introduces an anisotropy. Particle orbits of the electrons are tightly bound to the magnetic field, and thus cannot easily move perpendicularly across field lines. At the same it is these very particle orbits that influence the evolution of the magnetic field. This anisotropy and self-modulating feedback increases both the ensuing complexity of the equations and their wave characteristics, but the general principles remain the same. To put it bluntly, MHD provides the simplest *macroscopic* description of magnetized plasma that money can buy.

It is for this reason that fluid descriptions like MHD have been so universally used and beneficial towards advancing our understanding. When valid, the reduction of the problem from that of particles to their representative macroscopic variables (density, pressure, velocity, magnetic field) enables the focus to shift to capturing the evolution of the whole, rather than partial views of the system of interest. Of course, not all aspects of space plasmas are so agreeable to be conveniently captured by the MHD description. For these, we must return to the more basic kinetic physics that MHD evolved from in order to (hopefully) derive sufficient macroscopic approximations to describe them.

3.1.1 The MHD equations

The ideal magnetohydrodynamic (MHD) equations represent a highly useful and efficient way to represent a magnetised plasma, and are appropriate for a large number of systems. For this reason they are used almost ubiquitously in studies the solar corona on large scales in some form or another and are the backbone of the modeling

effort proposed here. The divergence form of the ideal MHD equations for a proton-electron fluid in three dimensions are listed here (Powell 1999)¹:

$$\mathbf{Mass} : \quad \frac{\partial \rho}{\partial t} + \nabla \cdot (\rho \vec{u}) = 0 \quad (3.1)$$

$$\mathbf{Momentum} : \quad \frac{\partial \rho \vec{u}}{\partial t} + \nabla \cdot \left[\rho \vec{u} \vec{u} + \left(p + \frac{\vec{B} \cdot \vec{B}}{8\pi} \right) \mathbf{I} - \frac{\vec{B} \vec{B}}{4\pi} \right] = 0 \quad (3.2)$$

$$\mathbf{Energy} : \quad \frac{\partial E}{\partial t} + \nabla \cdot \left[\left(E + p + \frac{\vec{B} \cdot \vec{B}}{8\pi} \right) \vec{u} - \frac{(\vec{u} \cdot \vec{B}) \vec{B}}{4\pi} \right] = 0 \quad (3.3)$$

$$\text{where, } E = \frac{p}{\gamma - 1} + \rho \frac{\vec{u} \cdot \vec{u}}{2} + \frac{\vec{B} \cdot \vec{B}}{8\pi}$$

$$\mathbf{Induction} : \quad \frac{\partial \vec{B}}{\partial t} + \nabla \cdot (\vec{u} \vec{B} - \vec{B} \vec{u}) = 0 \quad (3.4)$$

At their essence these four equations represent three basic physical conservation laws, namely conservation of mass, momentum, and energy, which can be closed with the induction equation (governing magnetic field evolution). Noting the dependence of magnetic field both in the momentum and energy equations it becomes clear that the three dimensional nature and time evolution of the magnetic field is absolutely critical in the dynamic representation of the system.

However, it is equally important to emphasize the implicit assumptions and limitations of MHD as well. More specifically, these equations are derived assuming the system satisfies four general limits. Because MHD describes a macroscopic fluid, the first two require that system is examined on sufficiently long length and time scales, (i.e. length scales, L , larger than Debye shielding length $\lambda_D \ll L$, and the system evolves slower than the plasma frequency $1/\omega_p \ll \tau$, which is a characteristic

¹note that notation of two consecutive vectors refers to the tensor product of the two vectors (components of $\mathbf{T} = \vec{B} \vec{B}$ are denoted as $B_i B_j$). The divergence of this tensor collapses the first index and produces a vector ($\nabla \cdot \vec{B} \vec{B}$ goes like $\partial_i B_i B_j$), which is why these products are present in the momentum and energy equations (Equations 3.2 and 3.3).

oscillation timescale). Because plasma particles also possess electric charge, MHD also requires that dynamics are not dominated by individual electrostatic potentials (i.e. the Debye sphere has a large number of particles and electric fields are easily 'shorted out'). This is commonly expressed in terms of requiring a large plasma parameter, $\Lambda \gg 1$, or as the 'weak coupling limit'. It is worth noting that for this reason most space plasmas are electrically neutral to an extremely high degree despite their large ionization fraction. The final assumption is that of collisionality, which requires that the zero-order phase space distributions of particles from which we obtain the macroscopic moments of density, temperature, etc. are Maxwellian (at least to a good degree of approximation).

Even so this not the whole story when describing an actual magnetized plasma that satisfies the above constraints (i.e. the corona). By rigorously expanding Fokker-Planck equation (which describes the phase-space evolution of a kinetic ensemble) and including the appropriate limits of a collisional electron-proton fluid, the ideal MHD equations result naturally as a solution when considering only the lowest order moments of the distribution functions of the protons and electrons. Referred to as the Braginski equations (Braginskii 1965), a more accurate complete solution involves 6 fluid equations (three each for electrons and protons), completion relations to close the system, and expressions for the first order considerations that effect the zero-order Maxwellian distributions (often referred to as 'transport effects'). These first order terms represent phenomena that become important under limiting conditions, such as anisotropic heat conduction (large T and ∇T), viscosity (large Reynolds number, $R_e = LV_0/\nu \gg 1$), magnetic resistivity (small Lundquist number, $S = 4\pi Lv_a/\eta \ll 1$), and additional two-fluid proton-electron interactions. All of these terms may have importance depending on the plasma physics application, and

can be seen in various applications to the solar corona and heliosphere. Electron heat conduction in the corona for example (Section 2.4) is one such transport effect.

One process not described at all by ideal MHD is magnetic reconnection. In ideal MHD the “frozen-in-flux” condition dictates that field lines cannot cross or slip through each other. This also states that for a given bundle of field lines, no-matter the complex distortions and compression introduced by fluid motions that the magnetic flux along any cross section is preserved. This ideal case has its limits: as adjacent anti-parallel flux systems are squeezed together, reconnection regions tend to form in small, thin current sheets. It is here where non-ideal kinetic processes are critically important, particles become able to slip across flux systems, accelerate and ultimately dissipate energy.

For this reason is up to the researcher to include the most appropriate physics and approximations to solve the task at hand in a tractable manner while still providing valid and valuable insight into the system of study. For example, it is possible to consider in detail specific particles when studying shock acceleration of energetic particles in an idealized manner, but it becomes highly non-feasible to do so for the entire 3D environment from the Sun to Earth without significant approximations. Even the ideal MHD equations become quite computationally expensive when applied to two or three dimensions. To include additional considerations, it is worth noting that with the representation of ideal MHD given above, the time dependence of a state variable, q_i , is of the form $\frac{\partial q_i}{\partial t} + \nabla \cdot \vec{F}_i = Q_i$. This states that the evolution can be written as the contribution of two terms, namely, the divergence of an MHD flux vector, \vec{F}_i , and an additional source term, Q_i . A numerical scheme of this manner then lends itself naturally then to including additional terms that may be important (e.g. adding $Q_G = \rho \vec{g}$ to the RHS of the momentum equation to account for gravity).

3.2 Computational Methods for MHD

Due to both their form and complexity, a natural setting for solving the full MHD equations is the computer. Because of the ability of a modern computer processor to perform billions of floating point operations per second, computers offer tremendous flexibility in terms of the problems to be solved. In using a computer, the researcher is no longer limited to solving the evolutionary equations by hand, this enables problems that feature arbitrary inhomogeneity that would be otherwise intractable to be investigated.

Of course this benefit does not come without a price! The ability for a computer to solve more simple equations in a second than the average person in a lifetime means that it is not always so straightforward to interpret the results. This removal of the researcher as the central actor in the computation can limit her/his ability to gauge both the accuracy and physical underpinnings of the dynamics. This is particularly true for large-scale 3D time-dependent simulations where the numbers of discrete variables represented at any one time can easily exceed the tens of millions.

The field of modeling hyperbolic systems of partial differential equations (MHD is one such system) using computers is quite broad and far beyond the scope of this document. Major points relevant to the computational methods used in this work are presented here.

3.2.1 Finite Volume Methods

One main aspect of the computational approach is the decomposition of the domain into individual computational elements where the continuous variables are broken down to floating point values. In the “finite volume” approach this decomposition has a tangible geometric representation.

Here we note that in the divergence form of the MHD equations (Equations 3.1 to 3.4) are explicitly written in the form of a conservation law. A conservation law for a state variable, q_i , is represented as:

$$\frac{\partial q_i}{\partial t} = -\nabla \cdot (\vec{F}_i), \quad (3.5)$$

where the vector \vec{F}_i represents the flux or “flow” of q_i . This form is immediately relevant to computer modeling if one thinks about the decomposition of a 3D space into polygonal elements (e.g. rectilinear cells). The volume integral of this divergence term can then be represented as a surface integral along the cell boundary using Gauss’s Law, where in this case the continuous surface integral becomes a finite sum over the flux at each face dotted with the face area, $\vec{A} = \hat{n} * Area$:

$$\int_V \nabla \cdot \vec{F}_i = \oint_S \vec{F}_i \cdot d\vec{A} = \sum_{j=1}^{faces} \vec{F}_i^j \cdot \vec{A}^j \quad (3.6)$$

The use of this type of volume decomposition and rewriting of the hyperbolic equations as a series of fluxes is typically referred to as a class of methods known as the ‘finite-volume’ scheme or method. This is illustrated graphically in Figure 3.1.

State Limiters and Flux Functions

Although the finite volume method provides a tangible geometric representation of the computational problem, the process of calculating the flux at the face surfaces presents a rich mathematical and physical problem. As with any discretization problem, the choice of interpolation method will govern the local order accuracy and convergence rate. Furthermore, the hyperbolic nature of MHD implies that waves, not diffusion or other processes are the drivers of change from state to state. This means in

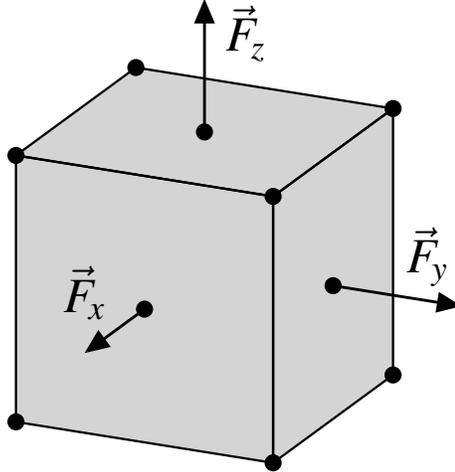


Figure 3.1: Illustration of the face fluxes for a cell in a finite volume scheme. Each of the fluxes from the four MHD equations are calculated at each of the six face boundaries (three shown).

a discretized representation, state changes are inherently oscillatory and can form sharp discontinuities (shocks) in regions of strong flow. For example, simply choosing to interpolate the state variables using the midpoint rule ($q^{i+\frac{1}{2}} = (q^i + q^{i+1})/2\Delta x$ in 1D) and using them to calculate the fluxes would give a hopelessly unstable *and* inaccurate evolution of the system.

The two main choices when solving for the interpolated MHD fluxes of at the faces of volume elements are: (i) choosing the way in which state variables are normalized to prevent spurious oscillations, referred to as the *limiter*, and (ii) choosing the process in which the flux is reconstructed at the faces, referred to as the *flux function*. The combination of these functions is typically problem dependent, as some flux functions are custom designed for the high order capturing of discontinuous shocks (e.g. the 8 wave Riemann-solver in Powell (1999)), while others may be more dissipative, seeking to hinder spurious oscillations and instability. A full description of the flux functions and limiters available in the MHD model used in this work can be found in Tóth et al. (2006).

Adaptive Mesh Refinement

One particularly useful tool in modern computational fluid dynamics is the use of what is known as Adaptive Mesh Refinement (AMR). As is often the case when studying inhomogeneous, non-linear flows, the grid resolution required to resolve a particular part of the evolution will depend highly on its local characteristics. Shock forming regions are naturally small and thin layers with sharp discontinuities and require high resolution, while smooth laminar flow will exhibit weaker gradients and may require relatively less resolution.

This means that if one must choose a grid is chosen beforehand, say a rectilinear decomposition of uniform cell widths along all three dimensions, then the minimum resolution required must be both known a-priori and be implemented over the entire domain. This represents a significant waste of computational resources if these scales are not expected to be necessary at all times and locations throughout the domain.

Adaptive mesh refinement addresses this issue directly by providing an alternative and solution dependent domain decomposition method. In the AMR construct, the domain is first decomposed into a number of low resolution “root” blocks that contain an even integer of cells along each axis. Taking each of these blocks as a self contained entity, a given block can be refined by a factor of two along each dimension creating a set of “child” blocks that make up the original (2, 4, and 8 children in 1D, 2D, and 3D respectively). The solution can now be calculated on the new blocks at double the resolution. As illustrated in Figure 3.2, refinement of the grid down to a desired resolution is achieved through the successive refinement of child blocks into new sets of blocks, essentially creating a hierarchical nesting of the geometry.

The “adaptive” part of AMR comes from the ability to refine or coarsen (unrefine) the blocks during the simulation depending on the flow properties. Given the

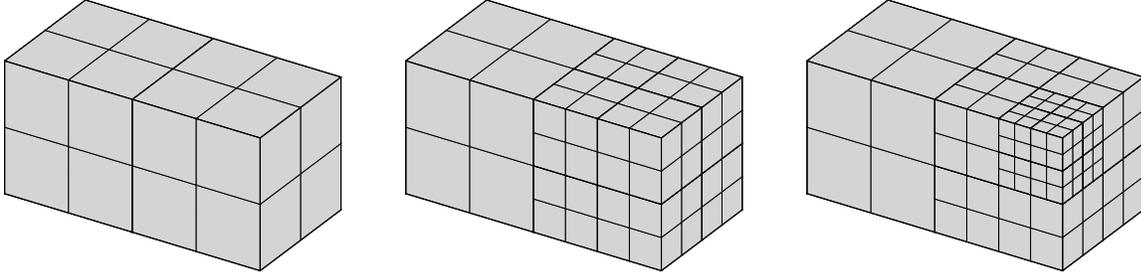


Figure 3.2: Illustration of the Adaptive Mesh Refinement process for a pair of $2 \times 2 \times 2$ blocks. Starting from the initial blocks (left) the right block is refined by one level into eight child blocks (middle). Now each of the child blocks may be separately further refined by an additional level as required by the simulation, which is shown for the top corner block (right). The refinement case on the right consists of $(1 + 7 + 8) \cdot 2^3 = 128$ cells while a uniform grid at level 3 resolution would require $8 \cdot 8 \cdot 2 \cdot 2^3 = 1024$ cells.

value of some physical heuristic (e.g. a shock steepening or strong electric currents) the grid resolution may be adjusted on the fly to properly capture the dynamics. This greatly enhances both the efficiency of the simulation by reducing the number of cells needed at any one time (a factor of ten in the example shown in Figure 3.1) and the accuracy by allowing the resolution to follow the physical evolution of the system as needed. Please see Powell (1999) for a description of the implementation of AMR in the 3D MHD model used here.

Generalized Grids

Another method relevant to this project is applying the finite-volume method to geometries beyond simple Cartesian boxes. The boundary surfaces of the Sun and Earth for example are spheres, and a sphere does not conform well to the principle axes of a Cartesian box overlaid over its surface.

One solution to this problem is to transform the uniform Cartesian representation to a more general finite-volume decomposition, i.e. a ‘generalized grid’. This is illustrated in Figure 3.3. Here a $4 \times 4 \times 4$ Cartesian block of cells (left) represents a uniform array in $(\ln(r), \phi, \theta)$ coordinates, referred to as the generalized coordinates.

This block is then transformed to the physical (x, y, z) spatial coordinates (right). Because the transformation acts on the nodes (vertices) of the cells and the $(\hat{r}, \hat{\phi}, \hat{\theta})$ directions are locally orthogonal, the polygonal nature of each cell is conserved and fluxes are still easily represented across face boundaries. The data arrays are still represented as Cartesian arrays, but now both the face areas and face normals vary across the cells, which allows for many complicated configurations to be represented in their natural geometry (a sphere in the case of the sun). This is particularly important in the case of the Solar Transition Region for example, where the radial gradient of temperature becomes extremely steep, requiring extremely fine resolution. Instead of having to refine all three (x, y, z) axes in order to cover the curvature of the lower boundary, a single non-uniform variation in r can be used (this is the implementation described in Section 4.2.4).

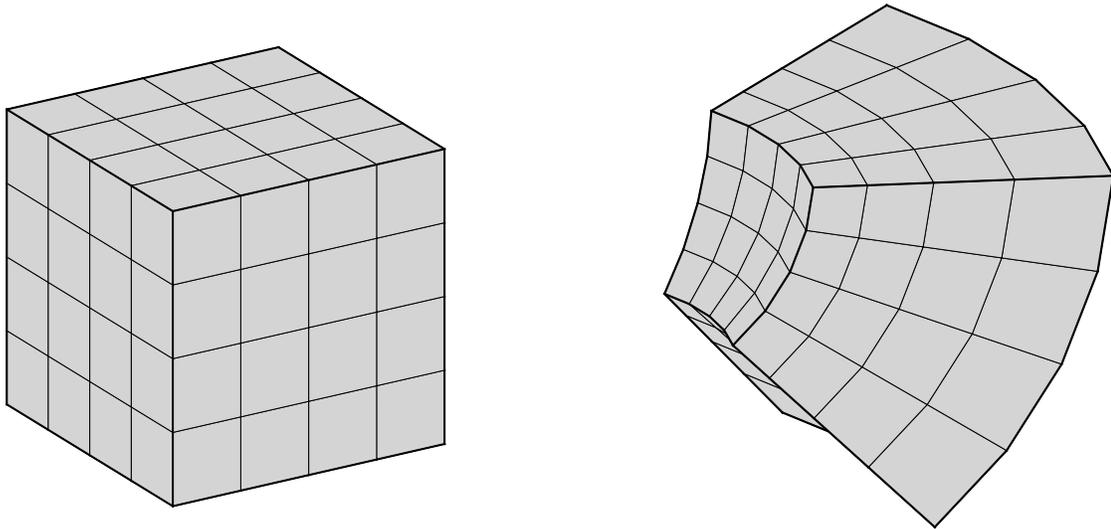


Figure 3.3: Illustration of a generalized grid transformation for a 3D block of cells for the case of logarithmic spherical coordinates.

Chapter 4

The Low Corona Model

Abstract

In this chapter we describe our implementation of a thermodynamic energy equation into the global corona model of the Space Weather Modeling Framework (SWMF), and its development into the new Lower Corona (LC) model. This work includes the integration of the additional energy transport terms of coronal heating, electron heat conduction, and optically thin radiative cooling into the governing magnetohydrodynamic (MHD) energy equation. We examine two different boundary conditions using this model; one set in the upper transition region (the Radiative Energy Balance model), as well as a uniform chromospheric condition where the transition region can be modeled in its entirety. Via observation synthesis from model results and the subsequent comparison to full sun extreme ultraviolet (EUV) and soft X-Ray observations of Carrington Rotation (CR) 1913 centered on 1996 Aug 27, we demonstrate the need for these additional considerations when using global MHD models to describe the unique conditions in the low corona. Through multiple simulations we examine ability of the LC model to assess and discriminate between coronal heating models, and find that a relative simple empirical heating model is

adequate in reproducing structures observed in the low corona. We show that the interplay between coronal heating and electron heat conduction provides significant feedback onto the 3D magnetic topology in the low corona as compared to a potential field extrapolation, and that this feedback is largely dependent on the amount of mechanical energy introduced into the corona.

4.1 Introduction and Background

With its origin in the long-studied fundamental question of how the solar corona can be heated to and maintain temperatures in the million Kelvin (MK) regime, a primary focus of this study is to address the issue of energy input into the corona in the context of a fully 3D global model. Because non-MHD processes of energy transport and local conditions in the low corona are responsible for coronal heating mechanisms, it is often quite difficult and computationally expensive to include the small-scale micro physics of reconnection and turbulence responsible for coronal heating in 3D models, especially since the exact processes involved are not universally agreed upon. As a result, heating models are often parameterized as a heating term that depends on various local magnetic and thermodynamic properties that is included in the energy equation (e.g. Aschwanden & Schrijver (2002); Schrijver et al. (2004); Abbett (2007); Mok et al. (2008)). However, due to the large number of heating models and their ad-hoc formulations, it is crucial to use real observations to compare and constrain these models and deduce the best combination of models, both for active regions and the quiet Sun, that yields the most realistic global simulations. When using such models to study transient events in the Solar Corona, particularly Coronal Mass Ejections (CMEs) and coronal waves seen in the extreme ultraviolet regime (EUV waves, Moses et al. (1997)), it is a motivating principle that only by constraining physical theories

and scenarios through as many observable manifestations available can we provide the best possible avenue to further our knowledge and precision in understanding these dynamic events (e.g. Lugaz et al. (2008, 2009); Cohen et al. (2009)). The ultimate goal being to strip away layers of empirical approximation with more fundamental physical terms and mechanisms. However, it is equally important to validate and asses the ability of these improvements to adequately represent the global conditions in the solar corona.

To address this issue through a deterministic, data-driven approach, we modify the global corona model of the Space Weather Modeling Framework (SWMF) (Tóth et al. 2005) to include the transition region between the chromosphere and the corona, where non-MHD thermodynamic terms of energy transport, such as electron heat conduction, radiative losses, and coronal heating all become important. Using techniques similar to the pioneering work of Lionello et al. (2001, 2009), in this refined version of the model the inner boundary is placed at the chromosphere or upper transition region rather than in the low corona and the now relevant non-MHD terms are added to the governing MHD energy equation.

In Section 4.2 we discuss the new Lower Corona (LC) model and physical considerations added as part of this work. In Section 4.3 we overview our runs and results and discuss the application of this model to the study of the corona (in particular the comparison to EUV imaging observations). In Section 4.4 we provide a detailed analysis of a particular run, and benchmark it via comparison to a previous corona model. We conclude in Section 4.5.

4.2 The Simulation Tool

4.2.1 SWMF

The main model and starting point for this work is the SWMF Solar Corona (SC) model (Cohen et al. 2007). As far as numerical methods, the code is fully parallelized and designed to be highly customizable in terms the methods, solvers, and equations used. A complete description of the MHD equations and their implementation in the SWMF can be found in Powell (1999) as well as the addition of source terms in (Groth et al. 2000). For the current version of the Solar Corona Model, a steady state solar wind solution is obtained using a variable γ model (Roussev et al. 2003b; Cohen et al. 2007, 2008). The latter references use the Wang-Sheeley-Arge (WSA) model (Arge et al. 2004) as an initial condition to derive the variation in the polytropic index. This then achieves a steady state MHD solution after nominal integration (henceforth referred to as the “Standard SC model”).

Physically, the most important advantage of this tool and others like it lies in its ability to simulate the complete 3D environment of any event and Carrington Rotation (standardized solar rotation number, abbreviated CR) for which data for the photospheric magnetic field is available throughout the entire solar surface. The initial magnetic configuration is extrapolated using the Potential Field Source Surface Method (PFSSM) (Altschuler et al. 1977), which uses magnetic coefficients derived from observations of the synoptic photospheric magnetic field (typically high order maps using data from the MDI instrument aboard the SOHO observatory, or low order maps the Wilcox Solar Observatory). Using this method, the subsequent evolution of the magnetic field towards a steady state during the simulation is no longer strictly potential.

While the standard version of the SC model has been very successful at reproducing the bi-modal solar wind structure and observations at 1AU (Cohen et al. 2008), which was the fundamental goal of that empirical model, the lower boundary at the solar surface is quite smooth and nearly uniform. In order to reproduce and study the fine structures of the the low corona we significantly modify the SC model to address the unique physics that take place at this boundary (henceforth referred to as the the Lower Corona (LC) model).

4.2.2 Including Additional Thermodynamic Terms

This modification of the energy equation takes the form of:

$$\frac{\partial E}{\partial t} + \nabla \cdot (\vec{F}_{MHD} + \vec{F}_c) = Q_{MHD} + Q_r + Q_h \quad (4.1)$$

where, the subscript *MHD* refers to the standard MHD terms in the SWMF and the additional terms \vec{F}_c , Q_r , Q_h are described below. Because these terms account for realistic energy transport, the polytropic index is no longer variable, and is set to a uniform value of $\gamma = 5/3$.

Heat Conduction

The standard form of anisotropic electron heat conduction in the collisional limit is included as an additional energy flux term, $\vec{F}_c = -\kappa_0 T^{5/2} \hat{B}(\hat{B} \cdot \nabla T)$, in the energy equation (equivalent physically to adding a source term of $Q_c = \nabla \cdot \vec{F}_c$). The parallel component of Spitzer conductivity (Spitzer 1965), this term is especially important in the transition region and low corona and plays a critical role in determining the equilibrium density and temperatures at the base of the corona. We use a value of $\kappa_0 = 1.23 \times 10^{-6}$ in cgs units.

As mentioned below, one of the two boundary conditions implemented sets the base of the model at chromospheric temperatures, meaning the transition region must be resolved in the model. Because it would be computationally infeasible to resolve the transition region down to scales of a few kilometers, we also include a method for broadening the equilibrium scale length of the transition region, which modifies the conductivity coefficient, κ_0 (described in detail by Abbett (2007); Lionello et al. (2009)). A brief dimensional argument for this method is given in appendix A.

Radiative Losses

The next term, $Q_r = -n_e n_p \Lambda(T)$, accounts for the radiative losses of the hot coronal plasma in the optically thin limit. The loss function $\Lambda(T)$ is calculated using the CHIANTI version 5 radiative loss routines (Landi et al. 2006) and linearly interpolated as a tabulated function in the model. The assumption of a fully ionized hydrogen gas is already implicit in this model, which gives $n_e n_p \sim n_e^2$. It is important to note that the choice of abundances used in calculating the radiative losses function can change the total losses significantly in the coronal temperature regime. For this reason we choose to use the coronal abundances file: `sun_coronal_ext.abund` (Landi et al. 2002) when calculating the radiative cooling curve with CHIANTI, and do not vary this function in this work.

Heating Model 1 - $|B|$ weighted

The first empirical coronal heating term, Q_h , that we examine is equivalent in form to that used by Abbett (2007) and is originally based on the universal relationship between the surface unsigned magnetic flux of a stellar photosphere to the integrated x-ray luminosity of its corona, which was derived by Pevtsov et al. (2003). This model

is expressed as:

$$Q_h = \frac{c\phi^\alpha\psi}{\zeta \int \psi dV}. \quad (4.2)$$

Where $c = 0.8940$, $\alpha = 1.1488$ are fixed parameters (values from Bercik et al. (2005)), ϕ represents the total unsigned magnetic flux at the solar surface, ψ is the local heating weighting function, and ζ is a normalization constant. This formulation calculates the total amount of energy input into the corona and distributes it via ψ , which is chosen to be a function of $|B|$. The primary benefit of this model is its simplicity, the amount of heating at any location is given by the value of ψ , and the total amount of heat input to the corona (nearly constant) is normalized by the global integral in the denominator, $\int \psi dV$, which is carried out over the entire domain. In this implementation, ϕ is calculated by integrating the unsigned flux at the model boundary at $r = R_\odot$, $\phi = \oint_{r=R_\odot} |B_r| dS$, which is essentially the photospheric magnetogram used to initiate the model.

Because both the relationship between X-Ray Luminosity and total power input into the corona is not well constrained, and varying magnetogram resolution does not constrain the true unsigned flux, ζ represents a relatively free parameter with which to adjust the total power on a case by case basis. In our model runs we choose $\zeta = 1/50$ and linear weighting with the magnetic field magnitude, $\psi(|B|) = |B|$. This gives the heating term the operational equivalent of $Q_h = H|B|$, where H is typically around $\sim 4 \times 10^{-5}$ in cgs units, and total integrated power of $Q_{tot} = 3.11 \times 10^{28}$ ergs s^{-1} if applied uniformly.

One drawback of this term (and of other $|B|$ weighted heating terms in global models) is that the heating scale height, defined as the point along a given loop where $Q_h(s) = Q_h(s = 0)/e$, is not a free parameter and varies with the strength and spatial distribution of \vec{B} . Also, note that the value of H depends on the specific

global magnetic field configuration and the radius to which the volume integral is calculated. In this work, we limit the range of influence of this function to the low corona by multiplying ψ by an exponential envelope function with a scale height of 40Mm.

Heating Model 2 - exponential heating

The second heating model is a simple exponential scale height model. Using a standard exponential form we define heating model 2 as:

$$Q_h = H_0 \exp[-(r - R_\odot)/\lambda]. \quad (4.3)$$

Where H_0 is the local heating rate at $r = R_\odot$ and λ is the heating scale height. A short heating scale height is consistent with SOHO and TRACE EUV observations of coronal loops (Aschwanden et al. 2000; Aschwanden & Acton 2001), and motivated by the “nanoflare” class of coronal heating models, in which most of the heat is deposited in the upper chromosphere and transition region (Parker 1988). It is important to note that it is the high thermal conductivity of the coronal plasma that subsequently distributes this energy along the field/flow lines. For heating quiet sun regions, we use the values $H_0 = 7.28 \times 10^{-5}$ ergs cm⁻³ s⁻¹, and $\lambda = 40$ Mm, which give a total power of $Q_{tot} = 1.99 \times 10^{28}$ ergs s⁻¹ if applied uniformly (surface flux = 3.27×10^5 ergs cm⁻² s⁻¹). The lack of explicit dependence on $|B|$ with an exponential scale height model allows us examine directly the effect that purely the magnetic geometry of the 3D corona has on the resultant thermodynamic equilibrium.

Coronal hole heating

To maintain realistic temperatures in the solar wind and coronal holes at large distances, we use the same form of Equation 4.3 with values of $H_0 = 5.0 \times 10^{-7}$ ergs cm⁻³ s⁻¹, and $\lambda = 0.7R_\odot$ giving additional total power $Q = 5.01 \times 10^{27}$ ergs s⁻¹. This function is applied uniformly in each model run. While not entirely realistic for the acceleration profiles observed in coronal hole regions and the solar wind, we find that including this term is adequate for reproducing coronal hole emission in the absence of short scale height heating.

Open field cutoff

One interesting focus of this study is to isolate the complementary effects that non-uniform heating at the surface and the 3D magnetic topology have in determining the equilibrium structure of the corona. For this reason, as one of the options in the model we include the ability to apply the low scale height heating model (either 1 or 2) to only regions associated with closed field in the corona. To do so, we use the PFSSM extrapolation computed to initiate the model to determine at every computational element whether the field threading the location is open (connects to the source surface and becomes radial) or closed (turns back down to the solar surface). If the region is associated with open field, then only the long scale height “coronal hole” heating model is applied (Section 4.2.2), while if the region is closed, both are applied.

We would also like to note that any of the empirical heating terms discussed above may also be attributed to wave absorption and dissipation, probably due to the ion interaction with Alfvén wave turbulence. In this case, the heating may be specified in terms of the wave (spectral) energy and their damping coefficient, and

the wave turbulence may contribute not only to the energy source but also to the momentum fluxes (see e.g. Sokolov et al. (2009) and papers cited therein). However, this particular study is focused primarily on the plasma conditions low corona, and we operate under the assumption that Alfvén wave pressure will be much lower than the thermal pressure there.

4.2.3 Boundary Conditions

Boundary conditions at the $r = R_\odot$ surface are applied to fix constant values temperature and density at the face boundary according to either of the models described below. Each of these use a zero flow condition and fix the tangential component of the magnetic field (similar to those used in Roussev et al. (2004); Jacobs et al. (2009)). For the supersonic flow at the outer boundary at $r = 24R_\odot$ we use a floating (zero-gradient) condition.

Chromospheric Boundary

The primary boundary condition used in this model is a simple uniform “chromospheric” condition. As described in Lionello et al. (2001, 2009), by setting chromospheric values of electron temperature, $T_e = 2 \times 10^4$ K, and density, $n_e = 1 \times 10^{12}$ cm⁻³, and including the transition region broadening method described in Section 4.2.2, it becomes possible to resolve the entire transition region everywhere in a global model. This is a critical advantage because the resultant topological equilibrium in the coronal part of the solution (density enhancements, varying width of the transition region, etc.) will depend entirely on the included physics and magnetic geometry, and not on its proximity to the boundary of the model. This fact is particularly important for the study of any sort of dynamics in the global corona, as

the sharp transition from fast Alfvén speed in the quiet corona ($V_a \sim 2-3 \times 10^2 \text{km/s}$) to extremely slow speeds in the chromosphere ($V_a \sim < 50 \text{km/s}$), provides a realistic dispersion buffer for fast magnetosonic waves.

REB Model:

In order to include a realistic lower boundary condition for the corona, while at the same time maintaining decent computational efficiency for the global domain, we use the method of the Radiative Energy Balance Model (REB) outlined by Withbroe (1988) (further formalism, including coronal heating in Lionello et al. (2001)). In short, this model fixes the base electron temperature to a high transition region value, $T_e^{tr} = 5 \times 10^5 \text{K}$, and in turn assumes an equilibrium balance throughout the rest of the Transition Region below to the top of the Chromosphere, from which an electron density, n_e^{tr} , may be obtained. By rearranging the terms in the MHD energy equation and integrating over T at constant pressure, one can express n_e^{tr} , solely in terms of the incoming heat conduction flux, coronal heating, and radiative losses:

$$n_e^{tr} = \sqrt{\frac{\frac{1}{2}\kappa_0(T_e^{tr})^3(\hat{B} \cdot \nabla T_e)^2 + \frac{2}{7}Q_h(T_e^{tr})^{\frac{3}{2}}}{\int_{T_e^{ch}}^{T_e^{tr}} T^{\frac{1}{2}}\Lambda(T)dT}} \quad (4.4)$$

where, the integral of the radiative loss function, $\Lambda(T)$, is carried out between $T_e^{ch} = 10^4 \text{K}$ and $T_e^{tr} = 5 \times 10^5 \text{K}$. This allows for the base density n_e^{tr} to be a function of the physical conditions included in the model (coronal heating, anisotropic heat conduction, and radiative cooling) and thus varies spatially along the boundary. Most importantly, the numerator of Equation 4.4 shows how the interplay between magnetic field strength, $|\vec{B}|$ (via Q_h in the right term), and normal orientation at the surface, \hat{B}_r (via $(\hat{B} \cdot \nabla T_e)^2$ on the left), sets the base density on the solar surface.

The ability to capture these features with such a simple, easily computed boundary is a primary motivation in using this particular model.

4.2.4 Geometric Considerations

Another aspect of this work has been to address the unique geometric concerns that arise when including the transition region and below. A typical solar corona (SC) simulation is carried out with an adaptive Cartesian grid over a Sun-centered $48 \times 48 \times 48 R_{\odot}$ cube with $4 \times 4 \times 4$ cell blocks. The average cell size is smallest at the surface ($\sim 10^{-2} R_{\odot} \sim 7,000$ km) and is incrementally increased with distance to a largest size of $0.65 R_{\odot}$ near the outer boundary, giving a few million cells. While this is a relatively large surface cell size, it is adequate considering the precision of the magnetic field boundary (an observational limitation). However, if one is required to resolve the transition region, with dynamic radial spatial scales on the order of a few km, it quickly becomes infeasible to use a Cartesian grid (with every 1/2 refinement in length the number of surface cells increases by 4). This can be partially alleviated using methods to widen the extent of the model transition region to typical scales of order 300 km without affecting the coronal solution (Section 4.2.2), but the problem is still quite substantial. This then represents a balance between height accuracy and computational efficiency (with a Cartesian grid, the number of surface cells increases by a factor of 4 with every successive 1/2 refinement).

To address this scale and resolution issue we adapted the generalized grid capability of the SWMF, which has ability to calculate MHD fluxes in arbitrary geometries, to construct a spherical (r, θ, ϕ) grid function with highly non-uniform radial scales near the transition region ($dr = 230$ km) that smoothly transitions to near equal face area at large r ($dr = 30,000$ km at $r = 5R_{\odot}$). Because the grid

function is continuous, the model maintains the block-adaptive mesh and adaptive mesh refinement (AMR) capability for flexible local spatial resolution both initially and as the simulation progresses. For this study, focusing on the global structure of the corona, we use a uniform spacing in the angular directions with $d\theta = d\phi = 1.4^\circ$ at the surface, which is coarsened by a factor of two via AMR beyond $1.7R_\odot$ for regions within $\pm 65^\circ$ and $1.2R_\odot$ outside (to avoid needlessly small cell sizes at the poles). The outer boundary is fixed at $r = 24R_\odot$. Degenerate cells touching the polar axes are treated with azimuthal averaging to avoid discontinuity across the poles. A grid comparison near the surface between this work and an AMR cartesian mesh with a similar number of total cells is shown in Figure 4.1.

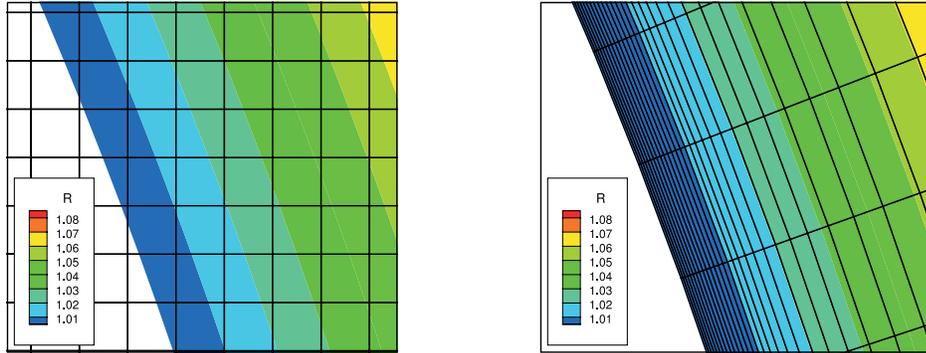


Figure 4.1: Comparison of grid geometry and cell sizes near the solar surface for the SWMF SC model (coloring indicates radial extent). Left: a Cartesian grid with minimum $ds = 6,800$ km. Right: The customized spherical grid with minimum $dr = 230$ km (part of this work). All three directions do not have to be further refined at the surface to enhance the radial resolution when using spherical geometry, leading to significant savings in computational overhead. In this example, both simulation domains have comparable numbers of total cells.

4.2.5 LOS image synthesis

To study the EUV corona and associated dynamics in the context of real events, we include a proper treatment of integrated coronal emission in the EUV range, particularly for the purpose of comparing simulated observations to existing EUV

observations by a current solar observatory. This process, following the work of Mok et al. (2005, 2008); Lionello et al. (2009), involves two main steps: (i) characterization of detector response based on physical parameters that are calculated in the model and (ii) line-of-sight (LOS) integration through the 3D data set to create synthesized image.

The first step is to understand and calculate the instrumental response for coronal material at a given temperature and density. For simplicity and ease to compare to studied observations we chose to model the three coronal band-passes at 171, 195, and 284Å of the EIT instrument on the SOHO spacecraft (Delaboudinière et al. 1995) and the AlMg filter of the Soft X-ray Telescope (SXT) (Tsuneta et al. 1991). Because of the extremely high temperature and low densities, the emission line EUV and Soft X-Ray radiation of the solar corona above 0.5 MK can be treated as optically thin to a good approximation. As such, the intensity measured by each pixel of an imaging detector can be treated as a LOS integral through the coronal plasma, namely:

$$R = \int n_e^2 f_i(T, n_e) dl \text{ DN s}^{-1} \quad (4.5)$$

where R is the pixel response measured in Data Numbers (DN) per second. Here l follows along the line-of-sight, the square of the electron density, n_e^2 , accounts for the amount of emitting material and $f_i(T, n_e)$ is the instrumental response of filter i per unit emission measure as a function of both temperature and density. This is equivalent to integrating the resolved Differential Emission Measure (DEM) distribution along l . To calculate the response functions, $f_i(T, n_e)$, we use the CHIANTI version 5 emission line analysis routines (Landi et al. 2006) to generate synthetic spectra, and the EIT and SXT analysis routines for detector response (a part of the SolarSoft (SSW) framework written in IDL (Freeland & Handy 1998)).

More details on detector characterization as well as the second step, the actual LOS integration through the dataset, are provided in appendix B.

4.3 Model Runs

In this section we present the application of the LC model to CR 1913, initialized using a synoptic MDI magnetogram centered on 1996 Aug 27. Occuring during solar minimum, the sun at this time features a conspicuous equatorial coronal hole extending from the north to down past disk-center, as well a large active region. This then conveniently allows us to examine the ability of a given model to describe these three basic regimes: the average quiet-sun, coronal holes, and active regions. Additionally, this rotation has been studied in detail using similar methods (e.g. Mikić et al. (1999); Lionello et al. (2009)) and thus provides a means of comparison to existing work.

Four model runs used to demonstrate the usefulness of the LC model are summarized in Table 4.1. As a convenient comparison of their global thermodynamic and topological properties, the LOS synthesis of EUV and soft X-Ray emission are shown in Figure 4.2. Each of the models presented use either $|B|$ weighted heating (model 1, Section 4.2.2) or exponential heating (model 2, Section 4.2.2). All four use coronal hole heating (Section 4.2.2) applied uniformly to the domain, while all but run C use the open/closed field weighting (Section 4.2.2) to achieve a more realistic equilibrium in these regions. In order to include strong heating in active regions with high magnetic field strength, Run D also includes a modification to the heating function, and transitions smoothly from exponential heating to $|B|$ weighted heating ($Q_h = 4 \times 10^{-5}|B|$ ergs cm⁻³s⁻¹) above 30 Gauss.

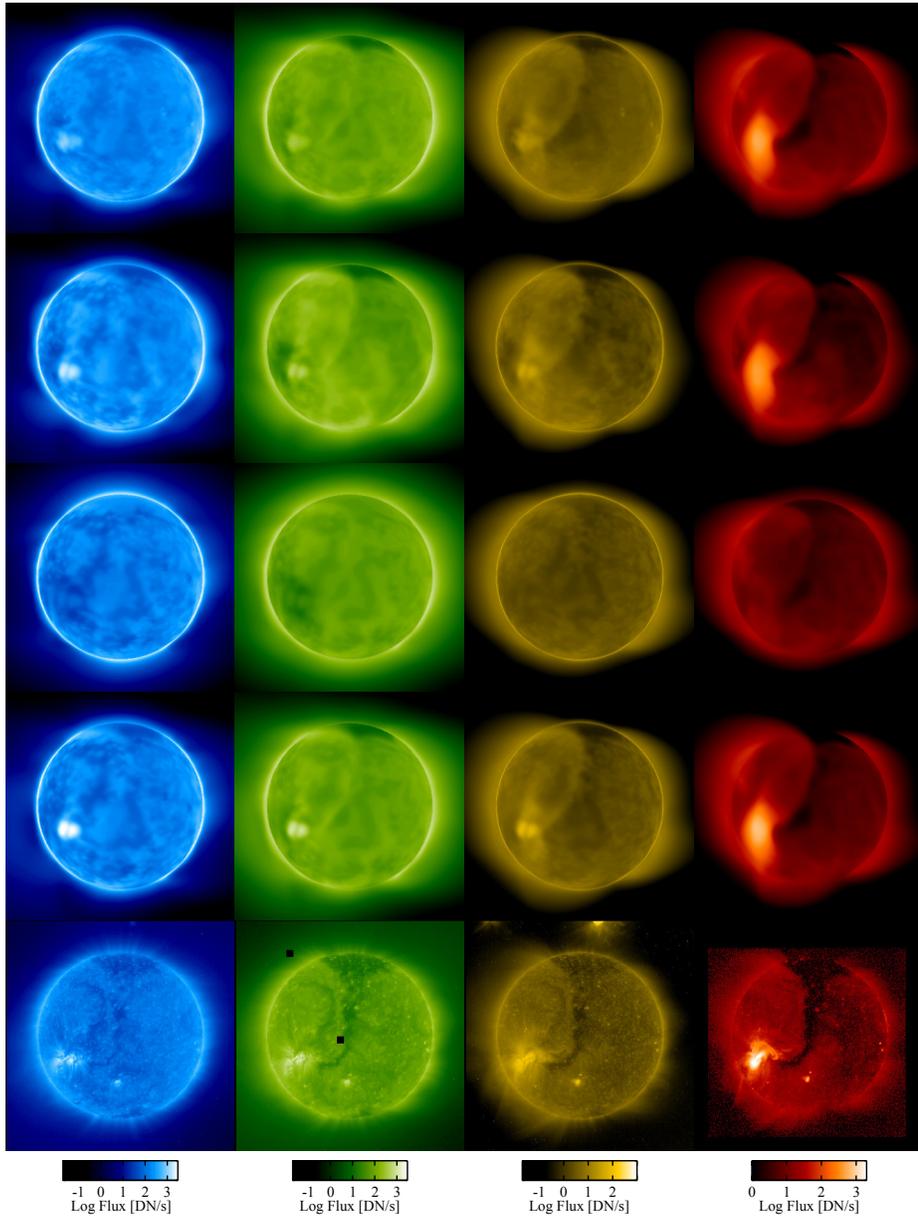


Figure 4.2: Comparison of EIT 171Å, 195Å, 284Å, and SXT AlMg image synthesis to observations for the model runs of CR 1913 centered on 1996 Aug 27. Runs A, B, C, and D are shown top to bottom. Bottom row: SOHO EIT and SXT AlMg observations of the same date near 01:00 UT (00:10:13, 00:24:05, 01:05:19, and 01:07:28 respectively). Run A: REB BC + B weighted heating + Open Field Modification. Run B same as A with chromospheric BC. Run C: Chromospheric BC + uniform exponential heating. Run D: chromospheric BC + Exponential heating + B weighted AR component + open field modification.

Run	BC	Heating	Open Cutoff	Power [ergs s ⁻¹]
A	REB	$\propto B $	Yes	2.88×10^{28}
B	Chromo	$\propto B $	Yes	2.88×10^{28}
C	Chromo	Exp	No	2.49×10^{28}
D	Chromo	Exp + AR	Yes	2.88×10^{28}

Table 4.1: LC Model Heating Parameters For Runs A-D.

All four model runs show similar global features in the EUV and Soft X-Ray when compared to observations but differ on the precise details. For example, all four runs resolve cool temperatures along the the polarity inversion lines near the surface (seen to the east and west of the extended equatorial coronal hole near the center of the disk). This is naturally due to field line orientation and loop length governing thermodynamic equilibrium. This commonality serves to emphasize the strong role that the 3D magnetic field topology of a given Carrington Rotation plays in determining dynamic equilibrium in the corona.

In the comparison between Run A (REB model BC) and Run B (Chromospheric BC) we observe more uniform emission near the surface as well as slightly higher temperature (as seen in the longer extent of SXT emission) for the REB case. Because the boundary is near the top of the transition region in the REB model, the height of the transition region is less able to vary in response to magnitude of the downward heat conduction flux from above. Also, since the REB model does not include a region with chromospheric densities (where the radiative cooling is much higher due to the n_e^2 dependence) a smaller fraction of the coronal heating power is lost in the transition region, leading to higher equilibrium temperatures. However, it is clear that the REB model, which is more suited for computational efficiency due to the longer equilibrium length scales at $T = 500,000\text{K}$, can be used to adequately describe the ambient global corona.

One of the most striking results is perhaps the comparison of Run C to the other model runs. In this run, the coronal heating function was applied uniformly in the computational domain (no dependence on θ or ϕ). While the coronal holes and significant AR emission are unsurprisingly not well preserved in the EUV, still much of the basic features of the low corona are reproduced. The ability of simple uniform heating model to reproduce obvious features on the surface, such as average quiet sun emission, and lessening near inversion lines, as well as the bi-modal structure between open and closed field regions at higher temperatures (284Å line and soft X-Rays) speaks to the importance of both the 3D magnetic topology in determining the dynamic equilibrium of the corona and the redistribution of energy via a thermodynamic energy equation including electron heat conduction.

For a more realistic empirical model in Run D, we modify Run C by including AR heating and the open-field cutoff to better describe heating in active regions in coronal holes. The most interesting finding in this comparison is that by including significantly enhanced heating in the large active region, we observe a pronounced effect on the equilibrium structure of the AR associated closed field/streamer region (Eastern side of the corona in Figure 4.2). This produces noticeable feedback on the global structure as seen via a larger northward tilt of the heliospheric current sheet near the AR longitudes (shown in detail Figure 4.3), and suggests a complex relationship both between the thermodynamics of the low corona and the global structure of the solar wind. Because this effect cannot be fundamentally extracted from extrapolating the magnetic field alone, this provides not only a strong motivation for using thermodynamic models, but also another element with which to constrain and refine AR heating models in future studies (the one used in in this work being a necessary but crude approximation).

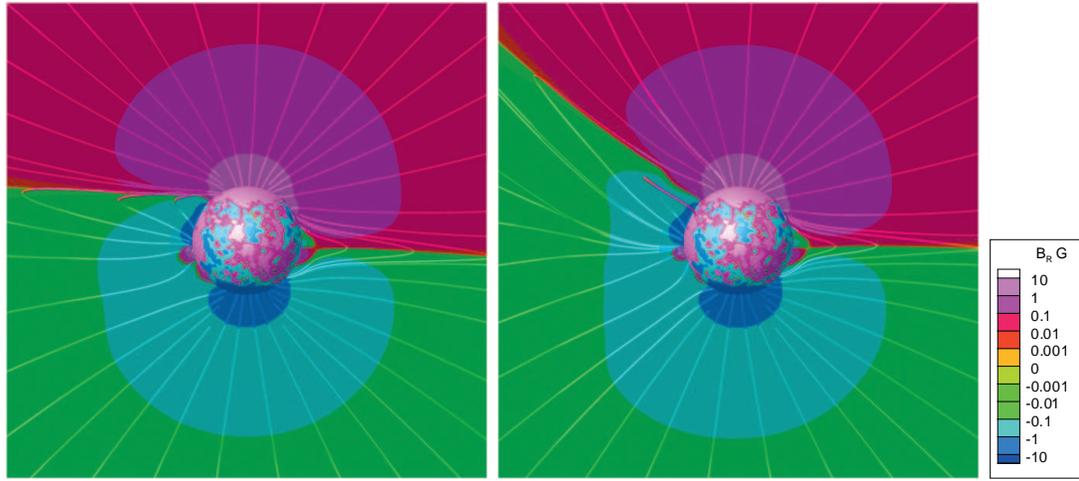


Figure 4.3: Comparison of the significant effect that AR heating has on the tilt of the heliospheric current sheet between Run C (uniform heating, left) and Run D (with AR heating and open field modification, right). The thermodynamic stress induced by significant local heating of the active region ($\sim 7 \times 10^{27} \text{ ergs s}^{-1}$) causes an extreme shift in the northward tilt of the heliospheric current sheet $\sim 35^\circ$. Simultaneously, the region not thermally connected to the active region on the opposite side of the sun remains unchanged. The color contours display the radial component of the magnetic field, B_r . The chosen slice is parallel to the polar axis and intersects the inversion line between the large active region seen on 1996 Aug 27. The 3D magnetic streamlines intersect the slice at the same location in each figure.

Another important inference about coronal heating can be gleaned from the comparison of the two heating models directly (Run B and Run D). Although the total heating power is the same in each model, the $|B|$ weighted heating model naturally has a shorter scale height (due to the falloff of $|B|$ with radius) and we subsequently observe slightly enhanced pressure in the low corona and lower temperatures (hence density scale height) in the closed field regions. However, the fact that the simple exponential heating model applied to the quiet sun in Run D can reproduce the mean structure of the low corona with the same fidelity as a more complicated empirical model, demonstrates that perhaps complex empirical models are not as entirely necessary as some might suggest and motivates a need for more physics based models to advance further.

4.4 Detailed Analysis

In this section we provide a more detailed analysis of Run D in particular. We examine the magnetic and thermodynamic structures realized by the LC model and provide a comparison to the standard SC model (Cohen et al. 2007).

4.4.1 Temperature structure of low corona

An important advantage of including heat conduction in a global 3D environment is the ability to study complex open/closed field topologies in a self consistent manner, which allows one to study the feedback effect that the magnetic topology has on heat distribution and vice versa. The most striking effect can be seen by examining the differences between heat conduction along open or closed field geometries. Because closed field regions represent closed systems for the flow of thermal energy, they achieve higher temperatures than their open-field counterparts and shift into the

soft-Xray regime ($T \sim > 1.5\text{MK}$). This natural correspondence can be clearly seen in Figure 4.4 where we show a 3D surface at fixed temperature ($T_e = 1.6\text{ MK}$) and an LOS image of soft-X-Ray emission.

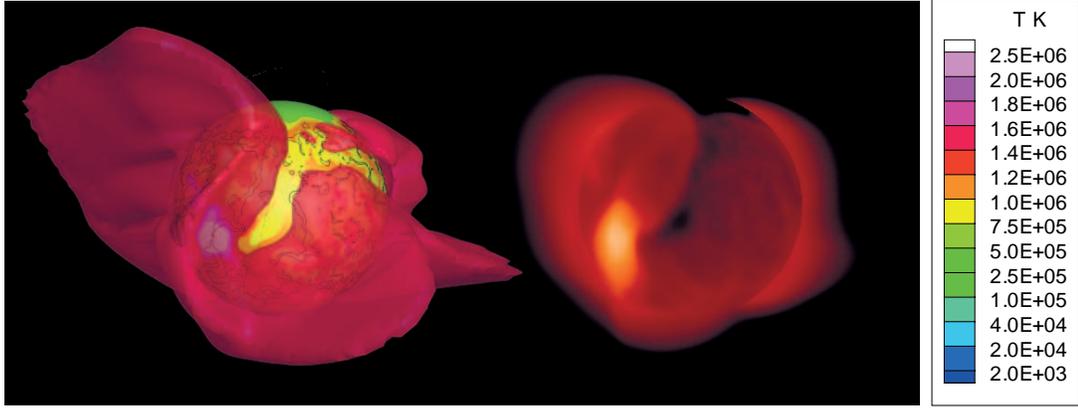


Figure 4.4: Visual comparison of 3D topological structure (left) to LOS synthesis of SXT AlMg response (right) for Run D (Exponential heating + AR heating). The surfaces shown are of constant $r = 1.03 R_{\odot}$ and $T = 1.6\text{ MK}$ with color contours of T . The black contour lines of normal radial field direction $|\hat{B}_r| = 0.2$ are shown to illustrate how the hot, closed field streamer regions overlay the inversion lines on the surface.

4.4.2 Magnetic structure of low corona

It is also important to examine in detail the effect that the thermodynamic model has on the magnetic structure as a whole. In Figure 4.5 we show a comparison between closed field lines at $r = 2.0R_{\odot}$ for the PFSSM initial condition (Altschuler et al. 1977), the standard SC model (Cohen et al. 2007) and Run D. Immediately obvious are the drastic changes between the closed field/streamer structure of the polytropic SC model and the thermodynamic LC model. Unsurprisingly, the high temperatures and thermal energy introduced by coronal heating and conduction along the closed field produces a large thermal stress in the relatively high β regions near the streamer cusps along the current sheet. This in turn leads to significant reorganization of the magnetic field as compared to a PFSSM or polytropic MHD model. The fact

that this sort of stress is highly sensitive to both the local nature of a given coronal heating model (Figure 4.3) and the global magnetic topology (Figure 4.5) is a leading motivation for using a fully 3D, thermodynamic model when studying the structure of the global corona.

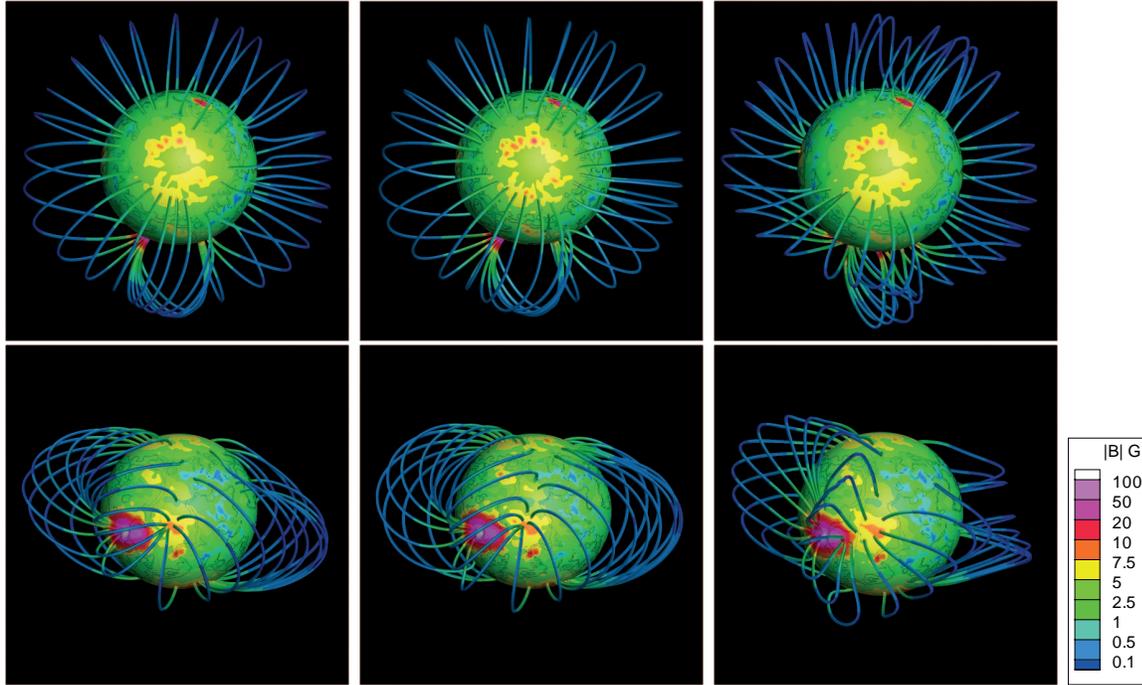


Figure 4.5: Magnetic field comparison of the streamer structure of CR 1913 between 3 different models, from a top down (top) and Earth-centered viewpoint (bottom) at 01:00 UT 1996 Aug 27. Left: The PFSSM initial condition (Altschuler et al. 1977). Middle: Steady state equilibrium of the default SC model (Cohen et al. 2007). Right: Steady state of Run D (Exponential heating + AR heating). It is immediately clear that the closed field structures become highly stressed by heating near the surface and the subsequent redistribution via heat conduction. Selected field lines are chosen at near equal intervals along the intersection of $r = 2.0R_{\odot}$ and $|\hat{B}_r| = 0.5$ in each model.

4.4.3 EUV and Soft X-Ray comparison

In Figure 4.6 we show LOS EUV and Soft-X-Ray image synthesis comparisons between run D and the standard SC model. In Figure 4.7 we show two quantitative slice comparisons cutting an average quiet sun region and the large active region. The

improved agreement of Run D in multiple filter bands is indicative of the improved temperature resolution possible with the LC model. While not an entirely fair comparison because the standard SC model does not include a full energy equation, we demonstrate the ability to quantitatively assess the relative agreement between a given model and observations in the EUV regime. This sort of comparison also allows one to study in detail various choices of heating models and, through multi-filter comparison, provide a basis to resolve the inherent degeneracies between modifying the total coronal heating power and the heating scale height within the model. A further examination of some of the limitations imposed by EUV synthesis from MHD models with finite resolution as well as future considerations can be found in appendix C.

4.4.4 Thermodynamic Comparison

It is also instructive to examine the global temperature and density structure as a function of height for both Run D and the standard SC model. In Figures 4.8 and 4.9 we show electron temperature and number density at three separate heights in the low corona. Important to emphasize is the fact that with a thermodynamic model, it is possible to resolve both significant changes in temperature with height and with respect to the magnetic field topology in the model. As expected, near the top of the transition region Run D resolves cooler temperatures near the inversion lines due to the short loop length, while simultaneously higher in the corona, hotter temperatures ($T > 1.5\text{MK}$) are achieved in close field regions, a natural result of energy flowing on a closed path via heat conduction. This greater sensitivity to field geometry (something difficult for a polytropic model to do without extreme fine tuning of boundary conditions) is critical when trying to correctly describe the conditions in the low corona.

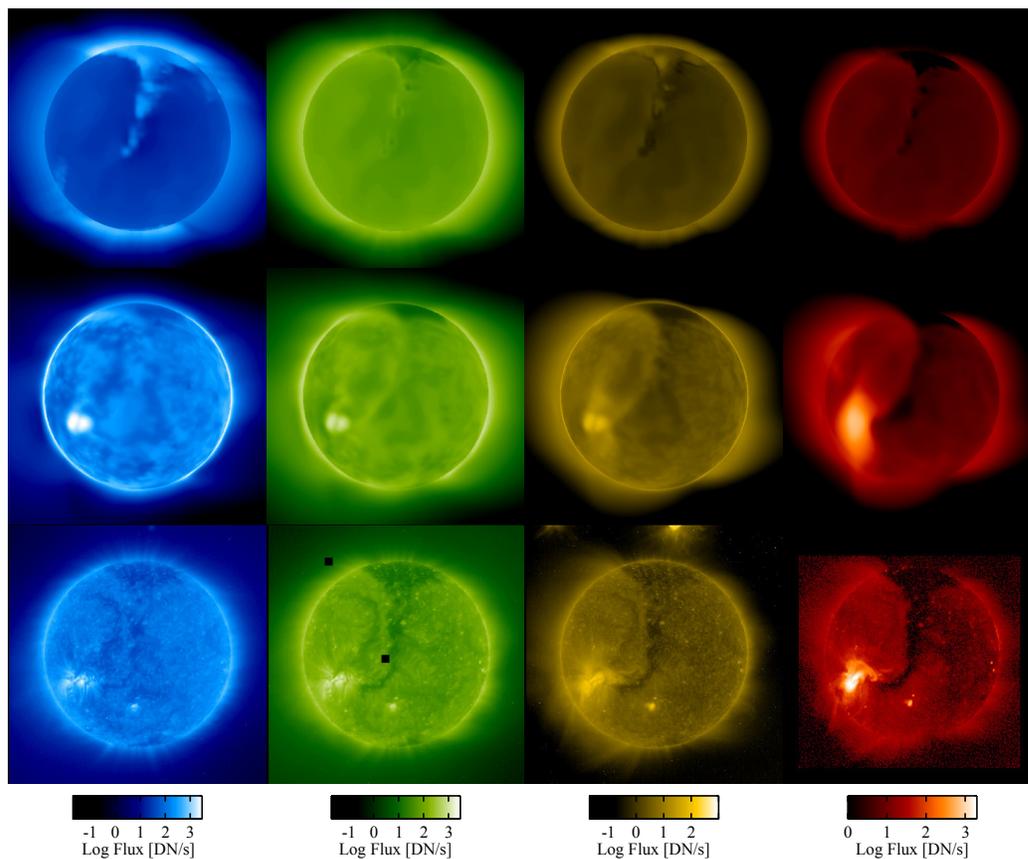


Figure 4.6: Comparison of EIT 171Å, 195Å, 284Å, and SXT AlMg image synthesis to observations for 1996 Aug 27. *Top row:* steady state of the standard SC model (Cohen et al. 2007). *Middle row:* Run D (Exponential heating + AR heating), demonstrating significantly improved agreement with surface conditions and streamer topology. *Bottom row:* SOHO EIT and SXT Almg observations of the same date near 01:00 UT (00:10:13, 00:24:05, 01:05:19, and 01:07:28 respectively).

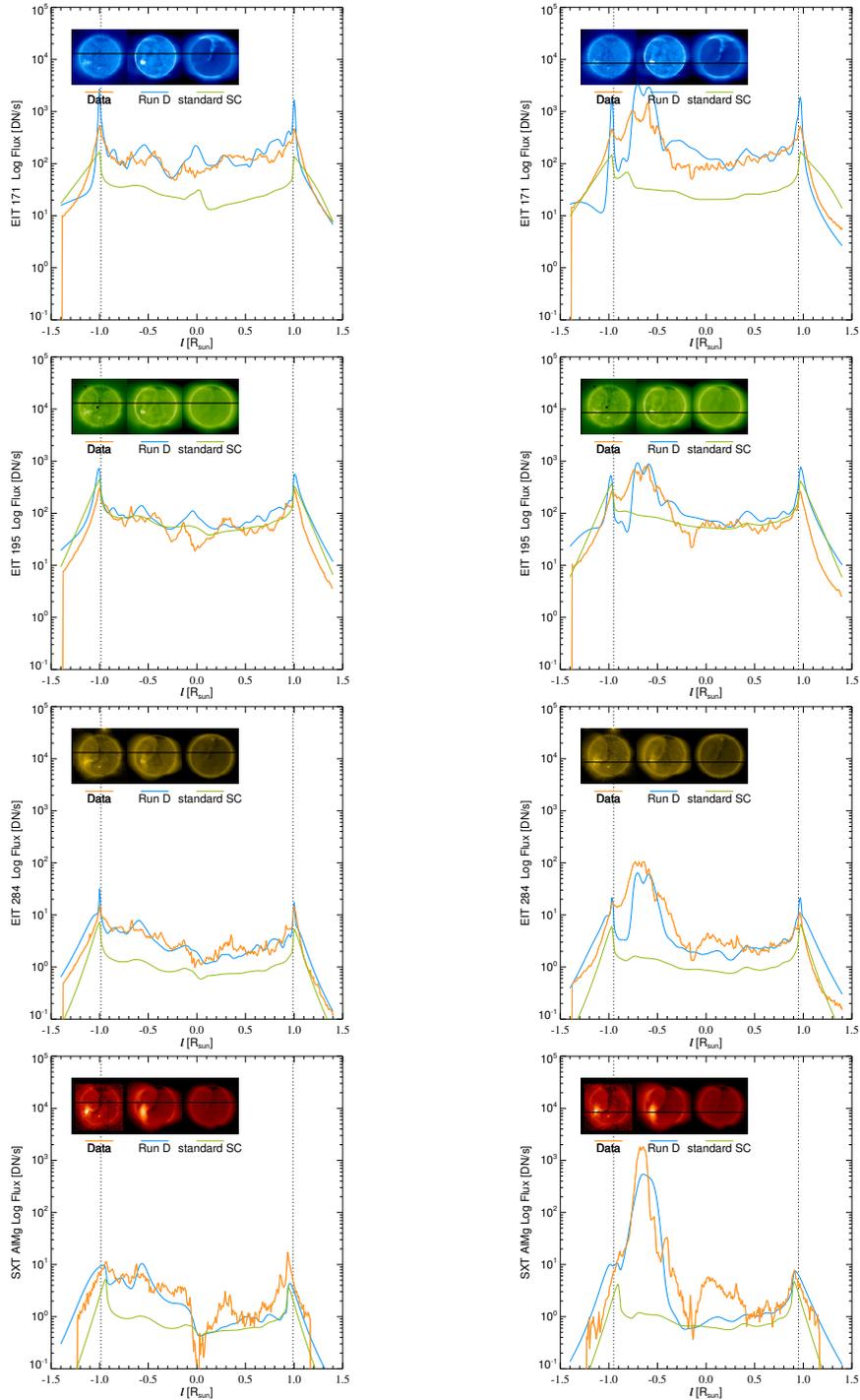


Figure 4.7: Quantitative slice comparison of EIT 171Å, 195Å, 284Å, and SXT AlMg synthesis from Run D (blue), the standard SC model (green), and observations (orange). The slices are chosen to include the average quiet Sun (left) and a large active region (right) observed on the disk.

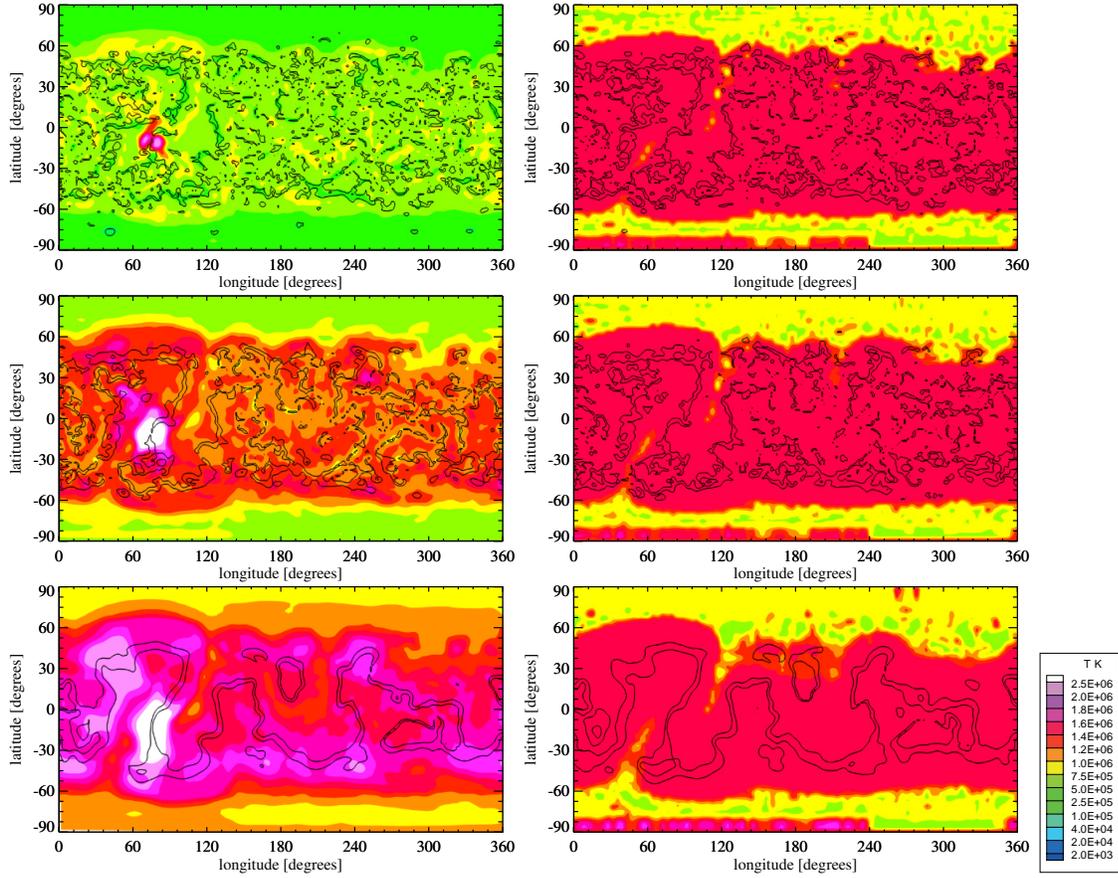


Figure 4.8: Temperature contours at $r = 1.01$ (top), 1.03 (middle), and 1.10 (bottom) R_{\odot} for run D (left) and the default SC model (right) for CR 1913 (Black lines at $|\hat{B}_r| = 0.2$). The full thermodynamic energy equation is able to capture large changes in temperature over short changes in radius. As expected, near the top of the transition region we resolve cooler temperatures near the inversion lines due the short loop length. Simultaneously higher in the corona, hotter temperatures ($T > 1.5\text{MK}$) are achieved in close field regions, a natural result of energy flowing on a closed path via heat conduction.

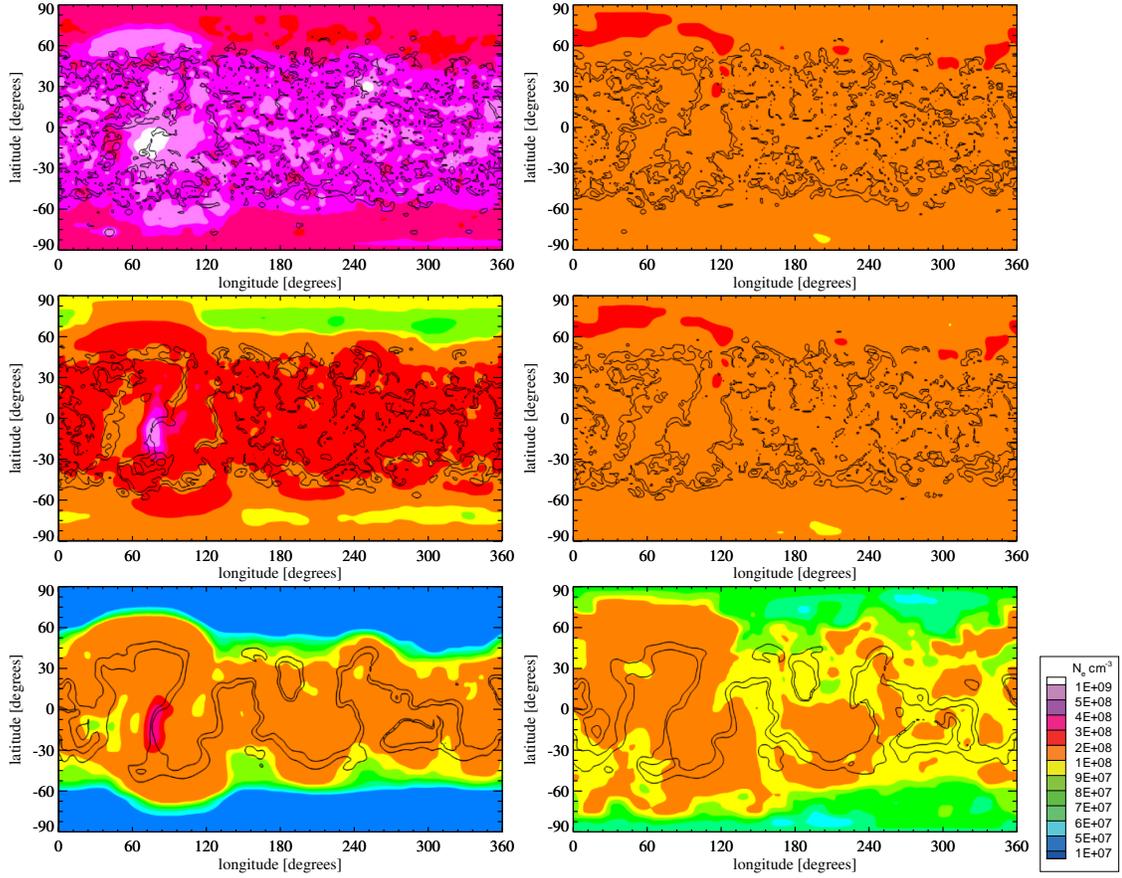


Figure 4.9: Electron density contours at $r = 1.01$ (top), 1.03 (middle), and 1.10 (bottom) R_{\odot} for run D (left) and the standard SC model (right) for CR 1913 (Black lines at $|\hat{B}_r| = 0.2$). This demonstrates the high dynamic range in density over small changes in radius resolved with the LC model.

4.5 Conclusion

In this chapter we demonstrate the clear need for a self-consistent treatment of the thermodynamic energy equation and boundary conditions when studying the global properties of the low corona with an MHD model. We observe that the interplay between coronal heating and electron heat conduction strongly governs the details of important structures in the low corona, which is something that cannot be described by extrapolation of the magnetic field on its own (e.g. the significant stress of the streamer regions and current sheet in response to active region heating seen in Figures 4.3 and 4.5). We also showcase the ability of the LC model to examine the effectiveness and applicability of various heating functions, and find that a simple exponential heating profile does quite well in describing the average structure of the quiet sun.

With this foundation, we believe that the LC model can provide a more realistic vehicle with which to study a wide range of aspects of the dynamic corona and solar wind. For example, the time-dependent dynamics of any sort of transient event in the corona, such as a CME or EUV wave, depend critically on the magnetic and density structure of the corona (density scale height being highly sensitive to temperature) and therefore it is important to use improved models when determining the global ambient medium in which they evolve. Additionally because of the general flexibility of the SWMF, future coupling of the LC model to complementary solar wind models, such as the SC model based on a full description of Alfvén wave turbulence currently in development (Oran et al. 2009, in press), or one including a multi-species treatment to resolve electron/ion temperature decoupling in the high corona, has become a feasible scenario.

Chapter 5

Case Study 1: 2008 March 25 EUV wave

Abstract

With the refined physics and methods developed for the LC model in hand, we can now turn to the main science driver of the dissertation: understanding the nature of EUV waves. In this chapter, we document our effort to explore the signatures of large scale EUV transients in the Solar Corona (EUV waves) using the our 3D thermodynamic Magnetohydrodynamic model (Chapter 4). We conduct multiple simulations of the 2008 March 25 EUV wave ($\sim 18:40$ UT), observed both on and off of the Solar disk by the STEREO-A and B spacecraft. By independently varying fundamental parameters thought to govern the physical mechanisms behind EUV waves in each model, such as the ambient magneto-sonic speed, eruption free-energy, and eruption handedness, we are able to assess their respective contributions to the transient signature. A key feature of this work is the ability to synthesize the multi-filter response of the STEREO EUVI imagers directly from model data, which gives a means for direct interpretation of EUV observations with full knowledge of the 3D magnetic and thermodynamic structures in the simulations. We discuss the implications of our results with respect to some commonly held interpretations of

EUV waves (e.g. fast-mode magnetosonic wave, plasma compression, reconnection front, etc.) and present a unified scenario which includes both a wave-like component moving at the fast magnetosonic speed and a coherent driven compression front related to the eruptive event itself.

5.1 Introduction and Background

As mentioned in Section 2.3, the highly non-linear temperature and density dependence of commonly observed coronal emission lines (e.g. Fe IX 171Å, XII 195Å, and XV 284Å) combined with line-of-sight projection effects inherent when observing optically thin EUV coronal structures often makes interpretation of conspicuous phenomena difficult.

This could not be more true for EUV waves (Section 2.6), where despite over a decade of continuous observations by SOHO EIT, their physical mechanisms have remained elusive. Ultimately one thing is clear: because the dynamics of wave propagation speed and shock formation depend highly upon the local sound and Alfvén speeds, the thermal-magnetic structure of the corona is critically important for any EUV wave theory. Combining these elements in a fully dynamic model to probe non-linear or non-wave scenarios in unison is then critical in furthering our ability to construct and constrain a theoretical framework for these events. Moreover, it is equally important for the results of any EUV wave scenario to be directly interpreted in the context of actual observations. From this perspective, we present a series of simulations of a realistic EUV wave using a global 3D thermodynamic Magnetohydrodynamic (MHD) model of the corona. We examine the effect that three key variables (eruption strength, eruption handedness, and ambient quiet-Sun magnetosonic speed) have on the ensuing transient signature, which is synthesized for

direct comparison to observations. While in a sense we are changing these parameters to “see what happens”, in our minds this is a critical use of computational models, i.e. as an ideal laboratory to study physical mechanisms in a controlled manner.

In Section 5.2 we describe the observations of the 2008 March 25 EUV wave transient, the prototypical event that we have chosen. In Section 5.3 we describe the 3D MHD model and methods used in this work. Sections 5.4 and 5.5 describe the simulation runs and our interpretation of their results. We conclude in Section 5.6.

5.2 Observations

5.2.1 The 2008 March 25 EUV wave event

The focus of this work is the conspicuous EUV wave transient that occurred on 2008 March 25 around 18:40 UT, with the eruption/flare site centered on NOAA Active Region 10989. Observed directly by the Sun Earth Connection Coronal and Heliospheric Investigation (SECCHI) instruments (Howard et al. 2008) onboard the Solar TERrestrial RELations Observatory (STEREO) A and B spacecraft pair (Kaiser et al. 2008) as well as the SOHO spacecraft, this event produced a GOES M1.7 class flare and was associated with a modest CME (Aschwanden 2009; Patsourakos et al. 2010a). With STEREO-A and B separated at this time by $\sim 47^\circ$, the twin Extreme-UltraViolet Imager (EUVI) (Wuelser et al. 2004) onboard produced synced observations of the entire event in four EUV filters at a high cadence (~ 2.5 min cadence for the Fe IX 171Å and He II 304Å filterbands, and 5 min cadence for the Fe XII 195Å and Fe XV 284Å filterbands). This arrangement afforded a dynamically rich view of the event, seen in projection both off of the east limb (STEREO-A) and on the disk (STEREO-B). At this time the erupting AR was only slightly behind the

east limb as seen by STEREO-A. This afforded optimal viewing conditions of the transient evolution off of the limb of the solar disk and highlights the north/south propagation of the transient. For this reason we choose focus on the EUVI-A data set in this work. Five minute running ratio snapshots, created by dividing the pixel by pixel flux of an EUVI image by a preceding image nearest to a given time interval, are shown for EUVI-A observations in the 171, 195, and 284Å filters for the first 45 minutes of the event in Figure 5.1.

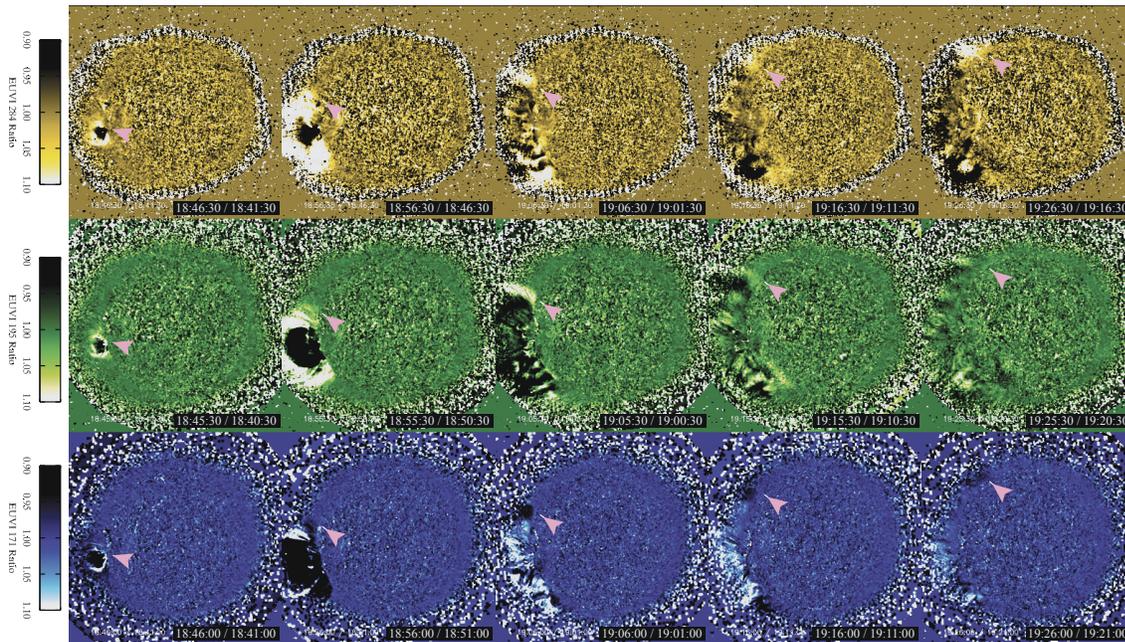


Figure 5.1: Running ratio images at five minute intervals for the first 45 minutes of the 2008 March 25 EUV wave event in the EUVI 171Å (bottom) 195Å (middle) and 284Å (top) wavebands. The approximate location of the northward propagating front at each time is shown with an arrow. The speckled pattern beyond $r \sim 1.3 R_{\odot}$ is due to photon noise and data compression. As is characteristic of EUV wave transients, these observations show a diffuse front expanding over large transverse distances within a short period of time. There is also a clear anti-correlation of the sign of the perturbation between the 171Å filter and 195Å and 284Å filters within the front. Note that the second and last frames for the 284Å filter are shown as a 10 minute running ratio due data gaps.

The running ratio method (the same as that used by Patsourakos et al. (2009)) is chosen because ratios highlight relative changes in photon flux that are independent

of the absolute flux value, unlike the more commonly used difference technique that compares a flux difference (e.g. Dai et al. (2010); Gopalswamy et al. (2009); Wills-Davey et al. (2007)). This makes ratio images effective for visualizing the EUV wave signal off of the Solar disk, where EUV flux drops off drastically (note that the emission of the Fe lines contributing to the EUVI filters is proportional to electron density squared in the collisional regime of the low corona). This implies that running ratio images effectively divide out the density dependence of the transient as a function of height, whereas running difference images do not. In the context of this analysis, we choose running ratios as opposed to base ratios (where each image is divided by a pre-event image) in order to best focus on the large-scale evolution of the transient with respect to itself at large distances. While base methods applied to limb events are optimal for studying coronal dimming and determining CME mass (e.g. Aschwanden et al. (2009)), they are not appropriate for studying the evolution of the extended EUV wave front away from the source region at times beyond ~ 20 minutes of the beginning of the event. This is due to the non-negligible rotation of extended structures off of the limb adding spurious contributions to the measurement that grow in amplitude with time for base methods, while this contribution is fixed for running methods. Additionally, to enhance the large-scale properties of the event and smooth out the effects of photon noise off of the limb, we perform Gaussian convolution of each EUVI image with a half width of $\sigma = 0.005 R_{\odot}$ (~ 3 pixels) before calculating the ratios. A prototypical EUV wave event, this event is characterized first by an outward hemispherical enhancement front and strong dimming in the eruption region. As the outward front leaves the field of view of the instrument, the transient retains a conspicuous transverse component in the form of a wave-like diffuse front that reaches the northern coronal hole at around $t \sim 19:15-19:30$ UT.

5.2.2 Time-Distance limb diagrams

One of our main tools for analysing the dynamics of the 2008 March 25 EUV wave is the time-distance diagram. Analogous to the time-elongation plot commonly used to track CME's with coronagraph observations (e.g. Sheeley et al. (2008); Lugaz et al. (2009)), we construct these diagnostics by first extracting the EUV signal along Sun-centered circular arc of radius $r = 1.1 R_{\odot}$ off of the East limb for every image in the dataset. The ratio of the EUV flux along this arc to the flux for the preceding image for a given filter is then calculated. These ratios now form a 2D grid with distance, s , along the arc as the x-axis and time as the y-axis, from which the speed of the projected bright EUV front at a given radius can be directly calculated from the slope. A schematic of this process is shown in Figure 5.2 (left), and the time-distance limb diagrams for the EUVI-A 171, 195, and 284Å filters are shown in Figure 5.2 (right).

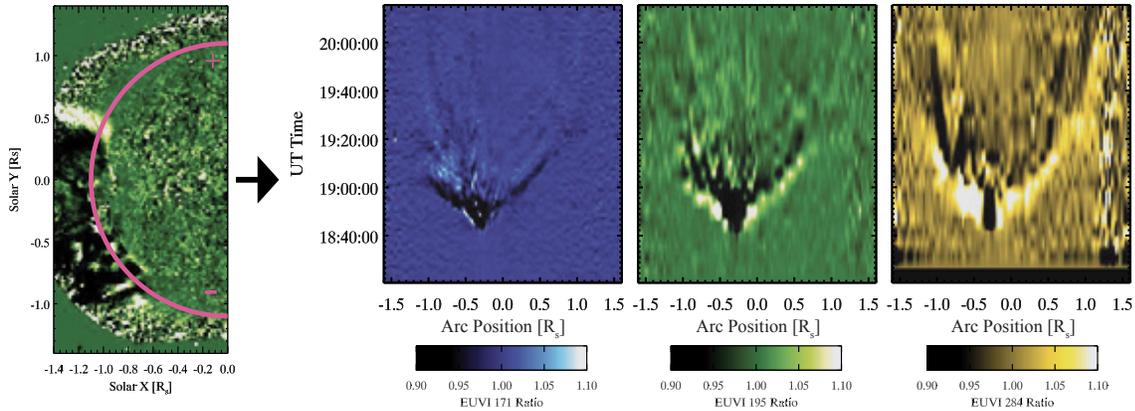


Figure 5.2: Time-distance diagrams of the EUV transient observed by EUVI-A off of the limb for the EUVI-A 171Å, 195Å, and 284Å filters. The x-axis, shown schematically as the magenta arc in the left inset, represents the position along an arc of constant radii, $r = 1.10R_{\odot}$, that spans the east limb with the equator as the zero point. The coloring of the time-distance diagrams (right) represents the flux ratio of the preceding image for points on this arc. Note that the cadence for the 171Å was 2.5 min while the cadence for then 195Å and 284Å filters was 5 min (except for 10 minute gaps for times $t = 18:56:30$ and $19:26:30$ for the 284Å filter). The aspect ratio is achieved through linear interpolation of the time-coordinate.

Immediately apparent upon examination of the EUVI-A time-distance diagrams is both the apparent speed (common in all three) and contrasting amplitudes for a fixed location between each filter (i.e. temperature window). Towards the north pole (positive x-axis) the 171 and 195Å filters exhibit anti-correlated behaviour, suggestive of a heating/relaxation period where the average temperature within the bright front is enhanced and subsequently cools as the transient passes. A simple estimate of the slope of the maximum enhancement in the 284Å filter between the points $s_1 = 0.18 R_\odot$ and $s_1 = 0.56 R_\odot$ gives a front speed of $\sim 350 \text{ km s}^{-1}$, although this measurement is limited mainly by ratio cadence and inherent uncertainty in the flux values due to the ambient evolution of the corona. We show a zoomed in view of the time-distance diagrams for the northward front with an overplotted speed range to demonstrate these features in Figure 5.3.

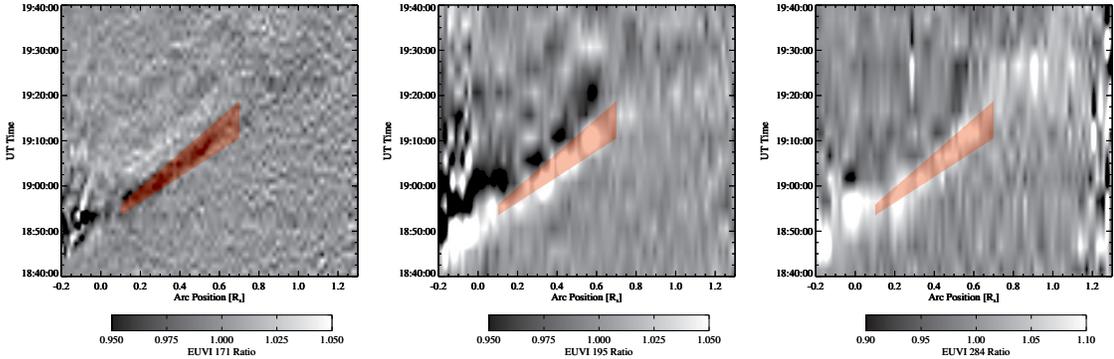


Figure 5.3: Time-distance diagrams of the EUV transient zoomed in on the northward front for the EUVI-A 171Å, 195Å, and 284Å filters. The red transparent polygon represents the a range of $350 \pm 50 \text{ km s}^{-1}$ overplotted on the front between $s = 0.1$ and $0.7 R_\odot$, and is displayed at the same location in each frame. The slope of the polygon is defined by the bounding speed range while the width in time is defined by the time interval needed to travel at these speeds to $s = 0.1$ from $s = -0.15 R_\odot$, the approximate origin of the event from this point. Here we see the slope of the perturbation falls within this speed interval, and that the anti-correlated nature of the 171Å perturbation to that in 195 and 284Å in space and time along the front is clearly visible.

5.3 Numerical Model

The numerical tool used in this work is the Lower Corona (LC) component of the Space Weather Modeling Framework (SWMF), a fully parallelized, customizable 3D MHD modeling framework (a general overview can be found in Tóth et al. (2005)). Details of the development and application of the LC component, which includes considerations relevant to resolving the thermodynamics of the low corona and transition region (e.g. radiative loss, field-aligned electron heat conduction, and empirical coronal heating in the energy equation), can be found in Downs et al. (2010). A critical feature of this tool and its previous iterations (e.g. Roussev et al. (2003b); Cohen et al. (2007)) is the ability to include synoptic magnetic observations of any Carrington Rotation (CR, standard solar rotation number) as boundary condition and basis to extrapolate the 3D magnetic field permeating the corona. This provides a means to study the conditions that are observed in the corona directly with an MHD model. For our simulations, the initial magnetic field configuration and boundary conditions are extrapolated via the Potential Field Source Surface Method (PFSSM) (Altschuler et al. 1977), using high order radial magnetic coefficients derived from observations by the MDI instrument aboard the SOHO observatory for CR 2068 centered on 2008 March 25.

A particular advantage of the LC component is the ability to achieve realistic equilibrium temperatures and densities in the low corona without a strong dependence on the choice of boundary conditions. Here the solar boundary is set in the chromosphere with characteristic values of electron density, n_e and temperature, T_e , ($n_{e,0} = 1 \times 10^{12} \text{ cm}^{-3}$, $T_{e,0} = 4 \times 10^4 \text{ K}$) and a widened transition region is resolved by modifying the ratio of heat conduction to radiative cooling at temperatures below 300,000 K (see Lionello et al. (2001, 2009) for details.) In this case, thermodynamic

balance in the corona is achieved self-consistently due to the interplay between magnetic topology and thermodynamic energy balance in the transition region. This then lends itself naturally to directly calculating the expected EUV emission of the model corona (a strong function of local n_e and T_e) and using this to validate the results for a specific time relative to spacecraft observations in the EUV regime (Downs et al. 2010). The important details and modifications to the LC model for the study of EUV wave transients are described below.

5.3.1 Line-of-sight image synthesis

Perhaps the most important diagnostic to characterize our model results is the synthesis of EUV images for one-to-one comparison to spacecraft observations. The process for creating these images from 3D simulation data for the SOHO EIT and Yohkoh SXT instruments is well described by Mok et al. (2005); Lionello et al. (2009) and the particular application of this method to the LC model is described in Downs et al. (2010). To build upon this foundation, we implement the ability to synthesize observations for the modern EUVI instruments onboard the STEREO-A and B spacecrafts as well as the X-Ray Telescope (XRT) onboard the Hinode spacecraft. This process is summarized as follows: a spectrum including continuum processes and optically thin emission lines important in the Soft-Xray to EUV regime ($1 - 450\text{\AA}$) is calculated for each point on a 2D grid of n_e and T_e using the CHIANTI emission line analysis code (Landi et al. 2006) (values ranging from $10^5 < n_e < 10^{12} \text{ cm}^{-3}$ and $10^{4.5} < T_e < 10^8 \text{ K}$.) For this step we use the composite abundance file `sun_coronal_ext.abund` and the composite ionization equilibrium file `arnaud_raymond_ext.ioneq` (distributed with the CHIANTI database) to calculate these spectra. Then, using the calibration data for the EUVI and XRT instruments

provided by the SECCHI and Hinode teams to the SolarSoft framework (Freeland & Handy 1998), we calculate the expected response per pixel, $R_i(n_e, T_e)$, for a unit column emission measure (EM, units of cm^{-5}) for each specific instrument and filter (we model the EUVI 171Å, 195Å, 284Å, and XRT Ti-Poly filters in this work). The total flux measured by a pixel then takes the form of

$$F_{los} = \int n_e^2 R_i(n_e, T_e) dl \quad [\text{Counts s}^{-1}] \quad (5.1)$$

where the integral is carried over the unique line-of-sight of the pixel through the corona, and the unit of measurement, ‘Counts’, depends on the particular choice of units for $R_i(n_e, T_e)$. As an additional aid in decoupling the temperature dependence of these diagnostics, we also produce images of the integrated column emission measure for each pixel, which amounts to using the same synthesis method with $R_{EM}(n_e, T_e) = 1 \times 10^{-26} \text{ cm}^{-5}$. To avoid integrating through artificially high emission measure regions which are produced in the widened transition region, we cut off each response function for temperatures below $T_e = 400,000 \text{ K}$. The temperature dependence of $R_i(n_e, T_e)$ for each filter at fixed value of n_e is shown in Figure 5.4.

5.3.2 Heating Model

As a proxy for the as yet unknown mechanisms of coronal heating we include a simple but effective multi-component empirical coronal heating source term to the MHD energy equation in order to achieve acceptable agreement of the relaxed MHD configuration to EUV observations. This term takes the form $Q_{total} = Q_{qs} + Q_{ch} + Q_{ar}$. The first two terms are identical to those previously explored by Downs et al. (2010) and use a simple exponential decay model of the form $Q_h = H_0 \exp[-(r - R_\odot)/\lambda]$.

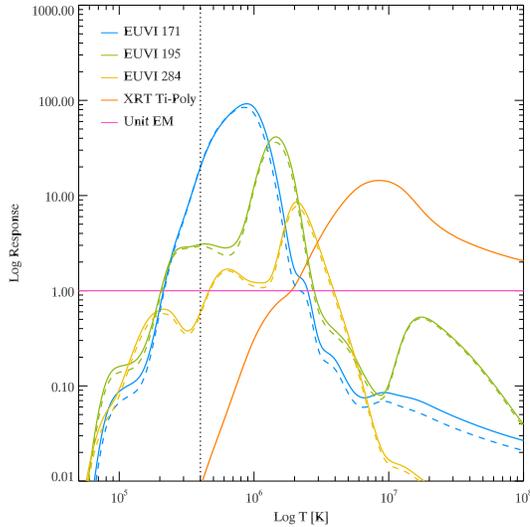


Figure 5.4: Temperature dependence of the filter response functions $R_i(n_e, T_e)$ for a fixed value of electron density, $n_e = 1 \times 10^8 \text{ cm}^{-3}$. These functions used to generate the synthetic images for each run. The slightly differing response functions for the EUVI-A (solid) and EUVI-B (dashed) are also shown. The units of $R_i(n_e, T_e)$ are $10^{-26} \text{ photons s}^{-1} \text{ cm}^{-5}$, $10^{-26} \text{ DN s}^{-1} \text{ cm}^{-5}$, and 10^{-26} cm^{-5} for three EUVI filters, the XRT Ti-Poly filter, and the unit emission measure diagnostic respectively. To neglect the unrealistic emission measure contribution of the widened transition region we set the $R_i(n_e, T_e) = 0$ to the left of the dotted line at $T_e = 400,000 \text{ K}$.

Before further discussing the individual heating terms, it is worth noting here that due to a) the significant amount of computation required to advance a time-dependent 3D thermodynamic MHD model and b) the lack of a universally agreed upon first-principles coronal heating mechanism, we must necessarily use an empirical parametrization to represent coronal heating within the model. The previous work of Lionello et al. (2009); Downs et al. (2010) explore heating functions in this context, demonstrating a favorable agreement with EUV observations through quantitative comparisons, and we base the heating functions and their parameter values on their results. Although in an ideal situation we would not hand-pick parameter values, a further refinement of these parameters through a rigorous deterministic approach, through e.g. a statistical Monte Carlo technique, would require a currently infeasible amount of computation time and would not be guaranteed to provide additional

physical insight due to the inherently empirical and parametrized nature of the heating terms. With this sentiment in mind, a description of our chosen empirical heating terms and their physical purpose is given below.

Q_{qs} is intended to represent the average heating of closed field (quiet-Sun) systems in the corona, with heating concentrated near the base of the corona (small scale-height). We choose parameters $H_{0,qs} = 7.28 \times 10^{-5}$ ergs cm⁻³ s⁻¹ and $\lambda_{qs} = 25$ Mm, and apply this term to closed field regions only, which is determined from a ray-tracing of the initial PFSSM extrapolation of \vec{B} (described below).

The Q_{ch} term is an attempt to grossly approximate the average effect of wave-heating mechanisms of the solar wind. Using parameter values of $H_{0,ch} = 5.00 \times 10^{-7}$ ergs cm⁻³ s⁻¹ and $\lambda_{ch} = 0.7 R_{\odot}$, this long scale height heating term allows both for relatively low densities and temperatures within coronal holes near the Sun ($n_e \sim 5 \times 10^7$ cm⁻³, $T_e \sim 900,000$ K, for $r = 1.04 R_{\odot}$), and reasonable temperatures ($1 < T_e < 2$ MK) at distances beyond $r = 2.0 R_{\odot}$. This term is applied uniformly.

The last heating component, Q_{ar} is designed to represent the presence of strong heating in active regions, particularly near loop footpoints and the polarity inversion region. Differing from the purely $|B|$ -weighted form presented in Downs et al. (2010), this term is motivated by the linear relationship of loop heating to the ratio of basal field strength to loop length derived by Pevtsov et al. (2003) (also explored by Schrijver et al. (2004)). To implement this, we use an initial ray-tracing of the 3D magnetic field to correlate a cell in 3D space to its specific mapping on \vec{B} to the Solar boundary at $r = 1.00$. Once determined, the boundary field magnitude is interpolated to this position and used to determine the strength of the heating term according to

$$Q_{ar} = \sum_{i=1}^2 H_{ar} \exp(-L_i(\vec{x})/\lambda_{ar}) \quad , \quad H_{ar} = H_{0,ar} \min \left[\frac{B_{s,i}}{L_h}, \left(\frac{B_s}{L_h} \right)_{max} \right] \quad (5.2)$$

where the index i sums over each direction of the loop, $L_i(\vec{x})$ is the length of the loop traced from location \vec{x} in the i^{th} direction (parallel and anti-parallel to \vec{B} respectively), L_h is the total loop half-length ($L_h = (L_1(\vec{x}) + L_2(\vec{x}))/2$), $B_{s,i}$ is the magnitude of the magnetic field strength where the trace intersects the boundary, $H_{0,ar} = 1 \times 10^{-2}$ ergs cm $^{-3}$ s $^{-1}$ sets the minimum AR heating rate, $\lambda_{ar} = 20$ Mm defines the heating scale height and $(B_s/L_h)_{max} = 20$ Gauss Mm $^{-1}$, sets the maximal AR heating threshold. We find that this provides hot, high density plasma in equilibrium within the active region, and thus yields adequate results both when comparing active region emission on and off of the solar disk for the high temperature filters (284Å and Ti-Poly). As a validation of the ability of this composite heating function to capture the thermodynamic state of the corona for 2008 March 25, a comparison of the synthetic images produced from our baseline run, Run A, to EUVI observations is shown in Figure 5.5 (details of this run are described in Section 5.4).

5.3.3 Eruption Model

In order to generate a strong EUV transient in our simulations we use an eruption model that is tailored to the asymmetric conditions that occur regularly in the solar corona. Additionally, because our specific goal is to synthesize EUV images from time dependent results and compare these to observations, it is critical that this model does not impose unrealistic temperature and density profiles at the source region.

We choose to use a form of the charge shearing eruption method introduced in Roussev et al. (2007) and further studied for an idealized configurations by Jacobs

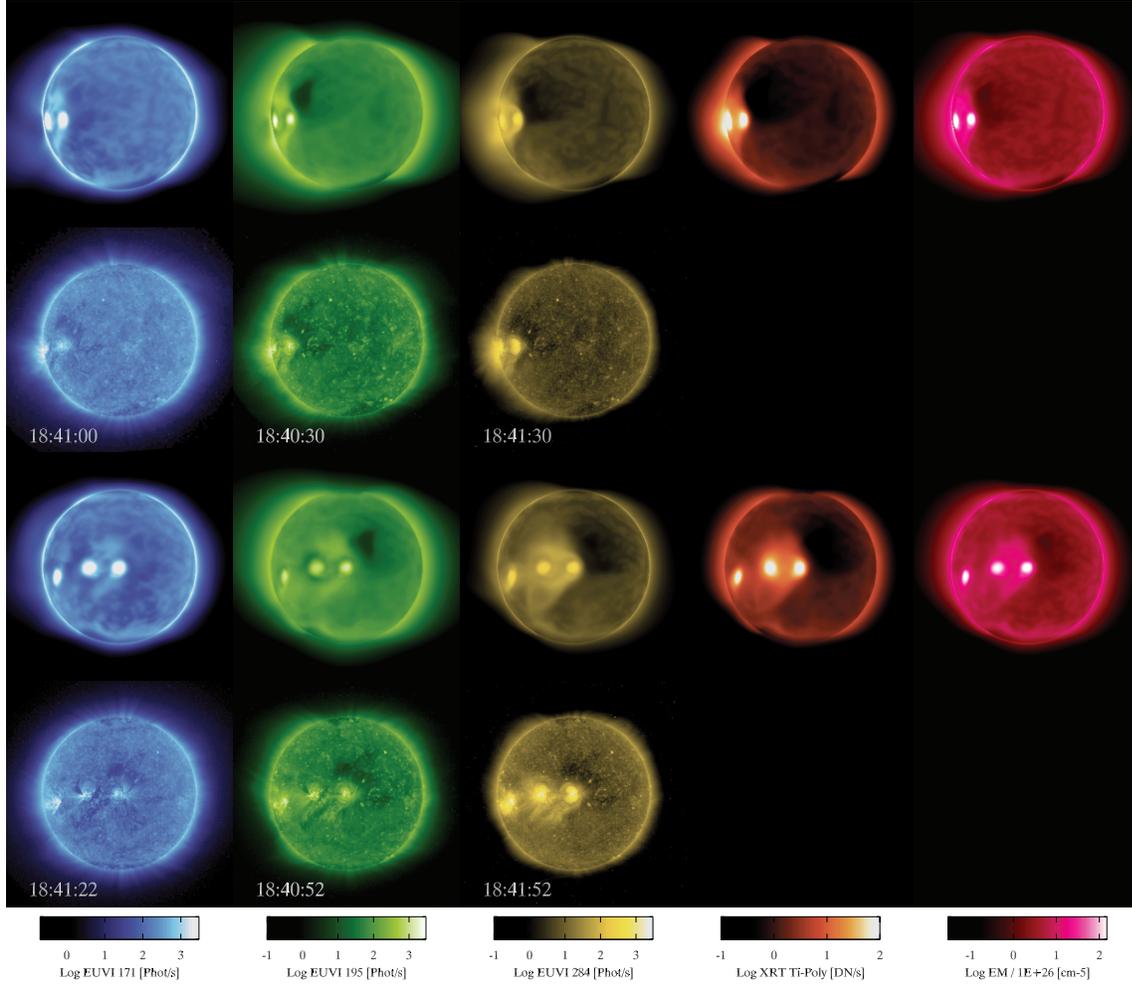


Figure 5.5: Comparison of synthetic LOS images for simulation Run A to EUVI-A (upper half) and B (lower half) observations. Shown in columns from left to right are: EUVI 171Å, 195Å, 284Å filters, XRT Ti-Poly filter, and integrated emission measure. We use the synthetic XRT observations from these vantage points as a high temperature diagnostic (note that $R_{Ti-Poly}$ is within 20% of its maximum for $T_e \sim > 2.8 \times 10^6 \text{K}$).

et al. (2009). In the bipolar version, additional magnetic flux is added to the positive and negative polarities of the approximate bipole comprising AR 10989 in the form of two magnetic charges, $+q$, and $-q$ (denoted q_{\pm}), placed at locations \vec{x}_+ and \vec{x}_- 7Mm below the surface, which are perpendicular to the polarity inversion line of the bipole, and separated by an initial distance $L_0 = 15\text{Mm}$. In this case the additional dipole field takes the functional form $\vec{B}_{q_{\pm}} = q_{\pm} \cdot (\vec{x} - \vec{x}_{\pm})/|\vec{x} - \vec{x}_{\pm}|^3$ (note that $\vec{B}_{tot} = \vec{B}_{q_+} + \vec{B}_{q_-}$ automatically satisfies both $\nabla \cdot \vec{B}_{tot} = 0$ and $\nabla \times \vec{B}_{tot} = 0$). Starting from a relaxed MHD solution at $t = t_0$ the charges are sheared at constant depth along the axis of the polarity inversion line at a linearly increasing speed to reach $v_0 = 75 \text{ km s}^{-1}$ at time $t = 5 \text{ min}$. The shearing motion then continues at this speed until $t = 30 \text{ min}$ when the motion is ended. Magnetic flux density at the boundary is preserved by modifying the charge strength to account for the change in distance $q_{\pm}(t) = q_{\pm,t=t_0} L_0^2 / |\vec{x}_+(t) - \vec{x}_-(t)|^2$, and constant depth is maintained by utilizing motion along spherical arcs at constant radii. The shear speed in the direction of the charge motion is also applied to the velocity boundary condition in the vicinity of each charge. While clearly a very idealized model, the application of this scenario leads to the requisite onset of instability and large-scale transient, as was the case for the conditions studied by Roussev et al. (2007).

5.4 Model Runs

In this section we present four simulation runs of the LC model for the 2008 March 25 EUV wave transient. The aim of conducting multiple simulations is to gain insight to the governing processes EUV waves by changing important parameters, namely average magnetosonic speed, eruption handedness, and total free energy. The varied parameters are shown in Table 5.1, all other considerations remain constant between

Run	$ q_{\pm} $ [Gauss km ²]	Handedness	\vec{B} scaling	v_{rise} [km s ⁻¹]	v_{peak} [km s ⁻¹]
A	2E+11	N/S	1	380±30	240±5
B	4E+11	N/S	1	440±30	289±8
C	2E+11	S/N	1	380±60	123±4
D	4E+11	N/S	2	780±50	322±15

Table 5.1: Summary of the four model runs and the choice of parameters for each. We also show the computed speeds of the two transverse fronts identified in the transient signal (described below).

the runs. For each run, a quasi steady-state coronal solution is first achieved by integrating the model in local time stepping mode (described in Cohen et al. (2008)), which amounts explicitly integrating each solution block, 64 cell volumes in this case, at its minimum timescale (a local quantity) from the initial condition for 8×10^4 iterations. At this point the eruption mechanism is applied, setting $t_0 = 18:40:00$ UT, and each run is advanced explicitly at the minimum global timescale until $t = 20:40:00$ UT physical time is reached.

Run A - (Baseline Run) With the first run we establish a baseline simulation for the event. In Figure 5.6 we show a running ratio time-series of the first 40 min of the synthesized images for run A from the STEREO-A viewpoint. As in the observations, a bright expanding front is seen clearly off of the limb in from the STEREO-A perspective, as well as a similar anti-correlation of the sign of the flux ratio between the lowest temperature response filter (171Å) and higher temperature response filters (195Å, 284Å, Ti-Poly), suggesting similar compression and thermodynamic mechanisms. Before proceeding we summarize the main discrepancies between the model and observations: a) the positive enhancement is most pronounced in the higher temperature bands (284Å and Ti-Poly) and shows less enhancement in the 195Å band compared to typical EUV wave observations, suggesting that the initial

quiet sun temperature at $r = 1.1 R_{\odot}$ is likely slightly too high. b) the width of the front observed off the limb by STEREO-A is less coherent (about a factor of 2) in the simulation. This is likely due both to finite resolution effects as well as the inability to produce arbitrarily fast reconnection and energy release with our eruption mechanism. And c) the imposed eruption mechanism, while producing a strong transient does not produce a fully formed erupting flux rope and strong core EUV dimming signal above the eruption site, as a result the ejected mass is significantly less than that calculated by Aschwanden (2009). This directs our focus to the feature best represented in the simulations: the expanding front of the EUV transient, which is the wave-like component identified by Patsourakos et al. (2010a). Despite these shortcomings, we propose that the ability of such a relatively simple model to capture the basic EUV properties of the expanding front represents a significant development.

Dissecting the Transient signal All simulations presented here show similar qualitative features to those described for Run A, namely a bright expanding rim showing clear temperature and density enhancements, but they differ in fundamental ways when studied in detail. As a concise and robust method of comparison, we turn to examining the transverse properties of the transient with time-distance limb diagrams (Section 5.2.2). In Figure 5.7 we show time-distance limb diagrams for an $r = 1.10 R_{\odot}$ arc based on synthetic images for the three EUVI filters (171Å, 195Å, 284Å), the XRT T-Poly filter, and emission measure all extracted at the STEREO-A location. Looking at the EM diagrams (rightmost column) all runs show a well defined density front propagating away from the eruption site in both directions, followed by both a flattening and low amplitude reversal of the signal as the front encounters the coronal hole regions (the gradient in magnetosonic sound speed is large at this interface). The anti-correlation between the 171Å filter and the others is best

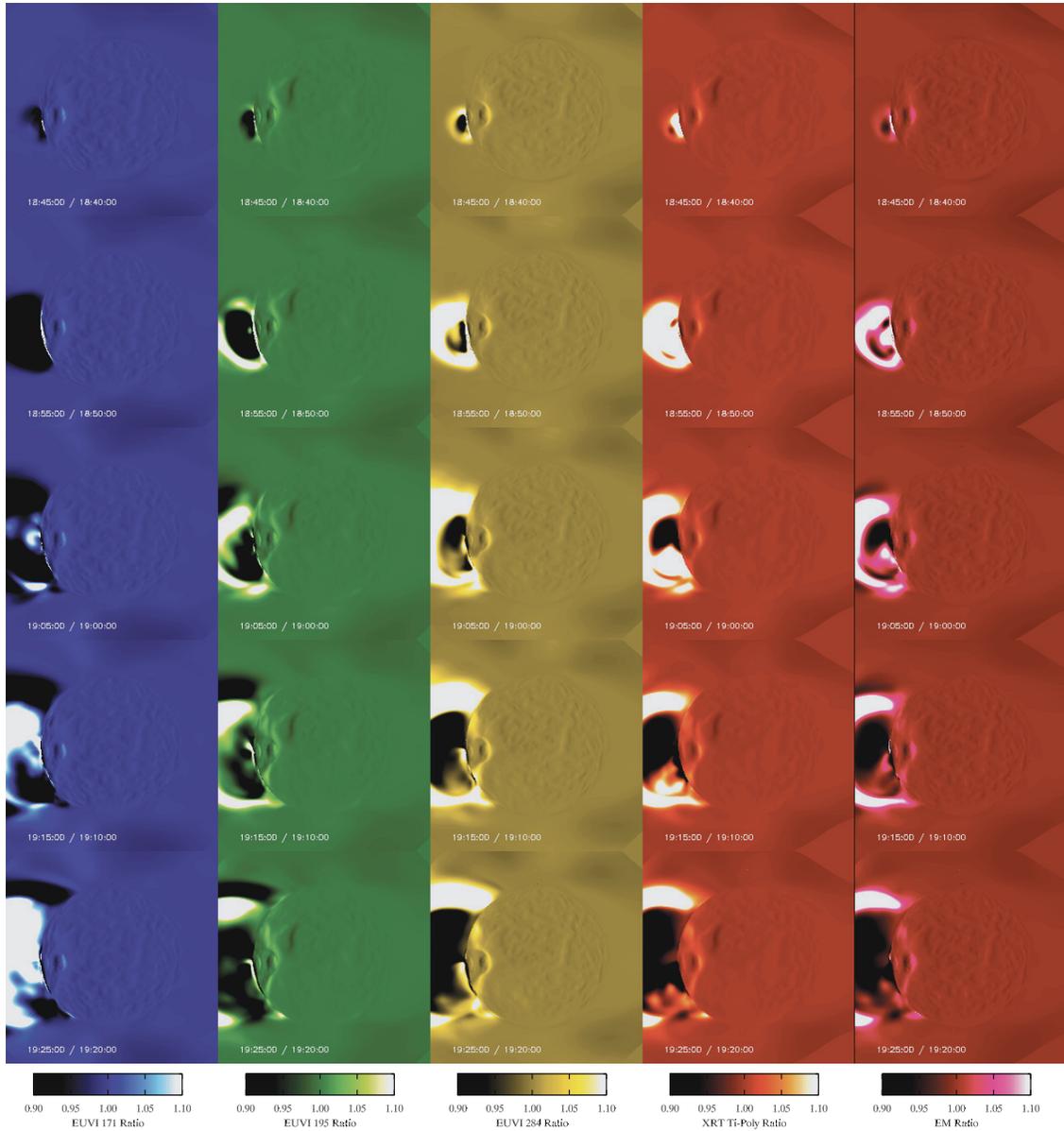


Figure 5.6: Five minute running ratio images showing the evolution of the EUV wave transient for Run A shown at ten minute intervals. The columns from left to right are: EUVI 171Å, 195Å, 284Å filters, XRT Ti-Poly filter, and integrated emission measure.

seen comparing the 171Å diagrams to the Ti-Poly diagrams, again suggestive of an increased temperature within the transient. However, in the case of the simulations, the 195Å also shows this anti-correlation (to a lesser extent). Here we note that this anti-correlation signal is somewhat sensitive to both the initial plasma temperature and perturbation amplitude, as the slope of $R_i(n_e, T_e)$ for the 195Å filter reverses around $T_e \sim 1.4$ MK. This implies that either the initial temperature of the coronal plasma at this radii is too high as compared to observations (most likely), or that the temperature perturbation has a higher amplitude than in the actual observations. Comparing the Ti-Poly diagrams to the EM diagrams also give a means of separating the correlation of temperature to density enhancement, which are typically co-spatial, but not entirely (e.g. the leading edge of the signal of Run D).

To quantify a relative comparison of the model runs to one another, we focus in detail on the structure of the northward propagating transient as identified in the time-distance limb diagrams. Choosing a position s along the $r = 1.10 R_\odot$ arc used by the time-distance diagrams gives a flux ratio as a function of time $f_s(t)$, which we show for each filter for two locations along the time-distance arc ($s_1 = 0.18$ and $s_2 = 0.70 R_\odot$) for each run in Figure 5.8. Each trace of $f_s(t)$ exhibits an initial rise (fall in 171Å) as the transient first arrives followed by a clear temperature and emission measure maximum. However the shape of each front is modulated as it evolves in space as well as from run to run. We separate the transient signal in terms of two components: a) a leading or “rise front” that identifies the time for a fixed location along the arc that the transient first appears, and b) a compression peak that identifies the time of the maximum density perturbation for fixed location. Calculating the rise and compression times for multiple locations on the arc gives a means of measuring the relative speed of each component and contrasting their change from run to run.

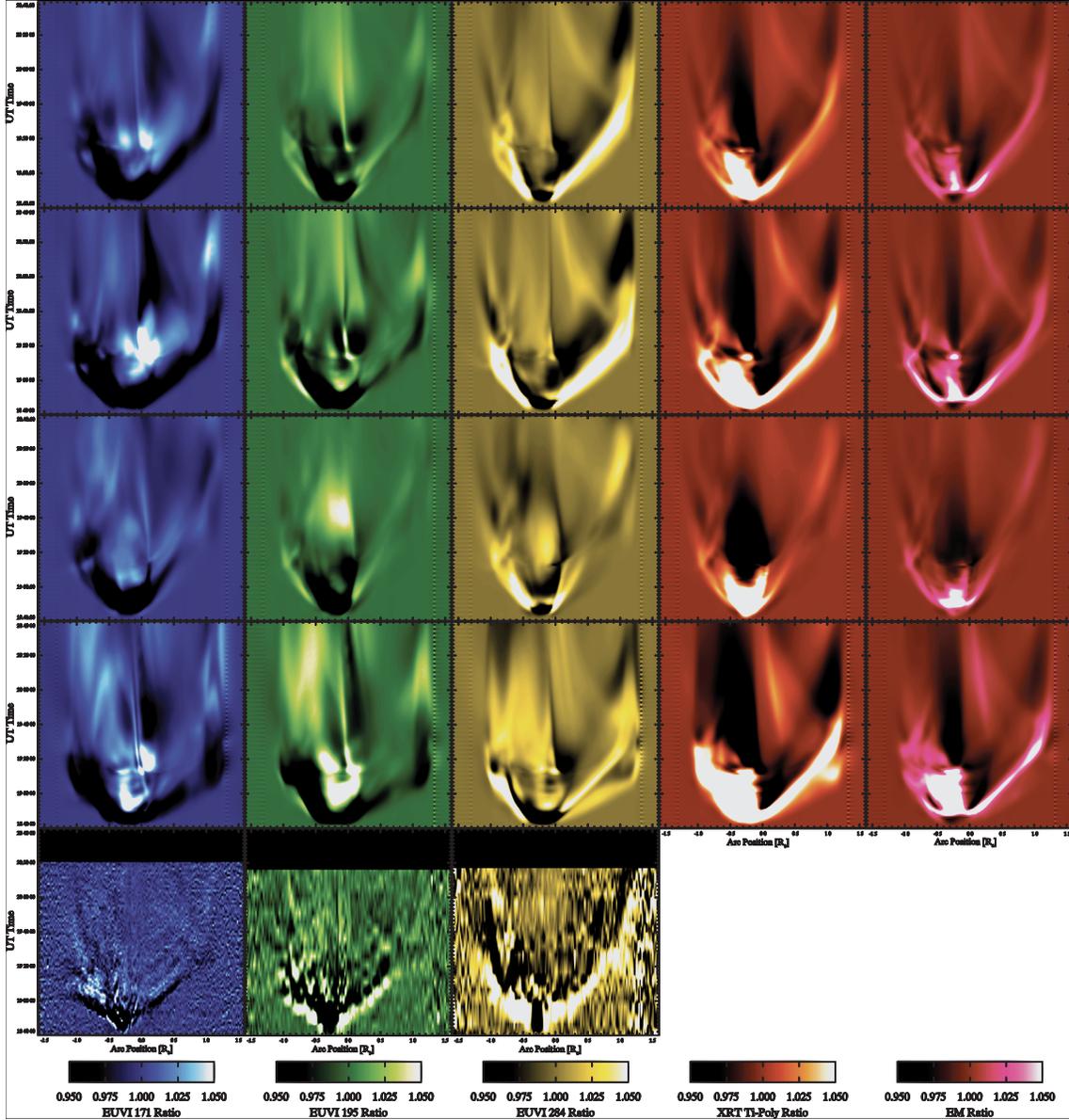


Figure 5.7: Time distance diagrams at $r = 1.1 R_{\odot}$ of the East limb for all four model runs and observations. From top to bottom we show Run A (baseline run), Run B (2x free energy), Run C (opposite handedness), Run D (2x ambient field), and EUVI-A observations. Shown in columns from left to right are: EUVI 171Å, 195Å, 284Å filters, XRT Ti-Poly filter, and integrated emission measure. The XRT diagram provides a diagnostic of the high temperature shifts during the event, while the emission measure gives purely the line-of-sight density dependence. To maximize fidelity, all synthesized time-distance diagrams are at a 2.5 minute cadence (the observation diagram cadences are described in the caption of Figure 5.2).

The timing of the rise front is determined by setting a normalized threshold value, a , and determining the time t_{rise} for which $a = abs(f_s(t))/max(abs(f_s(t)))$. The timing of the compression peak is simply the time t_{peak} for which $f_s(t) = max(f_s(t))$ for the emission measure (density only) filter. The velocity of the front between two points, s_1 and s_2 , is then readily determined as $v_{front} = (s_2 - s_1)/(t_2 - t_1)$, where t_1 and t_2 are determined from the methods listed above. Estimates of the inherent variation are determined by repeating the process for the nine pairs of points between $[s_1 - \Delta s, s_1, s_1 + \Delta s]$, and $[s_2 - \Delta s, s_2, s_2 + \Delta s]$ and calculating the average v_{front} (here $\Delta s = 0.06R_\odot$). Because the threshold method is somewhat ill-posed, we determine the average v_{rise} by repeating averaging the above process for values of $a : [0.1, 0.15, 0.20, 0.25]$ and determine our estimate of the error in the mean v_{rise} as the difference between the minimum and maximum velocities determined here. The compression location is well defined, and we calculate the error estimate as the standard deviation of the nine computed values for v_{peak} . The speed determinations for each front using locations $s_1 = 0.18$ and $s_2 = 0.70 R_\odot$ is summarized in Table 5.1.

Another feature of this diagnostic is its ready characterization of the thermodynamic response of the plasma to the transient. Looking at in detail $f_{s_1}(t)$ for Run A (top trace of Figure 5.8a) we see the transient signal is characterized by a marked decrease in 171Å flux, a rise then fall in 195Å flux, and ensuing peaks in the 284Å and Ti-Poly filters, which are co-temporal with the peak density compression. The process is then reversed as the front passes. This is entirely consistent with the travelling front smoothly enhancing the local temperature, T_e , and shifting the spectral response functions along the curve shown in Figure 5.4, a mechanism proposed by Wills-Davey & Thompson (1999). It is also worth noting that the static quiet sun heating component (Section 5.3.2) is not likely to contribute significantly to this thermodynamic phenomena because its inherent

heating timescale, $t_{heat} \sim P_e/Q_{qs}$, is greater than 30 minutes at $r = 1.1 R_\odot$ for $n_e > 5 \times 10^{-7}$ ergs cm^{-3} and $T_e > 10^6$ K.

Run B - (Eruption Strength) With our next run we choose to examine the effect that eruption strength plays in characterizing the EUV wave. To do so, we double the amount of magnetic flux involved in the shearing motion by doubling the strength of base charge to $|q_\pm| = 4 \times 10^{21}$ Gauss cm^2 . To preserve nearly identical heating with respect to Run A, we subtract the additional contribution to \vec{B} from the active region heating term (Q_{ar} in Equation 5.2). Examining the main differences between the transient signatures of Run A and B in the time-distance diagrams (Figure 5.7) it seems the dominant effect is a larger amplitude for the transient, particularly for the 284Å and Ti-Poly bandpasses. This is consistent with the fast mode wave interpretation, as an increase in energy released should naturally imply an increase in wave amplitude, although this would be similarly true for more complex modes as well. However, we also observe a slight increase in transverse speed of both the rise and peak compression fronts ($\sim 50 - 60\text{km/s}$). The slight increase in speed of both components is difficult to explain with a freely propagating fast-mode wave in the sub-shock limit, as is the case here. This increase suggests that the speed has been modulated due to the enhanced amplitude of the eruption and overpressure of the expanding plasma cavity, a phenomenon consistent with the solitary wave hypothesis of Wills-Davey et al. (2007). Of course, the relative importance of each mechanism cannot be easily determined yet in this case.

Run C -(Eruption Handedness) The second variable we examine is that of eruption handedness. As discussed in Section 5.3.3, photospheric motion of active region flux concentrations typically exhibit shearing patterns around the inversion

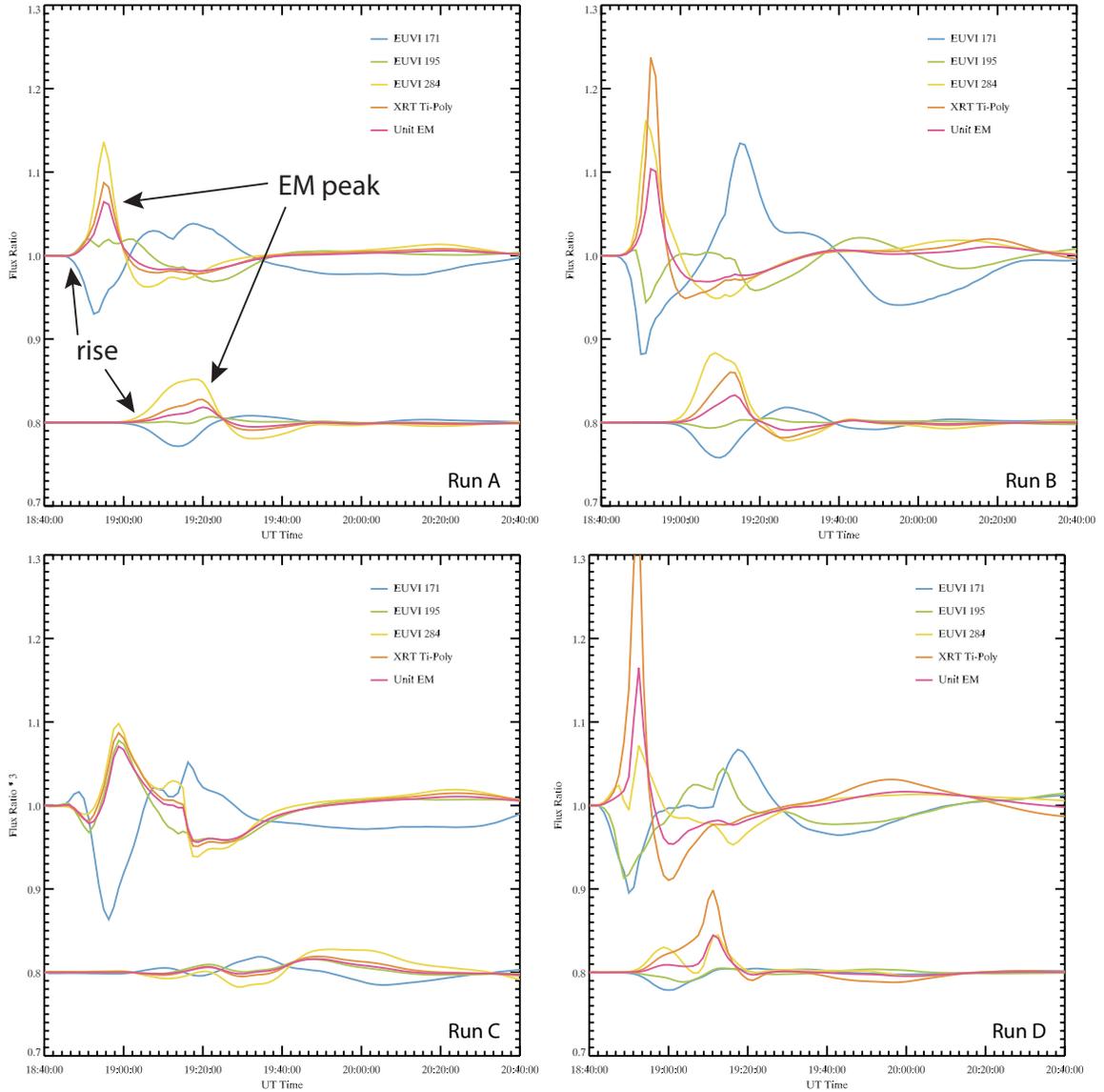


Figure 5.8: The flux ratio as a function of time for two points $s_1 = 0.18$ (upper trace) and $s_2 = 0.70 R_\odot$ (lower trace) on the arc axis of the time-distance diagrams (Figures 5.2 and 5.7) for Run A (baseline run), Run B (2x free energy), Run C (opposite handedness), Run D (2x ambient field). The traces are separated by subtracting a constant offset from the flux ratio at s_2 : $f_{s_2}(t) \rightarrow f_{s_2}(t) - 0.2$. The signal for Run C is scaled by a factor of three to emphasize the low-amplitude early rise front. The annotation for Run A illustrates what is identified in the front calculations for each run. The strong distortion of the perturbation signal in the lower trace for Run D is indicative of the bifurcation of the two fronts when the fast-magnetosonic speed is doubled.

line, a natural result of the Lorentz force on the atmosphere due to magnetic flux emergence (Manchester et al. 2004; Archontis et al. 2004). When the overlying coronal field is asymmetric, a change in sign of the shearing motion will drastically change the interaction between the two flux systems (overlying field and emerging field). In Run C, using the same relaxed configuration and heating model of Run A, we reverse the shear direction by 180° by changing the projected motion of the positive and negative charges from North/South (N/S) to South/North (S/N) respectively. As seen in Figure 5.7, this has a dramatic effect on both the strength and location of the resulting transient, most noticeably shifting the peak of the transverse emission measure signal from the northward to southward direction. Of note is the fact that the rise component of the northward transient is greatly diminished in amplitude (but not zero!), while the compression peak component remains relatively intense but travels at a markedly slower projected speed (240 km s^{-1} in Run A, 123 km s^{-1} in Run C). However, the rise front travels at a nearly identical speed to that in Run A, suggesting a similar mechanism with differing amplitudes, which is consistent with the identification of this front as the fast-mode component. The difference in speed between the respective compression peaks in Run A and Run C suggest an alteration of the speed and/or location of the global compression response of the ambient coronal field to the north, which should result naturally from a significant change in the nature of eruption brought about by reversing the shear direction.

Run D - (Ambient Magnetosonic Speed) In our final simulation we focus on the dependence of the EUV transient properties on the ambient magnetosonic speed in the corona. For this simulation, Run D, we scale $|q_{\pm}|$ and the boundary magnetic field by a factor of two (thus scaling the 3D PFSSM initial condition by the same factor), while simultaneously decreasing the \vec{B} dependence of the Q_{ar} heating component by

the same amount. After advancing the model to steady state, we achieve a similar equilibrium to that of Run A except now the magnetic field strength everywhere has increased by roughly a factor of two. Depending on the local ratio of sound speed, c_s , to Alfvén speed, v_A , (note $c_s^2/v_A^2 = \gamma\beta/2$, where β is the ratio of thermal pressure to magnetic pressure), this gives an increase of the perpendicular fast magnetosonic speed, $c_f = \sqrt{v_a^2 + c_s^2}$, of roughly a factor of two for low β regions (note that $\beta < 0.01$ for most of the corona below $r = 1.5R_\odot$, away from polarity inversion regions and current sheets), and a factor ~ 1.66 for $\beta = 1$.

The most obvious difference between Run D and Run B (which releases a comparable amount of magnetic energy due to the identical increase in charge strength) is the increase in speed of the rise component of the transient signal by nearly a factor of two (440 km s⁻¹ in Run B, 780 km s⁻¹ in Run D). Clearly this leading edge is highly dependent on the ambient magnetosonic speed, which allows for the direct identification of the “rise-front” as the fast magnetosonic wave component of the EUV wave transient. Another striking result is the fact that the peak of the compression front shows only a slight speed increase ($\sim 10\%$) relative to its Run B counterpart, and Run D now shows a clear bifurcation between the two fronts (visible in Figures 5.7 and 5.8). The lack of dependence on the fast magnetosonic speed of the trailing front suggests an alternate mechanism that is tied to the inherent details and timescales of the eruption impinging on the surrounding medium itself and *not* the ambient magnetosonic speed of the medium.

5.5 Discussion

The runs described in Section 5.4 provide an intriguing result: The peak transverse front of the EUV wave depends more on the inherent timescales of the CME itself,

rather than the ambient sound speed of the entire corona – a *key* distinction. This falls directly in line with an identification of the peak compression front as the non-linear response of the ambient coronal structure to the expansion of the eruption itself, which is in line with the ‘driven MHD-wave/plasma compression’ scenario: one of two plausible scenarios emphasized by (Attrill et al. 2009). This is further supported by the discrepancy of the compression peak speed (v_{peak}) with the rise speed (v_{rise}) for every run, where v_{rise} is consistently larger by at least 100 km s^{-1} . To show this visually, we plot time-distance diagrams for each run zoomed in on the northward propagating perturbation with overplotted derived front speed ranges for the EUVI-A 284Å filter (creffig:ch5:runs-slope-diagram-284) and column emission measure (Figure 5.10).

Focusing now on the 3D simulation data directly, we show the evolution of the front and ambient magnetic topology on an $r = 1.10 R_{\odot}$ surface and plane normal to the STEREO-A viewing position for runs A and D in Figure 5.11. The running ratio contours of n_e show a hemispherical perturbation ($\pm \sim 5 - 10\%$) propagate away from the erupting active region, forming a coherent outwardly propagating front. The separation of the fast-mode front from the coherent front formed by the eruption becomes quite evident comparing the initial 30 minutes (first 2 frames) of Run A to Run D. The increase in magnetic free-energy released (due to the doubling of $|\vec{B}|$ everywhere) has also modulated the outward speed of the compression front approximately 20-50% but is this not the near factor of two as would be expected by the increase in magnetosonic speed. This provides further evidence that the bulk of the perturbation signal is a result of the compression induced by the eruption processes and propagating plasma cavity, which will have a non-linear relationship to the overall characteristic sound speeds of the corona.

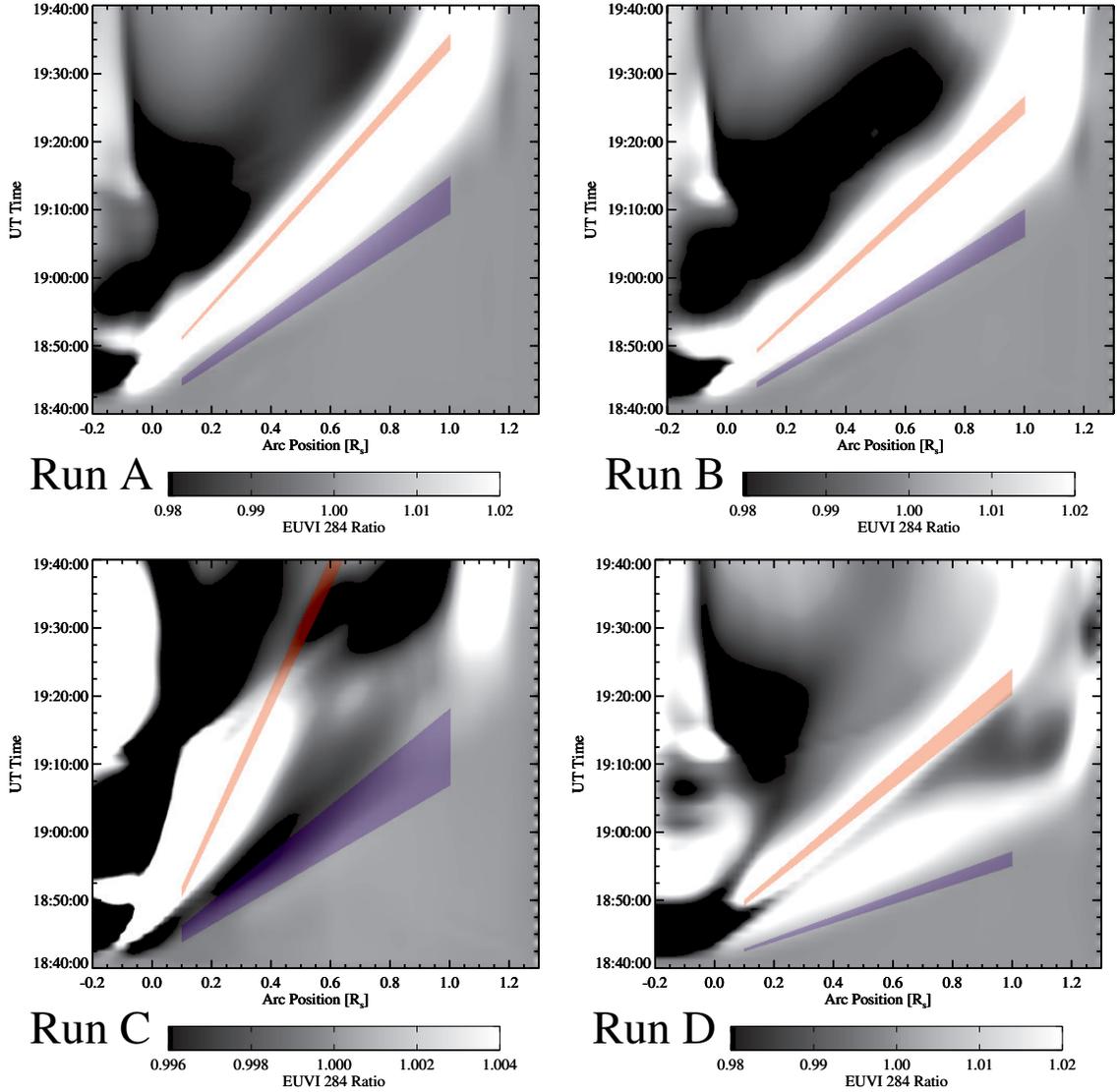


Figure 5.9: Time-distance diagrams of the EUV transient for all four runs zoomed in on the northward front of the EUV perturbation for the synthesized EUVI-A 284Å filter. The transparent polygons represent the derived speed limits of the rise front (blue) and the compression peak (red) diagnostics for each run (see Table 5.1 for the speed ranges). Similar to Figure 5.3, the slope of the polygon is defined by the bounding speed range while the width in time is defined by the time interval needed to travel at these speeds to $s = 0.1$ from $s = -0.15 R_{\odot}$. The left position (intersection) of the polygon on the diagram is simply the calculated $t_{rise}(t_{peak})$ for $s = 0.1 R_{\odot}$. The contrast is enhanced to show the location at which the perturbation is first seen, which is the feature identified by the rise calculation. The separation of the two fronts for run D is also clearly visible.

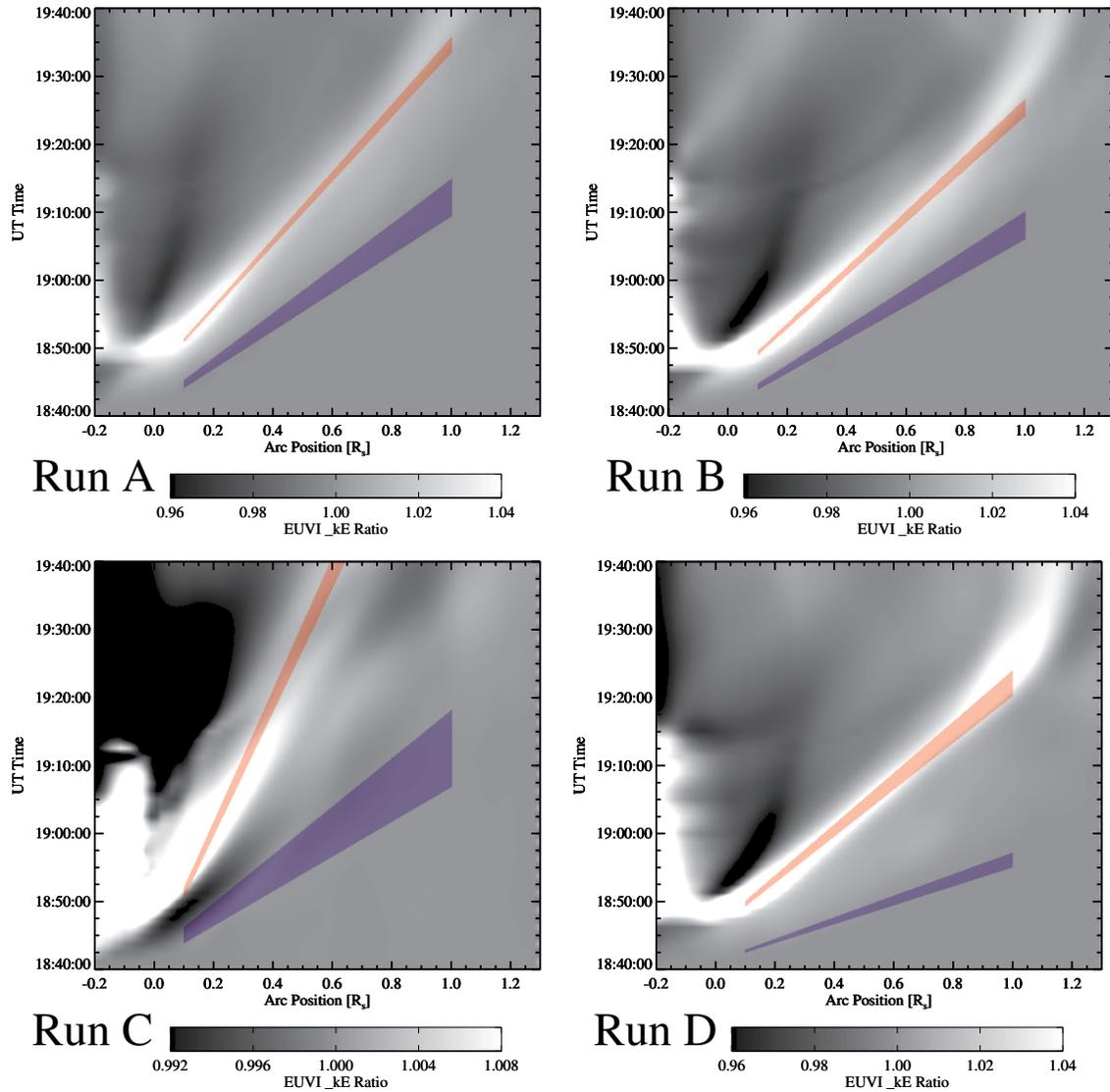


Figure 5.10: Time-distance diagrams of the EUV transient for all four runs zoomed in on the northward front of the EUV perturbation for the integrated column emission measure along the limb arc. The transparent polygons are identical to those in Figure 5.9 and represent the derived speed limits of the rise front (blue) and the compression peak (red) diagnostics for each run. This is intended to visually highlight the fact that the peak of the enhancement is seen to propagate at a significantly lower speed (slope) than the first instance of the perturbation as derived from the EUV filters, which is at a significantly lowered amplitude when examining the column emission measure (density only).

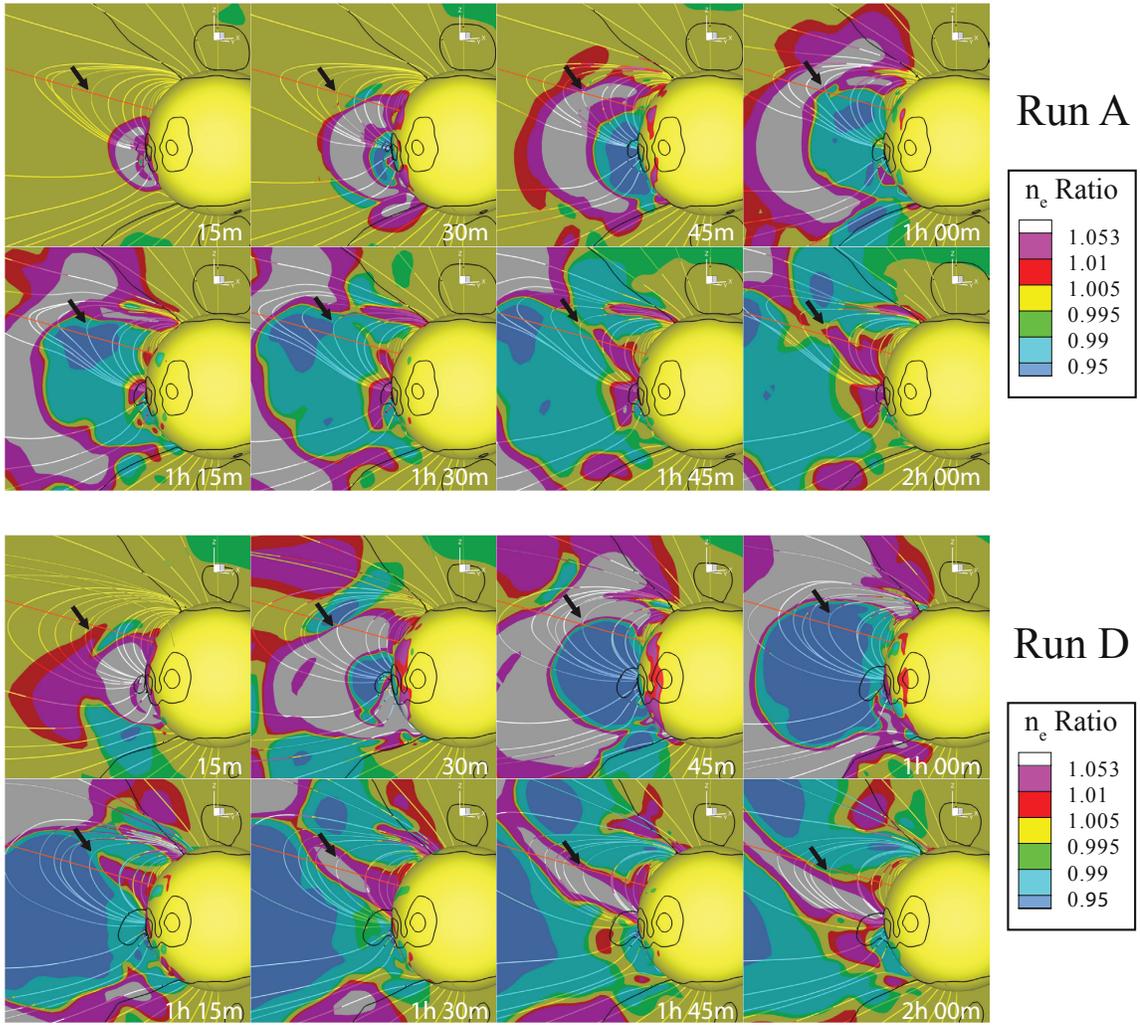


Figure 5.11: Visualization of the evolution and interaction of the transient with the ambient corona for the baseline run (Run A, Top) and the run with magnetic field scaled by a factor of two (Run D, Bottom) at 15 min intervals for the first 2 hours of the event. Coloring indicates 5 minute running ratios of the electron density, n_e , on an $r = 1.10 R_\odot$ surface and the plane normal to the STEREO-A viewing vector. 3D streamtraces of \vec{B} are drawn from points intersecting this plane and the spherical surface at near equal latitude intervals and the same points are used in each frame. These are chosen to emphasize the interaction of the expanding CME front and compression of the northward streamer region. This is highlighted by comparing the streamlines from frame to frame to the fixed orange line drawn as a reference point. The black arrow in each frame is hand drawn to point to the apex of a selected streamtrace ($|B_r| \sim 0$) and also illustrates the shift in this position as a function of time. The black lines show contours of $c_f = [1000, 3000]$ km s $^{-1}$ for Run A and $c_f = [2000, 6000]$ km s $^{-1}$ for Run D, which serve to outline the active regions and latitudinal extent of the Polar Coronal Holes.

Additional evidence for an organized transverse compression front comes from examining the effect of the eruption on the northward streamer region, visualized with magnetic streamlines in Figure 5.11. The orange line, which remains constant in each frame, represents the axis of the streamer region intersecting this plane for the pre-eruption state of Run A (i.e. $B_r \equiv \vec{B} \cdot \hat{x} \sim 0$). As the peak amplitude of the front passes around $t \sim 45 - 75$ min, the axis of the streamer region shifts northward collectively, and becomes noticeably offset from its equilibrium position (highlighted by the arrows). As the eruption front moves outward, and subsequently exits this region of the corona ($t > 75$ min), the axis of the streamer region is seen returning to its original position, co-temporal with the density front now traveling in the opposite, southward direction (most noticeable in Run D due to the increased eruption speed and amplitude). This implies that the observed EUV wave signal is most closely related to the plasma-compression of the streamer region (surrounding field) as it is perturbed from an equilibrium state.

It is also worth noting that in these simulations we are probing a regime where the transverse speed of the compression front in the quiet sun is below the typical fast magnetosonic speed. This is illustrated by showing the maximum (perpendicular) value of the fast magnetosonic speed, $c_f^{max} = \sqrt{V_a^2 + c_s^2}$, on the same plane shown in Figure 5.11 for the pre-eruption state of Run A in Figure 5.12. The fact that $c_f^{max} > 350 \text{ km s}^{-1}$ along the entire $r = 1.1 R_\odot$ arc northward of the eruption region indicates that the transverse compression peak ($\sim 240 \text{ km s}^{-1}$) is indeed traveling well below the fast magnetosonic speed (note that c_f^{max} effectively doubles everywhere for Run D so this statement is still valid). If the conditions were reversed and the ambient Alfvén speed were significantly lower than the transverse evolution of the event the formation and propagation of shocks would indeed modify the results (i.e. the case in the rising flux-rope experiment of Wang et al. (2009) or the scenario outlined

in Veronig et al. (2010)), which we leave to a further investigation. In our case, using a smoothed MDI magnetogram for the PFSSM initial condition and magnetic boundary conditions in the model is likely to *underestimate* the average magnetic field strength and thus fast magnetosonic speed in the quiet corona. This, combined with the realistic thermodynamic conditions afforded by the LC model (supported by the observation comparison shown in Figure 5.5), suggests that these sub-shock conditions are a plausible limit for the true quiet corona.

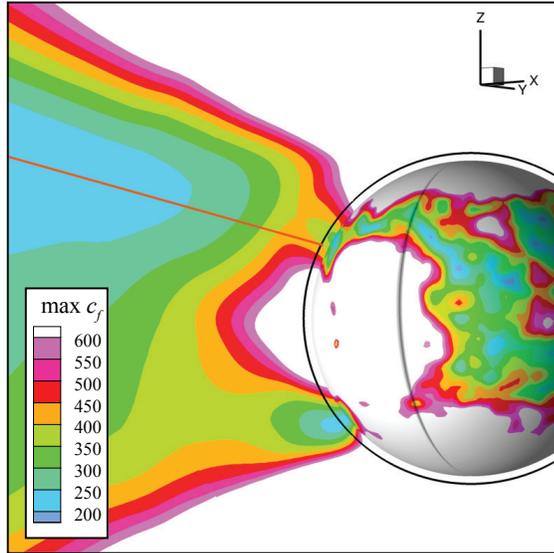


Figure 5.12: Color contours of the maximum (perpendicular) fast magnetosonic speed, $c_f^{max} = \sqrt{V_a^2 + c_s^2}$, in units of km s^{-1} for the pre-eruption configuration of Run A showing the same plane as in Figure 5.11 and an iso-surface of $r = 1.05 R_{\odot}$ (note $c_f^{max} \sim v_a$ for $\beta \ll 1$). The black line indicates $r = 1.1 R_{\odot}$ (the same distance of the time-distance diagrams) and the fixed orange line from Figure 5.11 is shown. Note that $c_f^{max} > 350 \text{ km s}^{-1}$ along the entire $r = 1.1 R_{\odot}$ arc northward of the eruption region while the derived speed of the transverse compression peak for Run A is $\sim 240 \text{ km s}^{-1}$. The saturation value of 600 km s^{-1} is chosen to illustrate the topological regions where c_f is large.

5.6 Conclusions

Using a global MHD model of the low corona as an experimental laboratory, we have studied the effect of three critical parameters on the subsequent evolution of the EUV transient, namely the eruption strength, eruption handedness, and ambient sound speed of the corona. Additionally, by modeling the realistic conditions of an observed event (instead of an idealized or axis-symmetric case) we have a means of interpreting the features and discrepancies of the results in direct context with observed characteristics of EUV waves, while simultaneously including the same form of observational bias. While it is obvious that these three variables should all play a role in determining the EUV wave characteristics, the separation of all three in a cohesive manner allows for the following interpretations:

- We can decompose the EUV wave transient into two parts: (i) a rise component travelling at the fast mode speed, and (ii) a separate (but often nearly overlapping) compression front of the surrounding medium brought about by the expansion of the erupting structures into the corona, which constitutes the diffuse peak of an EUV wave transient. This interpretation, one which identifies the EUV signal as a driven non-linear compressional wave, relaxes the requirement that this diffuse peak travels at the fast magnetosonic speed. This a very similar distinction to those made by Chen et al. (2005); Cohen et al. (2009), and in this case we do not require a freely propagating fast-mode component traveling at the fast magnetosonic speed to explain the coherent characteristics of the observed transient front (though it must surely exist at some amplitude).
- The amount of energy released during the eruption has a strong enhancement effect on the amplitude of the transient, but a lesser effect on the overall speed

(which should be related to the non-linear scaling of the eruption speed with free energy).

- Altering the eruption handedness strongly dictates the shape and speed of the peak compression front. However, the fast-mode front retains a similar speed and location (though with considerably less amplitude) again suggesting that the two components are independent.
- Through direct synthesis of observations we are able to re-create and examine the contrasting multi-filter dependence of the EUV wave transient. We find that the anti-correlation of the perturbation amplitude between 171Å (lessened emission) and the 195Å and 284Å filters (enhanced emission) can be well represented by temperature enhancement inside a propagating compression front, which is also diffusive due to the electron heat conduction term. We do not find that reconnection and/or permanent mass depletion are necessary components for describing this phenomena, though it should certainly modulate the signal where and when it does occur.
- Increasing the ambient Alfvén speed in the corona caused a clear separation of the two identified components, with the dominant transient component travelling below the fast-mode speed. This is a direct test of the fast-magnetosonic wave hypothesis and, in these experiments, we find that freely propagating fast-mode wave is not significantly contributing to the large-scale transverse signal of an ‘EUV wave’. This places emphasis on the need for any unified interpretation of the EUV wave picture to also account for the dynamic response of the global corona to the triggering eruption.

Of course with the commissioning phase of the Atmospheric Imaging Assembly (AIA) (Rochus et al. 2004) onboard the Solar Dynamics observatory nearing completion, we are poised to explore EUV waves with revolutionary observational advances in both time and temperature cadence. As such it is important to strive to develop models that are able to both capture observations and interpret the underlying mechanisms that compose them.

Chapter 6

Case Study 2: 2010 June 13 EUV Wave

Abstract

In this chapter we present a comprehensive observation and modeling analysis of the 2010 June 13 Extreme Ultraviolet (EUV) wave observed by the Atmospheric Imaging Assembly (AIA) aboard the Solar Dynamics Observatory (SDO). Due to the extreme advances in cadence, resolution, and bandpass coverage in the EUV regime, the AIA instrument offers an unprecedented ability to observe the dynamics of large scale coronal wave-like transients known as EUV waves. However, the complexity of the corona, coupled with line-of-sight (LOS) projection of structures, can often make the underlying nature of EUV waves difficult to interpret directly. To provide a physical analysis and further compliment observational insight, we conduct a 3D, time-dependent thermodynamic MHD simulation of the eruption and associated EUV wave using the Lower Corona (LC) component of the Space Weather Modeling Framework (SWMF). A key feature of this model is the ability to synthesize the multi-filter observations of the SDO/AIA instrument directly from model data, which allows for direct interpretation of the evolution observed by AIA with full knowledge of the evolving 3D magnetic and thermodynamic structures in the simulations. We focus

on two main aspects: (a) the interpretation of the stark thermodynamic signatures in the multi-filter AIA data within the propagating EUV wave front. And (b) an in depth analysis of the simulation results and their implication with respect to EUV wave theories. Multiple aspects, including the relative phases of perturbed variables, suggest that the outer, propagating component of the perturbation exhibits the behavior of a fast-mode wave. We also find that this component becomes decoupled from the evolving structures associated with the Coronal Mass Ejection that are also visible.

6.1 Introduction

In the previous study, we used multiple model runs in an experimental approach to examine the effect of various mechanisms on the nature of the EUV wave perturbation. This was quite successful for probing the relative strength of mechanisms for realistic conditions that we observe in the corona. The qualitative nature of the wave front was reproduced, in particular the thermodynamic behavior of the front (Figures 5.7 and 5.8), but due to observational limitations (lack of high cadence images in every bandpass, sub-optimal signal to noise off of the limb) it was difficult to make direct one-to-one comparisons of the simulation to model data. Ideally one would wish to compare the detailed, multi-filter flux evolution of the EUV wave predicted by the LC model directly to observations in an unbiased manner. Fortunately this wish was granted with the launch of the NASA Solar Dynamics Observatory (SDO) in February 2010.

An ambitious and technologically advanced satellite, the overarching mission of SDO is to capture a complete dynamical picture of the solar atmosphere by continuously monitoring the sun and solar magnetic field at high temporal resolution,

high spatial resolution, and high spectral resolution, with each of its three keystone instruments accomplishing pieces of this task. Of particular interest to this project is the Atmospheric Imaging Assembly (AIA) (Lemen et al. 2011) onboard SDO, an EUV imager. AIA consists of a set of four identical imaging telescopes optimized for continuous high resolution imaging at primarily EUV wavelengths. With 4096×4096 pixel detectors and a synoptic field of view out to $\sim 1.3 R_{\odot}$, AIA images the entire solar corona at an unprecedented (for the EUV regime) 0.6 arcsecond resolution. A massive improvement in its own right, the most transformative feature of AIA lies in its imaging cadence. The fastest cadence of the STEREO-EUVI instruments is typically 150-210 seconds in one or two filters depending on the specific observing program, AIA on the other hand images *all eight of its standard filters every 12 seconds!* This provides not only over an order of magnitude improvement in temporal resolution, but because all filters are continuously imaged, a tremendous amount of simultaneous thermodynamical information is gained. A sense for the unique capability of AIA is gained by comparing it to the SOHO/EIT and STEREO/EUVI instruments in Table 6.1. Comparing the three parameters that directly affect the total amount of observational data returned: the number of pixels, the number of filter-bands, and the overall cadence, we see that the AIA instrument returns a full two orders of magnitude more imaging data than either of the STEREO/EUVI instruments and a full three orders of magnitude more than SOHO/EIT. It is our goal in this work to take advantage of the new observational capabilities offered by the SDO/AIA instrument and attempt to unlock rich scientific potential they represent. Using the same coupled observation and modeling analysis approach taken in Chapters 4 and 5 we study AIA observations of the recent 2010 June 13 EUV wave event, observations that offer a tremendous amount of information on the dynamic evolution and thermodynamic state of the plasma within the EUV wave. In doing so

	AIA (2010)	EUVI-A&B (2006)	EIT (1996)
Pixels	4096×4096	2048×2048	1024×1024
Filter Bands	8	4	4
Max Cadence	10 s	150 s	600 s
Less relative to AIA	$1 \times 1 \times 1$	$4 \times 2 \times 15 = 120$	$16 \times 2 \times 60 = 1920$
Daily Data Size	~ 1 TB	~ 9 GB ¹	~ 250 MB ¹

¹changes with observing program, values represent an upper limit.

Table 6.1: Table showing the imaging capability and relative daily data amount for the three main EUV imaging instruments in space (along with launch date). In total AIA provides a full three orders of magnitude improvement over what was available a decade and a half ago. Although this does not necessarily guarantee results, the most fundamental improvement comes in terms of image cadence and filter coverage, which is more than an order of magnitude improved over the EUVI-A&B instruments launched in 2006.

we conduct a 3D thermodynamic MHD simulation of the EUV wave event, one that accurately characterizes the both the pre-event thermodynamic and magnetic state of the global corona and dynamic evolution of the EUV wave.

In Section 6.2 we briefly describe the observations of the 2010 June 13 EUV wave transient, a prototypical event observed by SDO/AIA. In Section 6.3 we describe the 3D MHD model and methods used in this work. Sections 6.4 and 6.5 describe the simulation of the event and provide a discussion of the results.

6.2 Observations of the 2010 June 13 EUV Wave Event

The primary focus of this work is the EUV wave transient that occurred on 2010 June 13 around 05:35 UT, and featured a flare and CME centered above on NOAA Active Region 11079. From Earth’s perspective AR 11079 had just rotated off of the solar disk, making this event appear as an extended perturbation off of the West limb. At this time the AIA instrument had recently finished its commissioning phase and

begun its synoptic science program featuring 0.6 arcsecond resolution images of the full sun out to $1.3 R_{\odot}$ at 7 EUV wavelengths all at a 12 second cadence. Being so close to the beginning of the AIA science program, this event was the first relatively high amplitude EUV wave observed, due primarily to the relatively fast impulsive CME, which produced a type II radio burst (associated with shocks). The associated CME kinematics were analyzed by Patsourakos et al. (2010b) and observational details of the shock conditions responsible for the type II radio burst are studied in Ma et al. (2011); Kozarev et al. (2011).

AIA images of the CME and EUV wave for the three highest signal-to-noise (S/N) filters (171, 193, and 211Å) at four minute intervals are shown in 6.1. The images are created using the running flux ratio method (Section 5.2.1), which divides the flux at given time by the flux at a previous time (24 second intervals in this case). These filters have similar response characteristics to the EIT and EUVI 171, 195, and 284Å channels (discussed in Section 6.3.1), and the basic thermodynamic features observed are similar to the 2008 March 25 event (Figure 5.1, negative perturbation in the outer front for 171, stronger positive perturbation in the higher channels). However, because of the synchronized, high cadence multi-filter observing program, the thermodynamic evolution of the event in *all* filters can be examined much more clearly. Furthermore, the high ratio cadence (24 seconds) allows for a much sharper view of the EUV wave front (outer component). This is critical, because early on a clear separation between the EUV wave and a trailing enhancement is observed (very clear in the 2nd and 3rd frames). The inner component is identified as the expanding bubble created by the erupting CME by Patsourakos et al. (2010b) and it initially appears as a positive enhancement in all three filters. This is indicative of a strong density enhancement (the CME is piling up material in front of it), which would be expected to increase emission in all filters (as opposed a temperature dominated

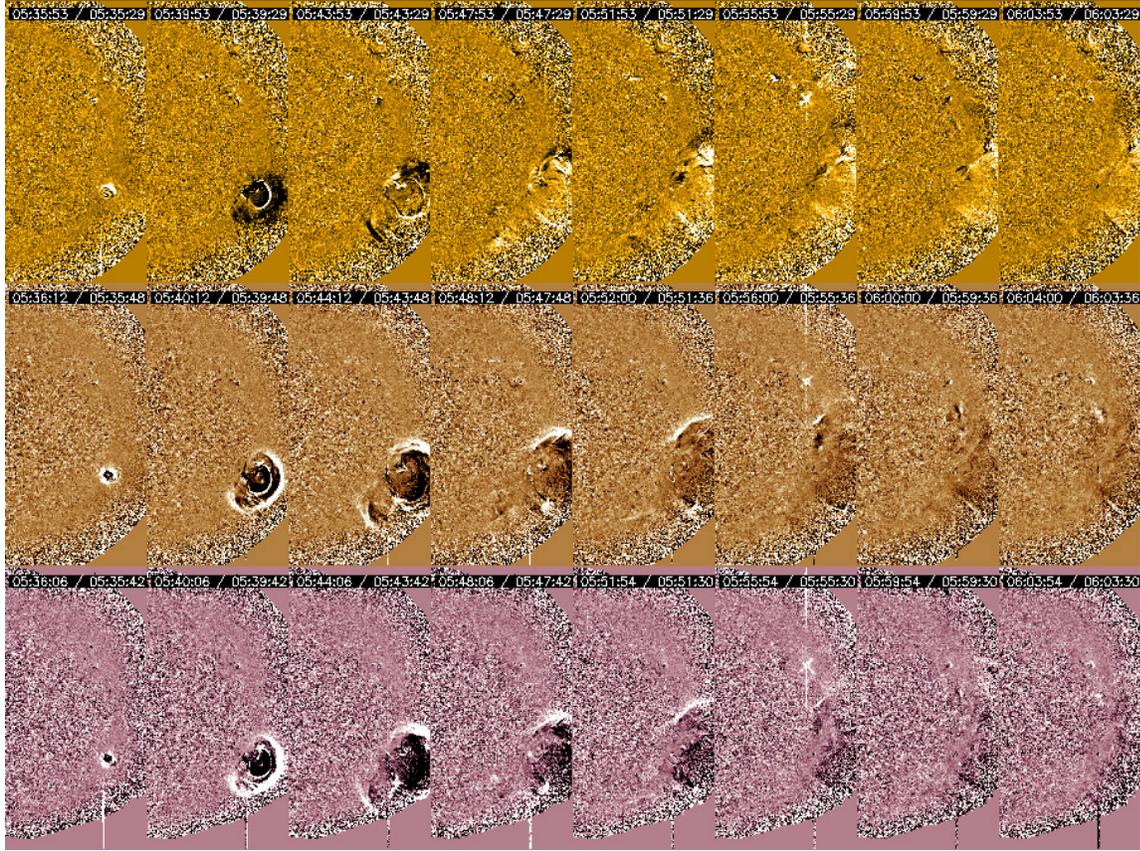


Figure 6.1: Twenty four second running ratio AIA images of the 2010 June 13 EUV wave event, shown at four minute intervals. Shown from top to bottom are the Fe IX 171Å, Fe XII 193Å, and Fe XIV 211Å filter channels respectively. Analogous to the 2008 March 25 event (Chapter 5) this event is characterized by a strong perturbation expanding outward in all directions that is positive in the 193 and 211Å bands and negative in the cooler 171Å band. The high ratio cadence (24 seconds) allows for a much sharper view of the EUV wave front (outer component) and early on a clear separation between the EUV wave and trailing enhancement is observed (2nd and 3rd frames). The inner component is identified as the CME by Patsourakos et al. (2010b). The minimum and maximum color range for the ratio shown is $1 \pm 2\%$. *Note:* the different false coloring convention reflects the colors chosen by the AIA instrument team.

change, which will change the relative filter contributions). The lingering effects of the CME passage remain in a moderate latitudinal width long after the EUV wave has passed below the detection limit (particularly visible in the later frames of the 171Å and 193Å images).

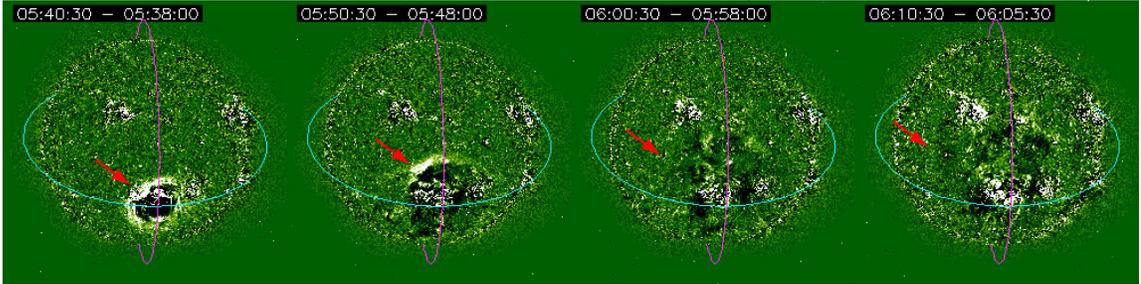


Figure 6.2: 2.5 minute running difference EUVI-A observations of the 2010 June 13 EUV wave shown at 10 minute intervals. From this STEREO-A perspective the eastward (red arrows) and westward propagation becomes clearly visible, features which cannot be captured from the limb perspective of AIA. For a scale perspective, the pink arc in each image represents a meridional arc of $1.2R_{\odot}$ centered above the eruption region, while the blue arc is the perpendicular great circle.

At this time, we were also fortunate that the separation of the STEREO spacecrafts (Kaiser et al. 2008) had placed them at near right angles to the orbit of Earth. This meant that the EUV wave was observed almost directly on disk center by the EUVI instrument (Wuelser et al. 2004) onboard the STEREO Ahead (STEREO-A) spacecraft, providing a completely complementary perspective and LOS projection of the EUV wave. At this time the synoptic observing program for EUVI-A had only the 195Å channel observing at a high cadence (2.5 minutes), but the general evolution and extent of the event was captured. EUVI-A 195Å images of the the event is shown in Figure 6.2, this time showing the running flux *difference* which better captures the EUV wave features when projected onto the solar disk (for a more in-depth discussion on the relative advantages/uses of flux differencing or flux ratios and running and base methods, please refer to Section 5.2.1). The images are processed

as 2.5 minute running difference images and linearly scaled with $\pm 5 \text{ DN/s min/max}$ (the last image shows a 5 minute difference due to a data gap). From this perspective the event exhibits the typical EUV wave characteristics (isotropic expansion, speed ranging from 250–350 km/s), particularly for the eastward (red arrows) and westward propagation, which cannot be captured from the limb perspective of AIA. The northern component remains clearly visible until it encounters an active region, at which point the signal becomes obscured (more details in 6.4).

6.2.1 AIA image reduction methods

Although AIA images are conveniently available only as already reduced Level 1 science products (Lemen et al. 2011), to extract the best signal for the EUV wave, the data is further processed for the following reasons: First, because EUV emission falls off sharply as a function distance from the solar limb ($\text{Flux} \propto n_e^2$) the amount of photon noise increases the further one looks off of the limb for a fixed image exposure. Second, the photon S/N off of the limb is further reduced due to data compression algorithms that are applied onboard before each image is transmitted to the dedicated SDO ground-station. This process typically reduces the file-size by a factor of 7-10 (absolutely required for the experiment to function) and is designed to prioritize high S/N features on the solar disk. This then presents a difficulty when attempting to extract the running flux evolution (already a derivative) of a signal that is typically no more than 5% over the background as the EUV wave propagates away from the eruption region. Fortunately, for the case of studying EUV waves, which are naturally large-scale, wide perturbations, the extreme high-resolution of the AIA telescopes can be harnessed to increase signal to noise by re-binning the 4096×4096 images down to a 512×512 . The resulting binned image represents 64 pixel averages and increases the

per-pixel S/N by a factor of 8. Additionally because the full 12 second cadence is not needed in the analysis, every other image is added together, further increasing the S/N ratio. Additionally for our quantitative flux plots in 6.4, we perform Gaussian convolution of each binned AIA image with a half width of $\sigma = 0.03 R_{\odot}$ (~ 6 pixels in the re-binned images) before calculating the ratios in an attempt to draw out the the large-scale properties of the event and further smooth out the effects of unrelated local variations and photon noise off of the limb.

6.3 Numerical Model

In order to realistically simulate the conditions for the 2010 June 13 event we require an MHD model that accurately captures the thermodynamic state of the low-corona. To this end we employ the Lower Corona (LC) component of the Space Weather Modeling Framework (SWMF) Tóth et al. (2005). Details of the development and implementation of the LC component, which includes considerations relevant to resolving the thermodynamics of the low corona and transition region (e.g. radiative loss, field-aligned electron heat conduction, and empirical coronal heating in the energy equation), can be found in Downs et al. (2010) (Chapter 4). A first application of this model to the study of EUV waves can be found in Downs et al. (2011) (Chapter 5).

As in our previous work we use a spherical (r, ϕ, θ) AMR grid that is non-uniform in the radial direction. The r -coordinate is implemented to possess high resolution, transition region scales ($\min \Delta r < 210\text{km}$) at the $r = 1R_{\odot}$ boundary of the model, and smoothly transition to logarithmic behavior at large radii. A minimum refinement of $64 \times 128 \times 64$ is applied to the entire domain with an additional factor of two refinement below $r = 1.7R_{\odot}$ for sub-polar co-latitudes ($-65^{\circ} < \theta < 65^{\circ}$). A Further

factor of two refinement around the erupting active region, NOAA AR 11079, and nearby active regions, 11080 (adjacent), 11078 (farther west), and 11081 (north) is also applied.

The initial magnetic field and boundary conditions are derived from a Potential Field Extrapolation (PFFS, (Altschuler et al. 1977)) of synoptic radial magnetic field observations from the MDI instrument. Typically this involves constructing a synoptic map successive slices of observations around the central meridian during an entire Solar rotation. However, for the 2010 June 13 event, ARs 11079, 11080, and 11081 began emerging shortly *after* their position had crossed the central meridian, and are more or less absent from a standard Carrington map for CR 2097. In order to represent these regions consistently in our model, we instead choose the MDI synoptic map created with a slice 45 degrees west of the central meridian, which represents the use of observations ~ 3.2 days after a standard Carrington map. To remove artifacts and correct for unobserved portions near the poles we smoothly transition to the polar corrected central meridian map provided by the MDI project for co-latitudes above 67° and below -67° over a width of $\pm 5^\circ$. A comparison of a standard central meridian magnetogram and the custom magnetogram used in the simulation are shown in Figure 6.3. Utilizing measurements away from the central meridian does increase uncertainty in the radial field, but as is plainly visible, it is a necessary trade-off in order to include the near-eruption conditions around AR 11079.

6.3.1 Pre-Event Conditions

The simulation itself consists of two stages. The initial step is designed to achieve an MHD equilibrium approximating the initial state of the pre-event corona, and the next step is to the evolve the eruption mechanism in time (described in 6.3.2).

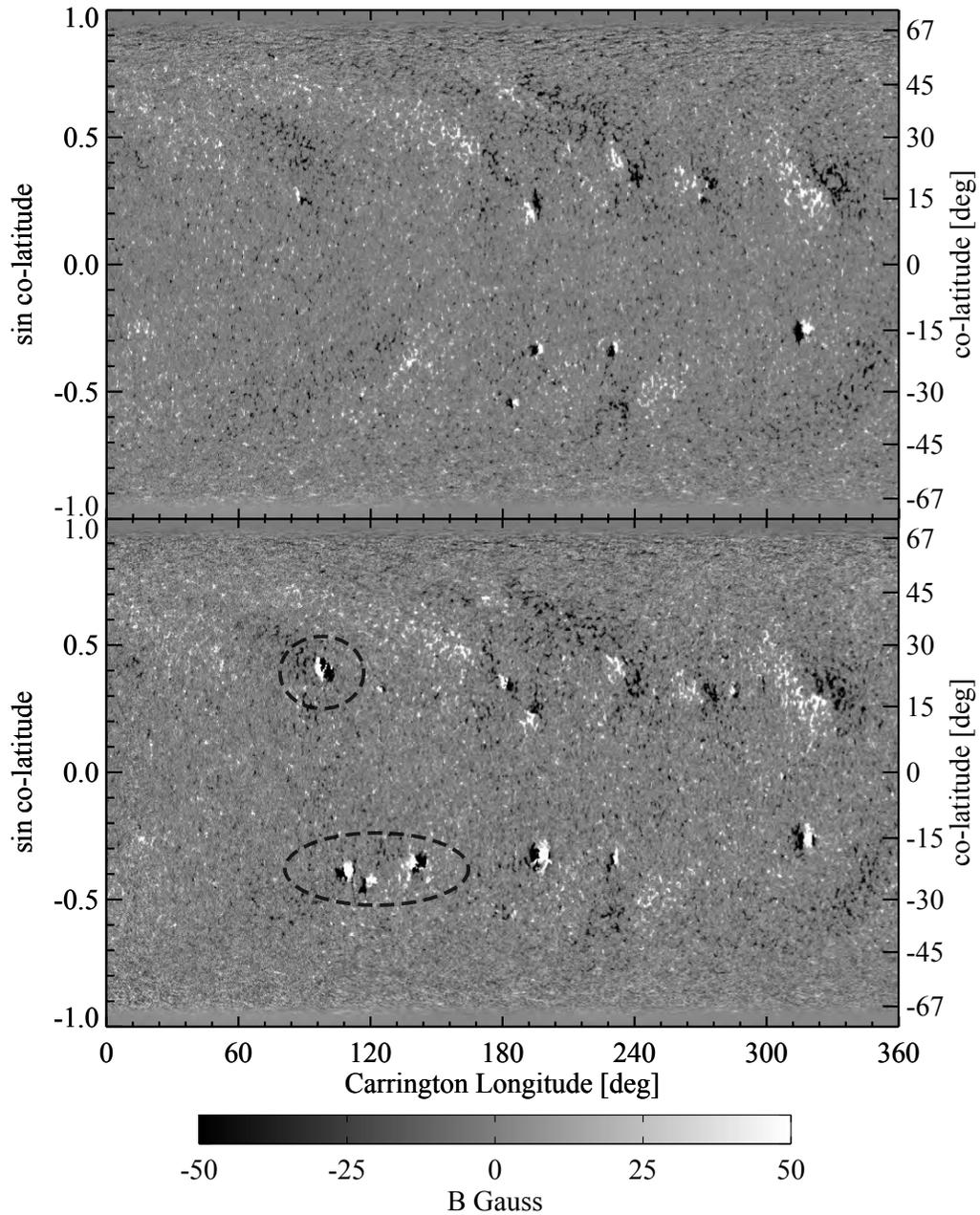


Figure 6.3: A comparison of the Synoptic Magnetograms discussed in 6.3 showing the results using meridional slices of observational data taken from either disk center (top) or 45° to Solar West (bottom). The recently emerged active regions that require the 45° west slice are circled. The NOAA AR numbers are 11080, 11079, and 11078 (bottom circle, left to right)) and 11081 is to the north (top circle).

The 3D volume is first filled with a PFSSM extrapolation of the input magnetogram and a spherically symmetric Parker wind type solution. The system is then relaxed to a quasi-steady state by integrating the full thermodynamic MHD equations the using local time-stepping method (see Tóth et al. (2011); Cohen et al. (2008)). By integrating with chromospheric boundary conditions and a suitable coronal heating model (Downs et al. 2011) thermodynamic balance over the transition region and magnetic topologies in the corona is achieved.

In order to directly compare the simulation results to observational data we must synthesize EUV observables from the simulation. The generation of synthetic EUV images involves using a description for plasma emissivity and detector/filter characterizations to generate a unit response function for each filter, $f_i(T_e, n_e)$, that depends strongly on electron temperature, T_e , and weakly on electron density, n_e . This function is then used to calculate the integrated emission along the line-of-sight through the coronal plasma defined by each pixel:

$$R = \int n_e^2 f_i(T, n_e) dl \text{ DN s}^{-1}, \quad (6.1)$$

where the n_e^2 factor *outside* the filter specific f_i is independent of temperature and reflects that the lines are formed collisionally. This method is based on that described by Mok et al. (2005); Lionello et al. (2009) and a description of its use in the LC model can be found in Downs et al. (2010). The detector response curves used in generating synthetic AIA images in this work are shown in Figure 6.4, which gives pixel response in units of DN s⁻¹ for a unit column emission measure (10²⁶ cm⁻⁵) as a function of T_e for each EUV channel of the AIA instrument. To be consistent with previous work presented in Chapters 4 and 5, the spectral calculations are made using the CHIANTI 5 emission line analysis code (Landi et al. 2006), using

the distribution’s composite abundance file `sun_coronal_ext.abund` and composite ionization equilibrium file `arnaud_raymond_ext.ioneq`. Details on the calibration of AIA can be found in Boerner et al. (2011) and an analysis of the emission properties of the spectral lines observed by AIA as well as their relevance for various solar features can be found in O’Dwyer et al. (2010).

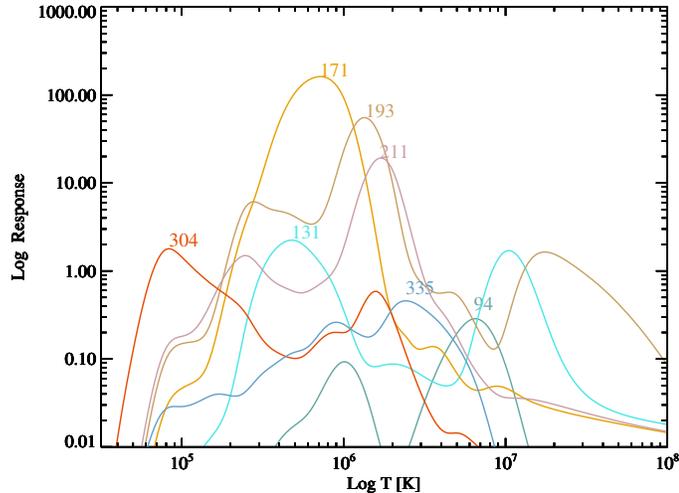


Figure 6.4: Temperature response of the 7 standard EUV filters on the AIA instrument calculated with the CHIANTI 5 spectral synthesis code. The AIA 304, 171, 193, and 211Å, filters have similar response functions to their SOHO/EIT and STEREO/EUVI counterparts (193→195, 211→284) and possess a relatively high S/N due to the preponderance of coronal material emitting at their peak temperatures. AIA 94, 131, and 335Å lines are intended primarily as probes for flare emission (they all have a high temperature component), but all three also possess a cool coronal component as well.

Figure 6.5 shows a pair of tri-color comparisons of AIA-EUV observations and those synthesized from the pre-event simulated conditions. Each tri-color image is an RGB composite of three different EUV filters (emission lines) where each filter is assigned a separate color channel. This serves to immediately highlight temperature-dependent density contrasts, and represents a useful analysis method, readily available due to the synchronized, high cadence imaging of each AIA filter. The top panel displays a tri-color image composite of the Fe IX 171Å (Blue), Fe XII 193Å (Green),

and Fe XIV 211Å (Red) filters, showing the temperature contrast for the three highest signal-to-noise filters of the AIA instrument.

Although the temperature peaks of the EUV filters are relatively broad, the tri-color images do well to highlight the temperature contrast between regions of closed field and open field, particularly on the solar limb. In the simulation the closed, quiet sun (QS), regions possess temperatures ranging from $1.2 \lesssim T_e \lesssim 1.5$ MK and appear reddish-green due to the heightened sensitivity in the 193 and 211Å filters. On the other hand, open, coronal hole (CH) regions range from $0.9 \lesssim T_e \lesssim 1.1$ MK and appear predominantly blue due to their low temperature. The range of temperatures observed is due primarily to the feedback of the coronal heating terms and thermal conduction over the inherently complex 3D magnetic topology. For further comparison, the bottom panel shows an additional tri-color filter set: Fe XII 193Å (Blue), Fe XVI 335Å (Green), and Fe XIII 94Å (Red). The preponderance of the blue and red contribution is due to the sensitivity of the 193 and 94Å filters to plasma in the $1.0 \lesssim T_e \lesssim 1.4$ MK range while for higher temperatures, the high-temperature component of the 335 line becomes relatively stronger.

The ability to capture both the general topological features of the corona and the relative contrast between filters of varying thermal response shows that the model does an adequate job of resolving the pre-event thermodynamic conditions of the corona on 2010 June 13. This is key, because any conclusions we draw on the physical nature of the event require that we accurately represent the conditions in which it propagates.

6.3.2 Eruption Model

The second stage of the simulation involves capturing the time-dependent dynamics of the eruption that generates the EUV wave transient. Because it is critically important

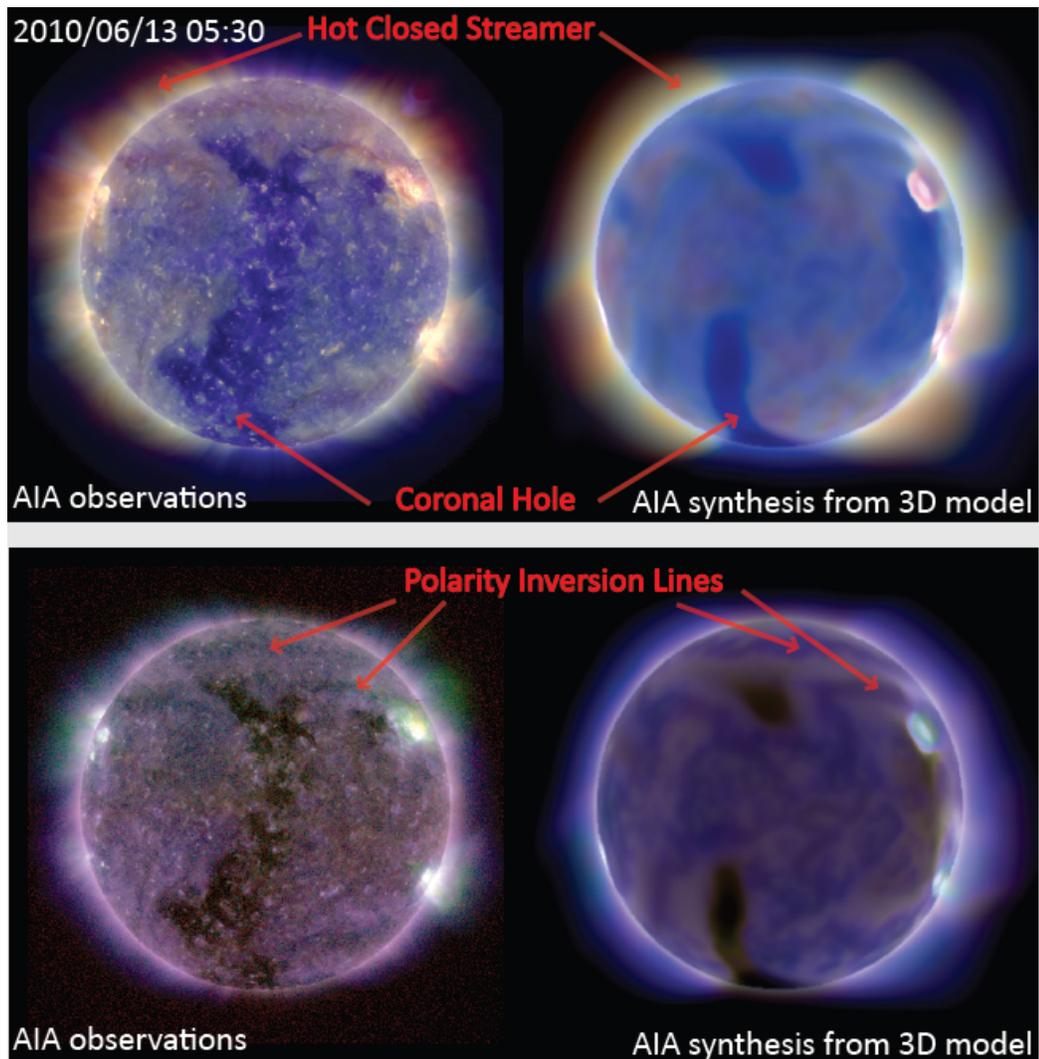


Figure 6.5: Tri-color intensity images of the pre-event state of the corona for observations (left) and emission synthesis from the LC model (right). As described in the text, each RGB color channel contains an intensity image of a particular AIA filter. *Top row:* AIA 171 (B), 193 (G), and 211Å(R) showing the contrast of coronal plasma in the 0.8 to 2.0 MK range. The LC model adequately resolves the geometry and temperature contrast between open field coronal holes and hotter, closed streamer regions. *Bottom row:* AIA 193 (B), 335 (G), and 94Å(R), which provides additional probe and comparison, emphasizing temperatures between 1.0 to 1.4 MK (red, blue) and those above 2.0 MK (green).

that we compare the simulation results directly to AIA EUV data, we require an eruption model that is both applicable to realistic magnetic topologies and does not impose unrealistic temperature and density profiles at or near the source region. To this end we employ the bipolar charge-shearing eruption model first introduced by Roussev et al. (2007). We have previously used this eruption mechanism to study the properties of EUV waves with the LC model (Downs et al. (2011)) and quickly summarize the properties here. In this model additional magnetic flux is added to the the positive and negative polarities of the approximate bipole comprising AR 11079 in the form of two magnetic charges, $+q$, and $-q$ (denoted q_{\pm}), placed at locations \vec{x}_+ and \vec{x}_- 7Mm below the surface, which are perpendicular to the polarity inversion line of the active region, and separated by an initial distance $L_0 = 15\text{Mm}$. A charge value of $|q_{\pm}| = 1.2 \times 10^{11}$ Gauss km² is applied, which corresponds approximately to an additional 58 Gauss in magnitude added to each the existing polarity centers. This roughly doubles the total field strength of AR 11079 at the surface of the model¹. The initial magnetic field configuration, polarity centers, and shear directions are shown in Figure 6.6. Starting from a relaxed MHD solution at $t = t_0$ the charges are sheared in a quasi-steady manner at constant depth along the axis of the polarity inversion line at a linearly increasing speed that reaches $v_0 = 50$ km s⁻¹ at time $t = 5$ min. The shearing motion continues at this speed until $t = 30$ min when the motion is ended. Magnetic flux density at the boundary is preserved by modifying the charge strength to account for the change in distance $q_{\pm}(t) = q_{\pm,t=t_0} L_0^2 / |\vec{x}_+(t) - \vec{x}_-(t)|^2$. The shear speed in the direction of the charge motion is also applied to the velocity boundary condition in the vicinity of each charge. Although this is clearly a simplification of the complexity of CME initiation mechanisms, the application of this scenario leads to

¹The PFSSM extrapolation to the resolution of the MHD model smooths out the highest field strengths seen in the synoptic magnetogram observations (Figure 6.3).

the requisite onset of instability and a large-scale transient that exhibits the general properties of an EUV wave.

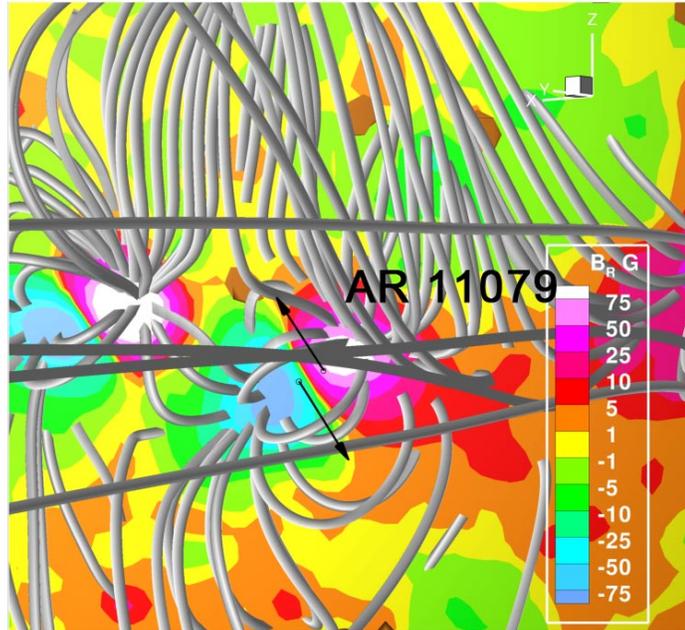


Figure 6.6: Diagram showing the pre-eruption magnetic conditions surrounding AR 11079 as well as the shearing motion imposed by the eruption model. The shearing motion is perpendicular to the polarity inversion line of AR 11079 and primarily stresses the low lying nullpoint between AR 11079 and 11080 (slightly above and to the left of AR 11079 in this image). This ultimately produces a modest eruption in the simulation.

6.4 EUV Wave Simulation Results

With our satisfactory pre-event conditions and eruption model in hand, we simulate the first 50 minutes of EUV wave transient. In order to best match to the evolution around 5:40 and beyond we elect to set the beginning of the shearing process at $t_0 = 5:28$ UT, about 7.5 minutes prior to the beginning of the flaring signal associated with the eruption (Ma et al. 2011). We focus our efforts in two main thrusts: first a characterization of the EUV transient observed by SDO/AIA involving the direct comparison of observations to the same observables synthesized from model data.

And second, an in-depth analysis of the fundamental variables contained in the 3D simulation data, which provide insight to the physical mechanisms that create the multi-component features of EUV transient.

6.4.1 Comparison to EUV observations

Figure 6.7 shows running ratio tri-color images of the EUV event at ten minute intervals for observations (top) and the simulation (bottom). The time difference for the running ratio is chosen to be 48 seconds, which serves to slightly enhance and broaden the filter contrast in the images. Like the tri-color image for the pre-event conditions (Figure 6.5), each RGB color channel represents a separate AIA filter (171 (Blue), 193 (Green), and 211Å (Red)) only now the flux ratios for each band are scaled identically on a linear scale of (1 ± 0.05) . This means that each particular offset in the relative phases or amplitudes of the perturbation for each channel will be spread across the RGB color plane. By nature this representation highlights anti-correlated ratio phases as having strong color components (e.g. negative ratios in 171Å and positive ratios in 193 and 211Å will appear yellow-red, while the opposite would appear bright blue). Correlated phases on the other hand (either all positive (white) or all negative (black)) will be confined to a mostly gray-scale range.

Fortuitously, due to the formation characteristics of EUV emission lines, this tri-color flux ratio method has direct relevance to separating temperature dominated perturbations from density perturbations. As illustrated in Equation 6.1, the bulk of the n_e dependence lies outside of the filter specific response function, which implies that a pure density perturbation will have an identical phase in *all* filters (grayscale in the tri-color plot). A pure temperature perturbation on the other hand will produce a unique, filter dependent signal that depends on the local slope of f_i at

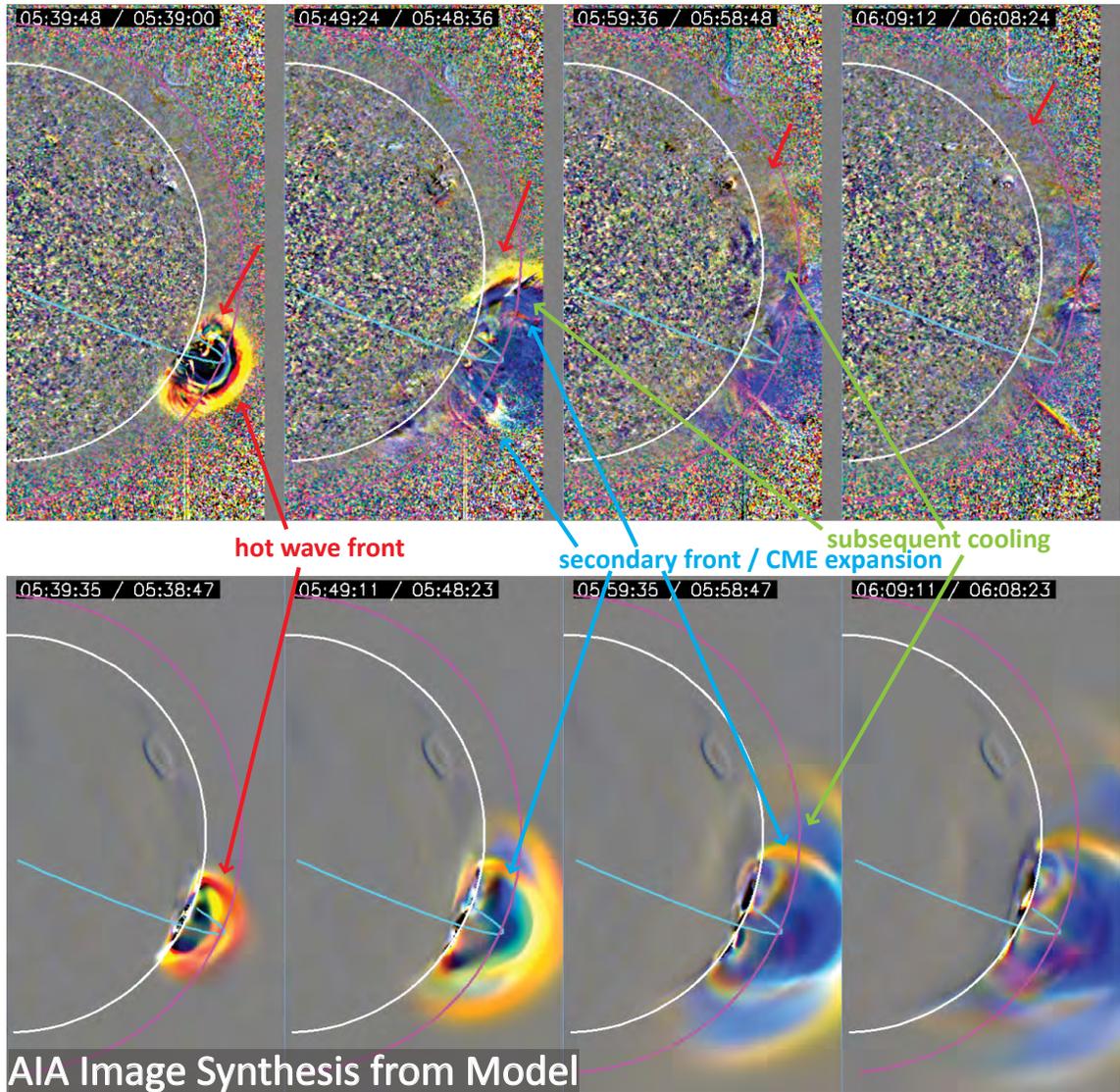


Figure 6.7: Tri-Color running ratio images for the 2010-06-13 eruption using AIA observations (top) and image synthesis from the simulation (bottom). Shown at ten minute intervals, the three channels are AIA 171 (Blue), 193 (Green), and 211Å (Red) 48 second running ratios. The total intensity variation is identically scaled in each channel to a ratio of $1 \pm 3.5\%$. For a scale perspective, the pink arc in each image represents a meridional arc of $1.2R_{\odot}$ centered above the eruption region, while the blue arc is the perpendicular great circle.

a particular temperature and can easily create anti-correlated phases between filters (picture sliding back and forth along the curves shown in Figure 6.4 for a fixed T_e window). Of course, for plausible scenarios both a density and thermal perturbation will be present, but the relative contrast is still immediately apparent, due in part to the steep dependence of the filter response functions on temperature.

The tri-color EUV images of the observations and simulations reveal two primary components that are important to discuss here: The outermost component, labeled in Figure 6.7, shows a nearly isotropic expanding hemispherical or ‘shell-like’ feature that is seen as an enhancement in the 193 and 211Å filters and as a relative flux *decrease* in the 171Å filter (this is seen as a strong yellow-red color, red arrows in the tri-color images). As this component passes, the relative sign of the perturbation reverses in sign for all three filters and is seen as an enhancement in the cool 171Å line (blue coloring, green arrows)). As discussed above, these color/phase signatures are highly suggestive of a heating and cooling cycle that occurs as the transient passes. This is not a new observational feature of EUV waves (e.g. Dai et al. (2010); Downs et al. (2011); Liu et al. (2011)), but it is captured with extreme clarity due to the high cadence multi-filter observing program of AIA. We identify this ‘hot-front’ explicitly as the main EUV-wave component in the ensuing discussion.

Although somewhat difficult to see at later times, also present in the running ratio images is a secondary front that exhibits somewhat different properties than the outer EUV wave. Identified as the CME by Patsourakos et al. (2010b) this front initially appears a strong hemispherical perturbation that is trailing the outer front (leftmost frame, 5:39:48 UT). As it expands, the transverse motion of this front is much slower and an extended cool dimming region is left in its wake. We identify this secondary component explicitly as the non-linear or CME component in the ensuing discussion.

A full kinematic picture of the wave can be gleaned by constructing a time-distance representation of the EUV flux along a fixed set of points in space. Analogous to the time-distance diagrams described in Downs et al. (2011) (Section 5.2.2), we construct tri-color time distance diagrams along an $r = 1.2 R_{\odot}$ that spans the western limb (we can examine a larger height than in the previous work because of the higher S/N ratio off of the limb for the binned AIA images). Shown in Figure 6.8 is the tri-color time distance diagram for this event at 24 second sampling, which readily shows the speed and thermodynamic characteristics of the wave (outer ‘v’ shape) as a continuous function of time (scale is now $1 \pm 1.5\%$). Additionally the secondary enhancement that we identify as the ‘CME-component’ is much more clear and appears as the inner ‘u’ shape. Unique about this component is the fact that the tri-color perturbation color signal is noticeably different than the outer EUV front, first appearing light blue then light pink at later times, suggesting a significant density change that competes with the thermal changes. Most importantly we observe that this component slows enough that it remains confined to the latitudes between -45° and 0° , again a markedly different behavior than the outer EUV front, which propagates further and only mildly changes slope.

Flux Comparisons

The main outer component of the EUV wave transient is further characterized by looking directly at the signal perturbation at various locations. Figure 6.9 shows flux versus time plots for AIA 171, 193, and 211Å channels for four position angles along the $r = 1.2R_{\odot}$ arc shown in Figure 6.7. Moving from north to south, panel (a) shows the flux evolution of the outer front far from the eruption site. The phase behavior that produces the color behavior of hot-front in Figures 6.7 and 6.8 is explicitly seen as anti-correlated slopes between the cool 171Å filter and the hotter 193 and 211Å

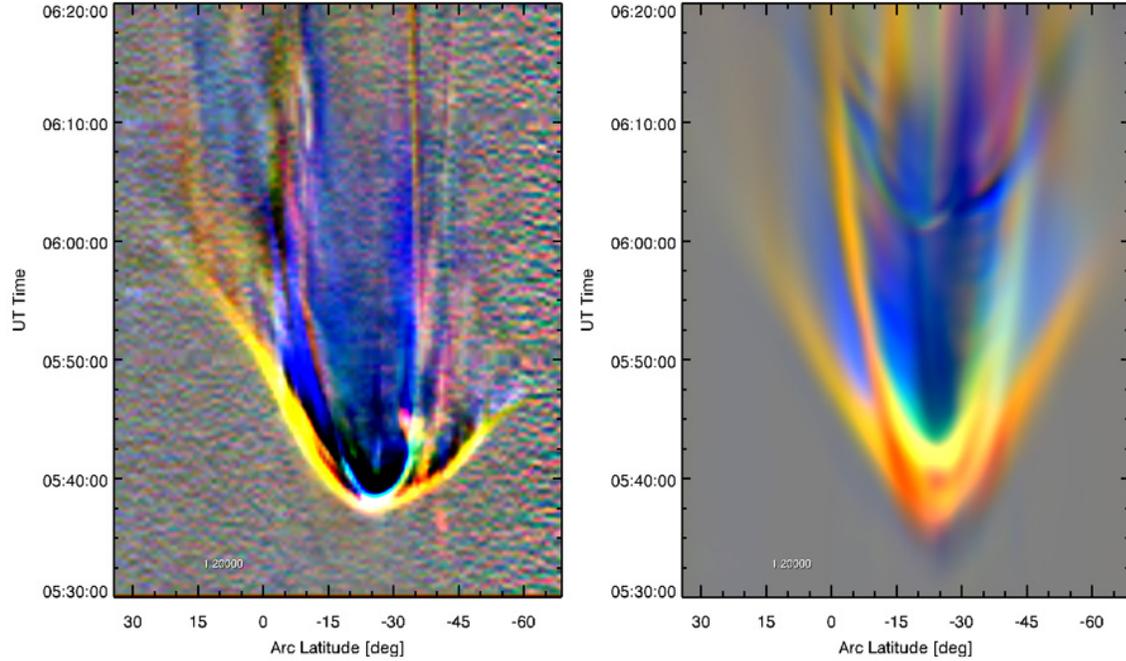


Figure 6.8: Tri-color time distance diagrams made from observations (left) and model synthesis (right). The color channels are the same as in Figure 6.7 but they are now scaled to $1 \pm 1.5\%$ and show 24 second running ratios extracted along an $r = 1.2R_{\odot}$ arc off of the solar limb (pink arc in Figure 6.7). This readily shows the speed (slope) and thermodynamic characteristics of the wave (outer ‘v’ shape) as a function of time, which exhibits initial heating (yellow red) and subsequent cooling (blue) as it passes a fixed location. Additionally the secondary enhancement due to the CME component appears as the inner ‘u’ shape, which remains confined to the latitudes between -45° and 0° . Note: the synthetic image shows a secondary transient ‘u’ feature at 6:08 UT, this is an unfortunate artifact due to halting of the shearing process ($50 \rightarrow 0 \text{ km s}^{-1}$) and is not physically meaningful.

filters, which is preserved in the presence of structures in a time-varying amplitude. Similar characteristics are observed in panel (b), taken at a latitude that is closer, but still relatively far from the eruption site. The overall amplitude here is higher, which is consistent with a pulse decreasing in amplitude as it propagates. Of note in both panels (a) and (b) is that all three of the filters share common inflection points (zero-crossings), which suggests that a common heating cooling mechanism is at play, rather than strong density modulation (would produce a common slope) or LOS effects involving multiple regions altering their temperatures. Comparing to the simulation for these locations, we see that the simulated transient does well to capture the anti-correlated phases and inflection point features in addition to recovering the overall width of the initial front and its arrival time (speed). However, the subsequent substructure that follows the initial front in observations is not particularly well produced, possibly a result of the difficulty of resolving the fine-scale structures and thermodynamics of the ambient corona with a global MHD model (see discussion in Chapter 4 and appendix C).

Closer to the eruption (panel c) the oscillation is present but modulated in the AIA observations. The 171\AA flux does not share the same inflection point as 193 or 211\AA and all of the three flux ratios do not return to zero. This suggests that we are observing a mix of linear and non-linear features due to the proximity to the eruption site and subsequent passage of the secondary front. Lastly, the location examined in panel (d) is in the path of the southern front and very near to the observed boundary between the closed field streamer and southern coronal hole. Both model and observations show the same qualitative phase relationship but the observed front is sharper (less broad) here than in the northern front and in the simulated flux ratio, and also passes about five minutes earlier than the simulation. Both effects are likely due to the increased propagation speed of the southern front with respect

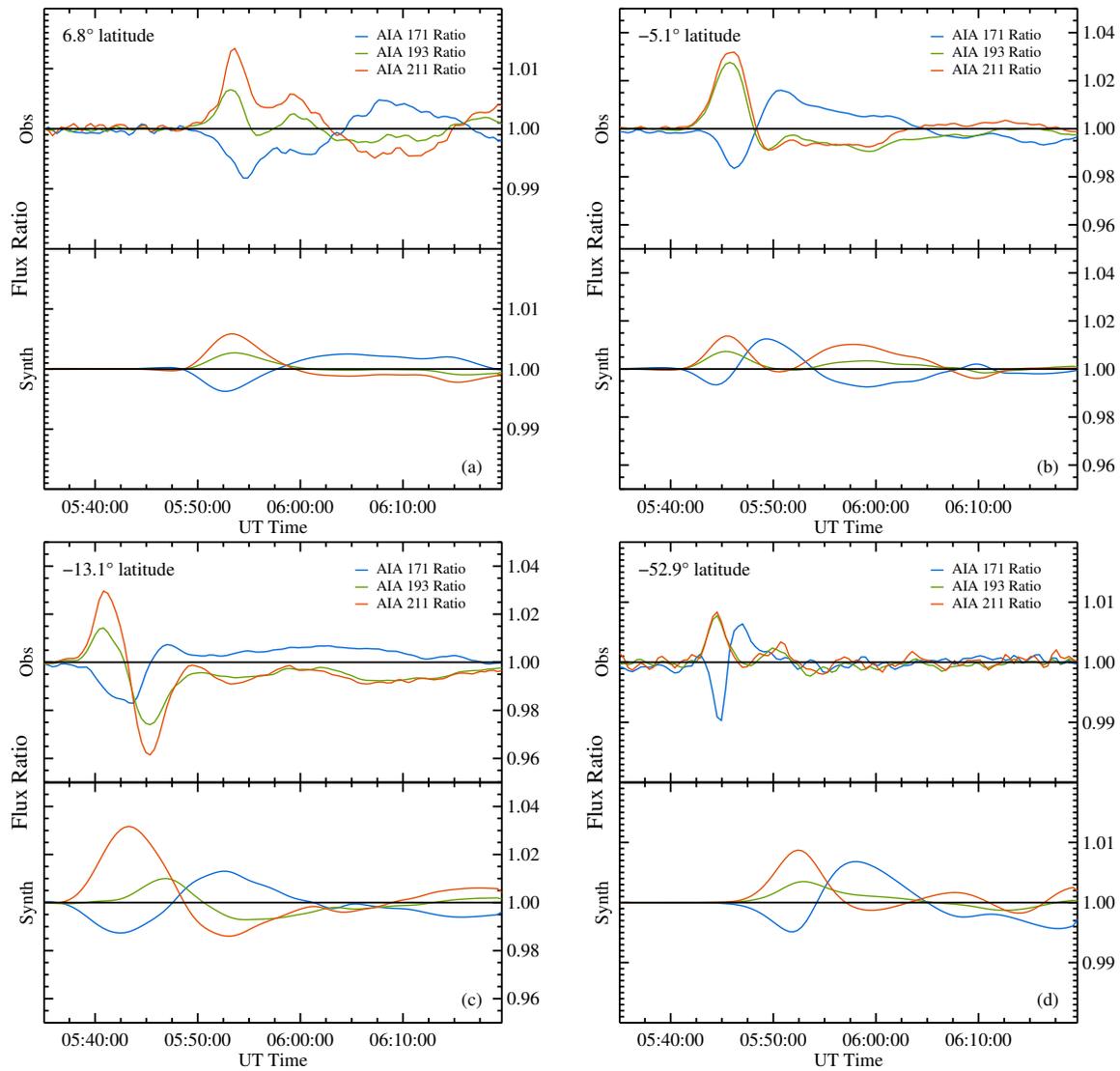


Figure 6.9: Flux versus time plots for the AIA 171, 193, and 211 Å channels comparing the observations (top traces) to model synthesis (bottom traces). The panels show fluxes extracted at four position angles along a $r = 1.2R_{\odot}$ off of the solar limb (pink arc in Figure 6.7). Arc positions (a), (b), and (c) are located in the path of the northern front, while arc (d) is located in the path of the southern front. Refer to the x-axis of Figure 6.8 for a sense of where these latitude positions lie with respect to the front.

to the northern front, which is not resolved in the model. We posit that this is due to the presence of relatively stronger field (faster magneto-sonic speed) in this region of the corona than is resolved in the model. Polar regions (particularly open/closed boundaries) are always more difficult to reproduce in magnetic extrapolations than equatorial regions, directly because the LOS component of the observed magnetic field measured at the surface gets further away from radial as we near the poles. At any rate, the correlation of the front with the fast magnetosonic sound speed is investigated in Section 6.4.2.

The inner, secondary component of the event is more difficult to pick out in running ratio observations due its slow transverse speed, so we instead turn to examining the base ratio for EUV flux relative to 05:30:02 UT. Unlike the running flux ratios, base processing highlights the zero-order non-linear changes that occur in the coronal plasma. Zero-order change is, of course, expected to be introduced by the CME eruption itself which often causes mass depletion and reduced EUV emission (coronal dimming, see Aschwanden (2009) for example). In Figure 6.10, we show the base ratio flux evolution for the event at three times along the entire $r = 1.2 R_{\odot}$ arc (note the reversal of time-space roles with respect to 6.9, as now arc latitude is the continuous variable). The strong non-linear (as high as 1.5 in 171\AA) evolution of this component creates the large peaks at nearly fixed latitudes along the arc, marking the edges of the volume carved out by the eruption. This forms the ‘well’ shaped signal (deep minimum, side maximums) spanning approximately -45° to 0° latitude in Figure 6.10. The model does well to reproduce the size of the secondary EUV perturbation caused by the CME but not the deep dimming (mass depletion) and precise thermodynamic signal (too much enhancement in the 211\AA channel).

Through this analysis we demonstrate that many of the important observational characteristics of the the EUV transient are captured by the simulation. This includes:

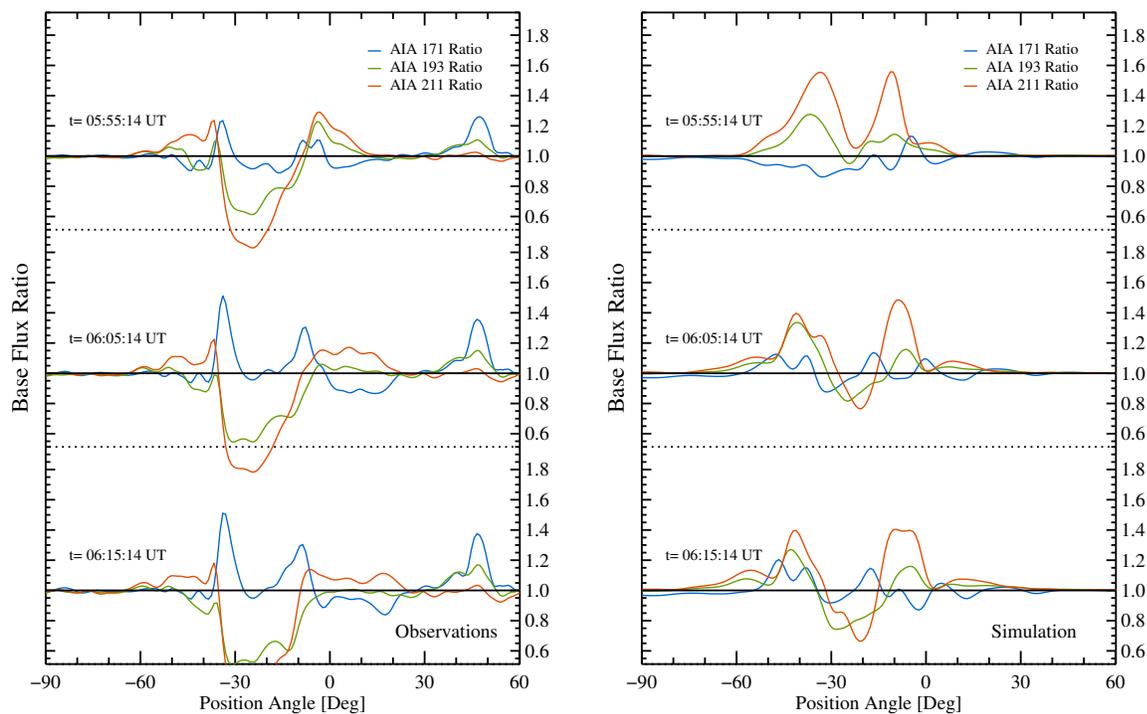


Figure 6.10: Base flux ratio measured along the $r = 1.2R_{\odot}$ arc at $t = 05:55:14$, $06:05:14$, and $06:15:14$ UT for observations (left) and the simulation (right). The base time chosen for the flux ratio is $05:30:02$ UT, and the trace for each filter is interpolated to a common time. The secondary EUV component is identified as the ‘well’ shaped signal (deep minimum, side maximums) spanning approximately -45° to 0° latitude. The EUV wave is barely perceptible in this representation ahead of the CME flanks due to its low absolute amplitude ($\lesssim 5\%$). The signal at $+45^{\circ}$ latitude is caused by the rising of an unrelated prominence off of the northwest limb.

- The extent and speed of the outer EUV wave in the northern direction.
- The approximate width of the initial pulse.
- The anti-correlated filter phases that indicate heating/cooling within the front.
- The kinematics and physical extent of the secondary CME component.

6.4.2 Analysis of the 3D data

In order for the coupled observation and modeling analysis to succeed it is critically important that the simulated EUV wave reproduce the basic characteristics of the observations. However, matching these observations alone do constrain the physical mechanisms behind the perturbation signal. In order to address this we turn to analysis of the temporal evolution of the full 3D set of eight MHD variables namely: density, ρ , vector velocity, \vec{v} , vector magnetic field, \vec{B} , and electron temperature, T_e . *Note:* from hereafter simulation time references will be with respect to the beginning of the simulation, $t_0 = 05:25:00$ UT.

First off it is important to correlate the main time-dependent components discussed in the EUV analysis to variables from the simulation data directly. From our experience in Downs et al. (2011) and this work, we find that the best variable to correlate the MHD data to the EUV perturbation in the synthetic images is the density perturbation. Although the temperature plays an important role in determining where a parcel of plasma lies in a given filters thermal response curve (Figure 6.4), it is the outer n_e^2 dependence that is guaranteed to modulate the signal regardless of temperature. In order to isolate the time-evolving transient over the background, we take snapshots of the 3D simulation every 48 seconds and calculate the

running ratio of density at *all* points in space, and use this variable in the discussion below.

Correlation to the Fast-Mode Speed

The next order of business to begin examining the applicability of the various EUV wave mechanisms to the simulation results, beginning with the most popular candidate: EUV wave as fast-mode waves. Fortunately the ambient magnetic field and position of the erupting active region provide excellent conditions to test the correlation of the EUV perturbation with the local fast-mode wave propagation speed, c_f in the corona. The fast-mode speed varies depending on propagation angle with respect to magnetic field, so we use the maximum value, $c_f^{max} = \sqrt{v_A^2 + c_s^2}$, where $v_A = |\vec{B}|/\sqrt{4\pi\rho}$ and $c_s = \sqrt{T/\gamma\rho}$ are the Alfvén and sound speeds of the plasma respectively. Shown in Figure 6.11 are color contours of c_f^{max} for both the SDO and STEREO-A perspectives at twelve minute intervals. The EUV wave evolution is highlighted in each frame by overlaying line contours of positive values of running density ratio, which helps to isolate the outer front in particular.

Starting with the SDO/AIA perspective (top row), we see that in the northern direction of propagation, away from the high localized field of the active region, c_f is fairly uniform for a large volume and confined to a narrow range of $\sim 200 - 350$ km/s (200 km/s represents a floor set by c_s for million degree plasma, which is independent of $|\vec{B}|$). However, in the southern direction, the presence of a nearby coronal hole (lower n_e and T_e , higher $|\vec{B}|$) enforces that c_f begins increasing rapidly over a short distance when the coronal hole boundary is reached. If the transient is indeed a pure fast-mode wave this would imply significantly different characteristics between the North/South fronts of the wave, which is precisely what is observed. As the northern portion of the front propagates, it retains a roughly hemispherical

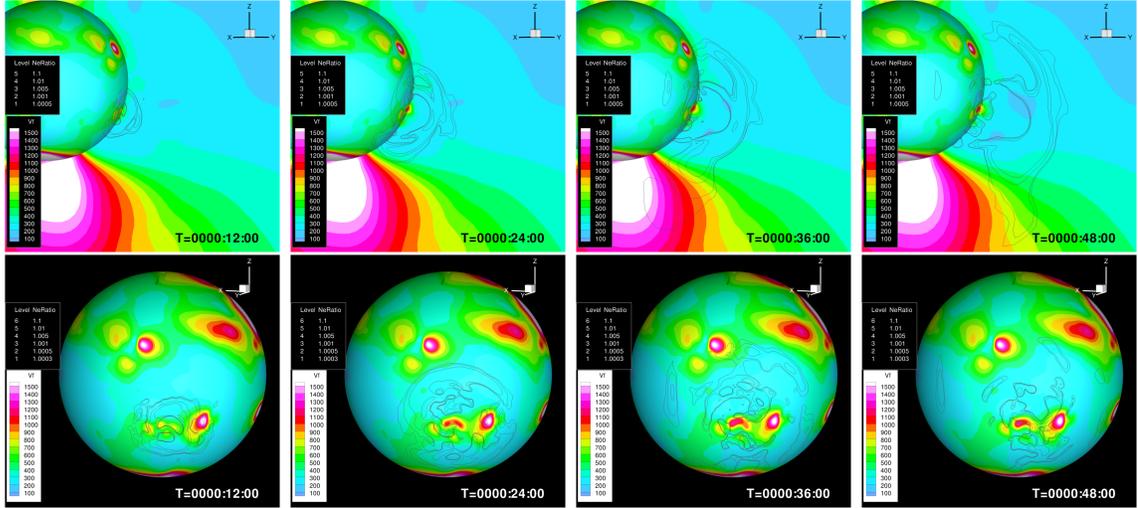


Figure 6.11: Correlation of the density enhancement (black contour lines) with the perpendicular fast-magnetosonic speed (color contours) from the AIA perspective (top) and the STEREO-A/EUVI perspective (bottom). Both perspectives show c_f and the density ratio on a sphere of $r = 1.1R_{\odot}$, and also the meridional plane intersecting AR 11079 for the top AIA perspective. The outer evolution of the black contour lines track the global EUV perturbation, which shows a clear alteration in shape as it encounters the southern coronal hole. Also visible from the STEREO-A perspective is the steeping and slowing down of the eastern front as it encounters the region of smaller c_f as well as the loss of signal as it encounters the northern active region.

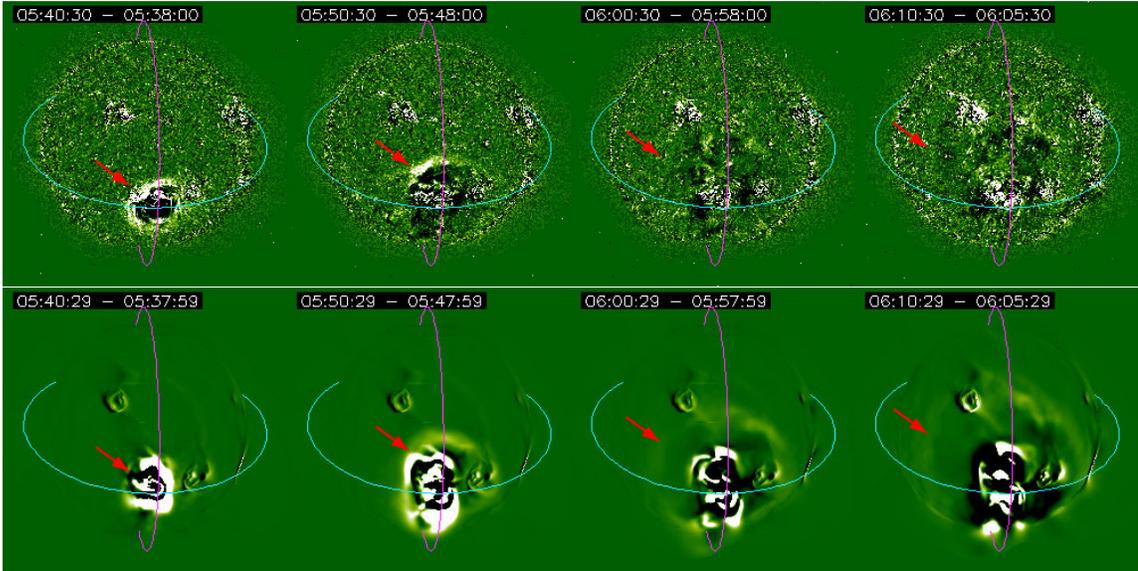


Figure 6.12: A comparison of EUVI-A observations (top) to EUVI-A image synthesis (bottom) of the EUV wave transient in the simulation. The running difference processing is the same as in Figure 6.2, and the red arrows tracking the eastern propagation of the transient are at identical locations for each column. The outer EUV front in the synthesized data appears at the same locations as the perturbed density contours in Figure 6.11 and tracks the shape of the observed front quite well in the eastern, northern, and western directions.

shape, which is expected for uniform propagation speeds. To the south however, as the front begins to encounter the large gradient in c_f its collective shape appears to both speed up and shear/refract to a more broad north south alignment, one far removed from the original hemispherical shape. In wave terms this collective behavior would be expected, as each individual wave packet will (i) travel at slightly different speed, altering the location where the enhancements line up, hence shape of the front (ii) undergo broadening (due to speed increase) and (iii) experience a significantly increased reflection probability (due to speed gradient).

Now turning to the STEREO-A/EUVI perspective (Figure 6.11, bottom row) we observe an analogous situation play out over the solar disk. Initially ($t < 25$ min) the eastern (left), northern, and western propagation of the outer front is through regions with a roughly comparable value of c_f . At this time the roughly circular nature of the front is preserved (a circle is the projection of a hemisphere on the disk). At later times, two interesting features are observed: First, in the eastern direction, the transient encounters a large region with a relatively smaller value of c_f (extended quiet sun) and exhibits both a slowing down and *steepening* in relative magnitude. This resembles the behavior of wave-packets steepening as they begin piling up when forced to slow down due to decreased propagation speed. Second, the transient eventually encounters the influence of the AR 11081 and adjacent high-field region in the north, which provides a relatively sharp increase in c_f . As it encounters AR 11081, the northern transient begins to broaden and distort the originally circular shape, eventually losing visibility at this scaling level, characteristics that again support the wave hypothesis. The applicability of this analysis is confirmed by comparing the STEREO-A/EUVI 195Å observations directly to synthesized images, which is done in Figure 6.12. The eastern propagation of the front in observations is reproduced by the model and is coincident with the density perturbation shown in Figure 6.11.

Additionally, the relative absence of the transient signal above the northern AR is reproduced.

Phase Analysis

In order to gain further insight into the wave nature of the extended front we turn to considering the linearized MHD equations in a uniform medium. There are numerous ways for expressing the characteristic waves in MHD, and for purpose of this discussion we use the form presented in Lectures 19-24 of Schnack (2009) and refer the reader there for complete details. Assuming a uniform magnetized medium with no flow, first decompose the system into a constant background $(\rho_0, \vec{v}_0=0, \vec{B}_0, p_0)$ plus linear perturbations about the background $(\rho_1, \vec{v}_1, \vec{B}_1, p_1)$. This representation can be used to linearize the ideal MHD equations by substituting this form and then canceling derivatives of constant quantities and terms involving more than one power of perturbed terms. Now, given a small linear displacement of a fluid element about its equilibrium position, $\vec{\xi}$, an evolutionary equation for $\vec{\xi}$ can be directly formulated:

$$\rho_0 \frac{\partial^2 \vec{\xi}}{\partial t^2} = \frac{1}{\mu_0} (\nabla \times \vec{B}_0) \times [(\nabla \times (\vec{\xi} \times \vec{B}_0))] + \frac{1}{\mu_0} \left\{ \nabla \times [\nabla \times (\vec{\xi} \times \vec{B}_0)] \right\} \times \vec{B}_0 + \gamma \nabla (p_0 \nabla \cdot \vec{\xi}) \quad (6.2)$$

Standard solutions for the characteristic eigenvalues and eigenfunctions can be determined by substituting a plane wave solution, $\vec{\xi}(\vec{r}, t) = \vec{\xi}_0 \exp[i(\vec{k} \cdot \vec{r} + \omega t)]$, where, \vec{k} is the direction of propagation, which leads directly to the separation of the three MHD wave modes: the fast and slow magnetosonic waves, and Alfvén waves. Additionally, any linear displacement $\vec{\xi}_0$ can be represented as a linear superposition of the eigenvectors of each of the three modes, $\vec{\xi}_0 = \sum_i \vec{\xi}_i(\vec{k})$. What is most pertinent to take from this discussion is the relative phases of the velocity and density perturbation

respectively:

$$\vec{v}_1(\vec{r}, t) = \frac{\partial \vec{\xi}}{\partial t} = i\omega \vec{\xi} \quad (6.3)$$

$$\rho_1(\vec{r}, t) = -\nabla \cdot \vec{\xi} = -i(\vec{k} \cdot \vec{\xi}). \quad (6.4)$$

Since the velocity perturbation is a vector quantity it is difficult to analyze because its projections depend on a choice of coordinate system, we go further and examine the phase of its divergence, a scalar quantity:

$$\nabla \cdot \vec{v}_1 = -\omega(\vec{k} \cdot \vec{\xi}). \quad (6.5)$$

Because of the additional derivative, $\nabla \cdot \vec{v}_1$ is 270° out of phase of ρ_1 , which makes for a unique signature to look at when identifying components in the simulation that exhibit linear, compressible, wavelike behavior.

In order to apply the above illustration to variables calculated in the simulation, we make the identification of $\rho_1 \rightarrow n_e$ running ratio, and $\nabla \cdot \vec{v}_1 \rightarrow \nabla \cdot \vec{v}$ running difference. The running method is chosen because it isolates the short term low amplitude transient from long term variations. We should note here that this calculation technically adds an effective derivative and is noisier, however this acceptable because the phase relationship will still be preserved by definition.

The top panels of Figure 6.13 show a comparison of the running difference of $\nabla \cdot \vec{v}$ (color contour) and running ratio of n_e (lines) for $t = 28$ and 44 min with a 48sec ratio/difference. Examining the outer component of both the southern and northern front at $t = 28$ min we observe the characteristic signature of a 270° phase relationship, i.e. a positive to negative sign reversal for $\nabla \cdot \vec{v}$ at the peak the of n_e enhancement. 16 minutes later this feature is still quite conspicuous in the north

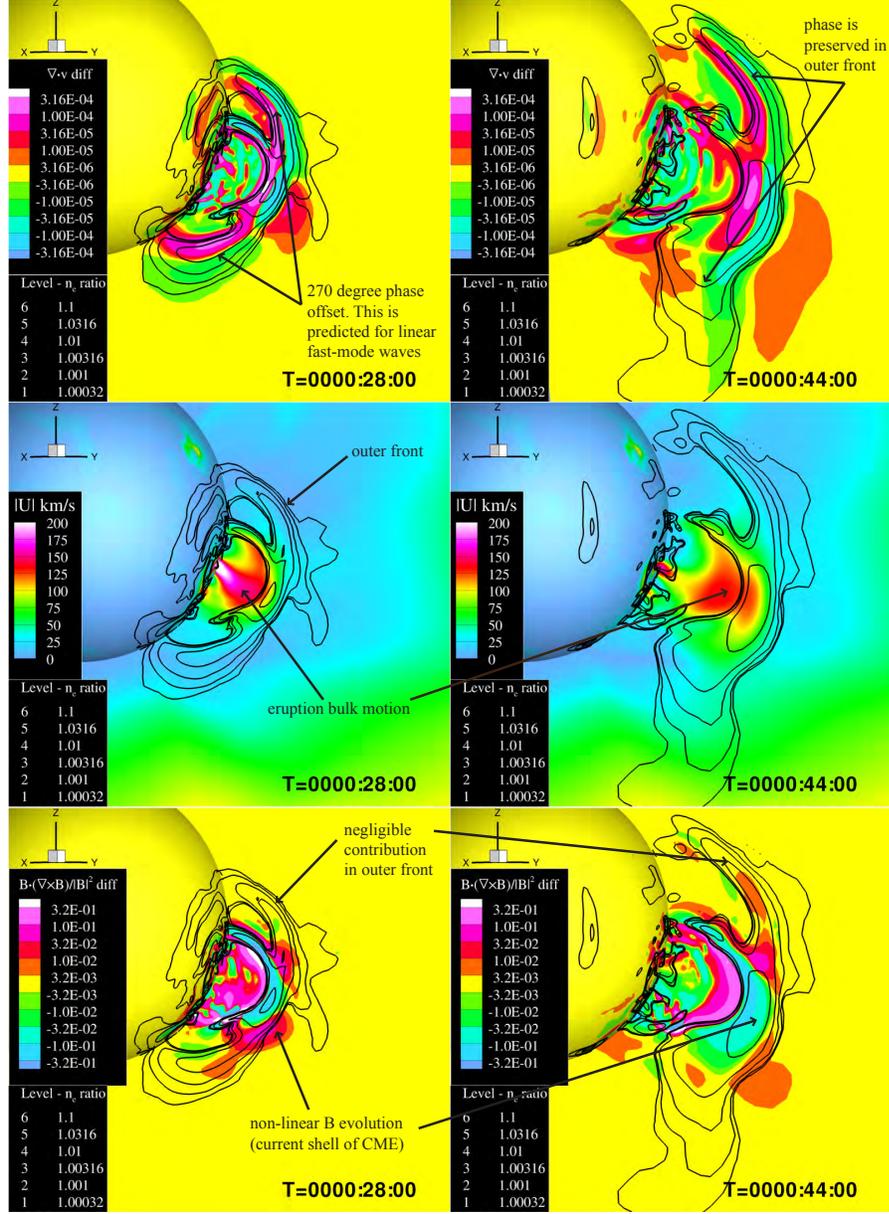


Figure 6.13: Snapshots of the simulation at $t = 28:00$ min (left) and $t = 44:00$ min (right) for three parameters on the meridional plane intersecting AR 11079 and sphere of $r = 1.1R_{\odot}$. The identical black contours in each panel represent positive values of running density ratio (perturbed ρ_1). *Top row:* the relative phases of the perturbed density and velocity divergence, $\nabla \cdot \vec{v}_1$ (color), showing a 270° phase offset in the outer front. This can be identified by looking at the location of the positive to negative inflection point of $\nabla \cdot \vec{v}_1$ (pink \rightarrow yellow \rightarrow blue shows $+$ \rightarrow 0 \rightarrow $-$), which resides precisely along the peak of the the positive density perturbation. *Middle row:* the magnitude of the fluid velocity ($|\vec{v}|$) showing the bulk motion of the CME as it propagates outward. Large, non-linear changes in $|\vec{v}|$ are localized to the region directly above the eruption and are absent from the outer front that exhibits the EUV wave behavior. *Bottom row:* the running 48 second difference of the current parameter α for both times. The strong positive and negative values of this parameter define the “expanding current shell” which is directly correlated with the bulk velocity enhancement in the middle row, and *not* the outer EUV wave front.

where the sound speed is still relatively low and uniform. It becomes distorted in the south due to the passage into the coronal hole region, but the phase relationship remains quite clear. This reinforces and is consistent with the wavelike behavior discussed in the previous section (also see Figures 6.11 and 6.12).

A necessary step in this analysis is to now separate the fast-mode wave component from that of the non-linear evolution of the CME eruption itself. We illustrate this in two ways, first by examining the bulk velocity of the eruption and then by looking at the currents that are produced, both of which help localize the CME component of the EUV perturbation. The middle panels of Figure 6.13 show the absolute value of flow velocity for $t = 28$ and 44 min. Immediately apparent is the relatively central locality of the bulk velocity of the CME. The outer compression fronts identified in the top panels show little absolute velocity difference from their surroundings, while the central core of the CME itself is accelerated to a few hundred kilometers per second and is flowing outwards.

Further evidence supporting a separation between non-linear CME evolution and the EUV wave can be found in the MHD currents formed during the eruption. The bottom panels of Figure 6.13 show running difference values of the parameter $\alpha = \vec{J} \cdot \vec{B}/|\vec{B}|^2 = (\nabla \times \vec{B}) \cdot \vec{B}/|\vec{B}|^2$ for the same times and cadence as the top panels. A critical parameter supporting the current shell hypothesis discussed in a simulation by Delannée et al. (2008), α is a scalar quantity that illustrates where field-aligned currents are strong relative to the local magnetic field. Indicative of non-linearly evolving magnetic structures, this parameter traces regions of expanding and contracting systems of magnetic flux within the CME eruption. Note that for a purely linear displacement, α is identically zero because it can be shown that the vector pair (\vec{J}_0, \vec{B}_1) and (\vec{J}_1, \vec{B}_0) are both mutually orthogonal for all eigenmodes. Comparing the three rows of panels in Figure 6.13 we see that α is localized to the eruption

region and strongly correlated with the bulk velocity of the CME, and *not* strongly associated with the outer front of density perturbation. This allows us to identify this component of non-linear evolution as the manifestation of the often discussed non-wave components theorized to explain EUV waves. This current evolution resembles the ‘field line stretching’ model discussed by Chen, F. et al. (2011), the ‘current shell’ model of Delannée et al. (2008), and the ‘non-wave’ components modeled by Cohen et al. (2009); Downs et al. (2011).

6.5 Discussion and Conclusions

In this work we explore the physical underpinnings of the 2010 June 13 EUV wave by characterizing the event within a 3D time-dependent thermodynamic MHD model of the global corona. The crux of this analysis relies on the assertion that the transient simulated in the model provides a realistic accounting of the true event that is observed. This connection is established by the forward modeling of observational data (EUV images), the results of which can be used for a direct comparison to observations. This is done on a one-to-one basis qualitatively for the pre-event conditions (Section 6.3.1 and Figure 6.5) and quantitatively for the time-dependent signature of the EUV transient (Section 6.4.1 and Figures 6.7 to 6.10 and 6.12). With this important link in place, we find strong evidence in the simulation that the outer, propagating component of the perturbation exhibits the unequivocal behavior of a fast-mode wave. We also find that this component becomes decoupled from the evolving structures associated with the Coronal Mass Ejection that are also visible (Section 6.4.2 and Figures 6.11 and 6.13). This provides strong support for the fast-mode wave interpretation of EUV waves (Gopalswamy et al. 2009; Patsourakos et al. 2009; Patsourakos & Vourlidis 2009) and models combining both wave and

non-wave components, where the fast-mode wave is primarily responsible for the outer propagating front (Cohen et al. 2009; Downs et al. 2011). Before going on the implications of these results for purely non-wave explanations for EUV waves are discussed below.

6.5.1 Relevance to Proposed ‘Non-Wave’ Mechanisms

Field Line Stretching Model: The idea of an EUV wave event possessing both a fast-mode wave and trailing non-linear component is not new. In fact the ‘field-line stretching’ model originally proposed by Chen et al. (2002) and subsequently studied by Chen et al. (2005); Chen, F. et al. (2011) (among others) predicts exactly this situation (discussed in Section 2.6.1 and Figure 2.11). The key distinction however is in the physical mechanism responsible for the EUV emission in the globally propagating front. In an effort to unify coronal signatures with Moreton waves (fast-mode waves traveling at high speeds in the chromosphere) the field-line stretching model proposes that a coronal Moreton wave (fast-mode wave) is launched during the eruption and propagates freely in all directions under coronal conditions. The EUV signature however is not produced by this the coronal Moreton wave (argued to be relatively undetectable) and instead it is the subsequent expansion of the CME and surrounding of the arcade that creates this signature. The enhanced emission produced by the ‘stretching’ of field pulled along with the CME and its subsequent compression on the surrounding regions, this behavior was also observed and studied in our previous study (Downs et al. 2011). For the 2010 June 13 event we find both strong evidence for both components as well, and in a semantic sense confirm their scenario. However, our analysis confirms that outer fast-magnetosonic wave component is not only observable but is in fact *clearly* responsible for the ubiquitous

features of EUV waves, (nearly isotropic at onset, large transverse propagation distances, modulation due to local fast mode magnetosonic speed, decoupling from the CME source region). This is a significant *physical* distinction.

Current Shell Model: Briefly mentioned in the analysis of the current parameter, α , in Section 6.4.2 and Figure 6.13, is another non-wave theory for the transient EUV signature of the outer front: the ‘current shell’ model proposed by Delannée et al. (2008) and subsequently explored in Delannée (2009); Schrijver et al. (2011). As discussed in Section 2.6.1 and Figure 2.9, this scenario features an erupting flux rope that forms an expanding shell or layer of localized MHD currents as it impinges on the surrounding field in the corona. This represents the non-linear contribution of the changing magnetic field in the induction equation (Equation 3.4). These currents are then thought to generate an observable EUV transient by heating the coronal plasma as they dissipate. Indeed we can identify this phenomena taking place in both the EUV observations and in the MHD simulation of the eruption. However, it is the location of these currents that are problematic for this model to apply to this event. As shown in Figure 6.13, the current shell is confined (as expected) to the region of the CME itself and *does not* extend into the outer front that is observed. Furthermore the heating and cooling observed in the outer front is completely consistent with that of a compressible wave, whose nature is confirmed by the relative phase analysis.

Reconnection Front: Another explanation for the characteristic signature of EUV transients is the ‘reconnection-front’ model proposed by (Attrill et al. 2007a) and argued observationally by Attrill et al. (2007b); Dai et al. (2010). In this scenario, the EUV wave signature is generated by successive reconnection events of favorably oriented field with the expanding field of the CME eruption. These successive

reconnection events dissipate magnetic energy, conducting thermal energy upwards along connected magnetic field lines, ultimately creating the collective front that is observed. As with our previous work (Downs et al. 2011) we do not find evidence for these mechanisms playing a role outside of the immediate vicinity of the eruption region (which is complicated by all the other non-linear terms). A thermal conduction front due to reconnection would necessary need to be correlated to the CME evolution (not the case for the outer front), and would not be directly correlated to fast-magnetosonic speed (contrary to what is observed).

Slow Mode Mechanisms: The last set of ‘non-wave’ explanations for EUV waves that we briefly address are the various works that explore the applicability of slow-mode mechanisms. Although the slow-mode is indeed a wave characteristic of the MHD equations, due to the unusual nature of slow-mode waves EUV wave mechanisms employing them typically invoke non-linear slow-mode processes, such as a coherent soliton pulse (Wills-Davey et al. 2007) or the steepening of a slow-mode shock, such as the one described in Wang et al. (2009). Although we do not address any particular slow-mode theory directly here, we do not find strong evidence for slow-mode mechanisms contributing to the extended outer front. First off, in the transverse directions (north, south, east, west) the outer front does not develop characteristics indicative of an MHD shock, the pulse remains in a linear regime (sub 5%) while decaying and does not incur large enough flow velocities (Figure 6.13, middle row) to exceed the speeds of the local eigenmodes. (Of course the slow-mode shock simulated in the ideal conditions simulated in Chen, F. et al. (2011), could explain the EUV signal we identify as the flanks of the CME).

Turning to phase speeds directly, we note that in the strong field limit, the fast mode speed does not depend strongly on the orientation angle, θ , between the

propagation direction and local direction of the magnetic field: $c_f \approx \sqrt{v_A^2 + c_s^2 \sin^2 \theta}$. On the other hand the slow mode speed, c_{slow} , varies significantly with orientation in the strong field limit: $c_{slow} \approx c_s \cos \theta$, and goes to zero for perpendicular propagation. In our simulation, a drastic change in the front speed that depends on the orientation of \vec{B} is not observed at any location along the outer propagating front. From the AIA perspective shown in Figures 6.11 and 6.13 the outward propagating front encounters parallel field, while the northern and southern components encounter initially perpendicular field, and all three directions show a similar behavior. The phase relationship identifies a compressible wave for this front (both fast and slow mode waves are compressible), but a slow-mode wave would *not* be able to simultaneously satisfy the isotropic nature that is observed.

6.5.2 A Unified Wave/Non-Wave Picture:

In our analysis of this event 6.4 we find strong evidence supporting the identification of the outer EUV transient observed by AIA and EUVI-A as a fast-mode MHD wave. This should not, however, marginalize the role that the non-linear evolution of the eruption plays in the overall set of EUV signatures that are observed. If say, for arguments sake, that this specific eruption proceeded twice as fast, released twice as much energy, or occurred in a corona with twice the ambient magnetic field strength, then the resulting EUV signature (all fronts) would *most definitely* be altered in some way (in fact we explicitly explore this in Downs et al. (2011)). These mock scenarios are relevant to reality in the sense that the conditions of the corona are never the same for any two events and, as a result, it is not guaranteed to always be the case that a particular scenario will be universally applicable. This implies that the relative contribution of the outer wave component and inner CME component

will likely depend highly on the specific conditions and eruption mechanism for every event. Clearly if the size and speed of the erupting region approaches that of the fast-mode wave front then the two features will become difficult to distinguish (e.g. Run A in Downs et al. (2011)). All-in-all this reinforces the need for a broad perspective and when considering possible EUV wave mechanisms and that considerations of *specific, and realistic* conditions for *each* event are extremely important. In the event studied here we are able to clearly identify and separate the fast-mode wave responsible for the EUV wave from the strong currents and CME evolution that also provide an EUV signal, but this may not always be the case for future events that will be captured by AIA or other future observing facilities.

Along these lines we promote a combined wave/non-wave picture of EUV wave transients, one where the outer EUV front is initially driven by the solar eruption, but later becomes a freely propagating fast-magnetosonic wave. The unique, event specific evolution of the solar eruption however will continue to produce some observable features in the EUV (this is the same scenario discussed in Cohen et al. (2009); Patsourakos et al. (2009); Patsourakos & Vourlidas (2009); Downs et al. (2011)). Surely a fast-mode wave will exist on some level when the corona is perturbed (perturbed strongly in the case of CMEs) because fast-magnetosonic waves are a primary means of information transport across field lines in a magnetized plasma. Additionally fast-mode waves *by their very nature* conveniently satisfy the global, perpendicularly propagating nature of observed EUV wave transients, without relying on a particular set of constraints on the ambient conditions. This is quite compelling as it relaxes the need for the various ‘non-wave’ mechanisms to require that the CME/coronal arcade possess physical extents of a solar radii or more relatively close to the surface, a significant physical difficulty for the basic models of CMEs. But the fast-mode wave cannot fulfill all observational requirements on its own! Some

events, such as the slowest reported waves (50 – 200 km/s), and features such as extended dimming regions and persistent brightenings simply cannot be described by fast-mode waves. Here the non-wave, non-linear evolution of the event itself saves the day by bringing a slew of non-linear mechanisms to the table. With this framework, we theorize that many of the slowest reported EUV waves (Wills-Davey et al. 2007) were in fact measuring the secondary component of a weak eruption where the initial fast-mode wave was not detectable given pre-AIA instrument and cadence limitations.

Ultimately the strong implications towards EUV mechanisms discussed here are directly borne out of the fact that the AIA instrument and its high cadence, high resolution synoptic observing program offers a new source of unprecedentedly detailed observations with which to study EUV waves. Without a source of strong observational constraint, particularly for events that never occur the exact same way twice, it becomes exceedingly difficult to constrain the theoretical models. Models that all too often are lacking with respect to a rigorous prescription of the mechanisms behind the observable features. To this end we attempt to unify the two, employing a state-of-the-art model and an analysis of cutting edge observations. We model an EUV transient without assuming a-priori a particular theory or explanation, and instead it is plausible connection to observations that gives credence to physical mechanisms identified in the results. Results which, *we hope*, help to eliminate the suspension of disbelief that is sometimes required for physical interpretations when either the model or observations are incomplete.

Chapter 7

Conclusion

With each passing month, year, and decade, our theoretical understandings of solar phenomena are undergoing continuous evolution and refinement. In furthering the inevitable march of this process, it is critical to continue to improve the existing models and validate the new. With this overarching goal, we have undertaken this task on both a generally broad and scientifically focused scope.

In our validation study described in Chapter 4, we use the LC model to study coronal heating by exploring empirical parameterizations in the context of realistic 3D magnetic structures observed in the EUV and soft-X-Rays on 1996 Aug 27. Through direct comparison of synthetic observables to observations (Figure 4.2), we demonstrated that this model can effectively capture the interplay between coronal heating and electron heat conduction. Furthermore, we showed that this interplay strongly governs the details of important structures in the low corona, effects not easily characterized with ideal MHD, or magnetic extrapolations on their own.

Next, for the meat of the dissertation, we sharpen our focus to a specific scientific goal: harnessing the LC model towards the understanding of the fundamental physical nature of EUV waves. Here the coupled observational and modeling approach plays

an important role, effectively bridging a critical gap between observations that are unexplained and models whose observable consequences cannot be verified.

In Chapter 5, using the LC model as an effective digital laboratory, we simulate the time-dependent observational signature of four different versions of a realistic solar eruption. We explore the effect of three key parameters on the resulting observational signal of the EUV transient (ambient magnetic field, eruption strength, eruption handedness). Through this characterization and the subsequent interpretation of the results through the lens of *observable* features, we find evidence that there is more to the story than either a ‘pure’ MHD wave or no wave at all. In fact both of these features are complex and, as we document, depend significantly on the unique properties of the eruption!

We conclude with the results of our definitive case-study on the 2010 June 13 event in Chapter 6. Here the rich observational capabilities of the AIA instrument allow our approach to shine. In our simulation we are able to definitively separate the wave and non-wave components by examining both the linear and non-linear components of the eruption and global transient. Along these lines we promote a unified wave/non-wave picture of EUV wave transients, *one where the outer EUV front is initially driven by the solar eruption, but later becomes a freely propagating fast-magnetosonic wave*. Although this is a fine result in its own right, it is the subsequent direct comparison to observations that solidifies its applicability to the real world, allowing us to place the relevance of our results within the greater context of the many EUV wave theories. Ultimately, it is our belief that the coupled observation and modeling analysis approach, such as the one taken here, is poised to make great strides in understanding complex solar phenomena over the next decade.

Chapter 8

Extensions and Future Work

In Chapter 4, we document our efforts to greatly extend the utility of a global 3D MHD model to the study of the low solar corona (the LC model). It was of critical importance that the methods implemented be generally applicable to a variety of scientific avenues, not just limited to the study of EUV waves. This is particularly true for the observational synthesis methods, which give the user ability to generate the expected output for *any* coronal observable that can be parameterized as a function of position and MHD variables (observables from 6 separate spacecraft were used in this work for example). We briefly discuss current and potential future applications of the LC model below.

One completely different observation modeling application of the LC model is to study ground based coronagraph imaging observations of polarized light. Polarization measurements of the magnetic field signal at the surface of the sun have been a routine observation for decades, however only recently have we seen ground based experiments designed to measure polarized light directly in the corona (Lin et al. 2004; Tomczyk et al. 2008). Although an extremely difficult measurement to make and interpret, polarized light in the corona can serve as a direct measurement of magnetic properties in the corona itself, which is typically only inferred through magnetic extrapolations

(as is done in this work). Thanks to tools provided by the High Altitude Observatory¹, we have begun exploring the generation of synthetic polarization intensity images for the Fe XIII 10747 Å line in the near infrared, one of the lines now routinely observed by the Coronal Multichannel Polarimeter (CoMP) instrument (Tomczyk et al. 2008). Using a spectral synthesis package for Fe XIII 10747 Å to generate the images (Casini & Judge 1999), we show in Figure 8.1 synthetic polarization images generated from the coronal conditions simulated for 13 June 2010 (Chapter 6) and compare them to the derived coronal structure in the model. As is clearly visible, the LOS convolution of magnetic field information in polarized light makes for a highly structured signal, even for what appear to be smooth structures in intensity (scattered light) images. As is discussed in Liu & Lin (2008) the interpretation and/or inversion of coronal polarization measurements requires a significant amount of effort, and goes hand in hand with leveraging extrapolations or estimates of the 3D magnetic structure and thermodynamic conditions of the corona. By definition the LC model provides this information as model output. As a result, we envision a potential application wherein polarized light model and observation comparisons can be used to both refine and constrain the LC model parameters while at the same time aid interpreting the complex signals and structures that are presented in the actual observations.

In a broader sense, a key benefit of leveraging the flexible framework of the SWMF to develop the LC model is the large user base of researchers familiar with its methods. Other, non-EUV wave applications of the LC model and methods by other researchers include:

¹FORWARD: a general IDL package for the forward modeling of coronal observables from models: <http://people.hao.ucar.edu/sgibson/FORWARD/>

- A study of the role of reconnection in determining the final orientation and connectivity of an erupting flux-rope (Cohen et al. 2010)².
- A detailed account of the complex interaction of an erupting CME with nearby unipolar field (Lugaz et al. 2011). Here the extended EUV dimming was reproduced and confirmed to be related to the changing connectivity as the event progressed.
- A non-Solar application on stellar coronae, one aimed determining the effect of limited spatial resolution of stellar surface magnetic field maps on MHD wind and coronal X-ray emission (Garraffo et al. 2011).

We hope that these applications represent the beginning of a rich and fruitful application of the LC model and its associated data analysis tools by the broader community.

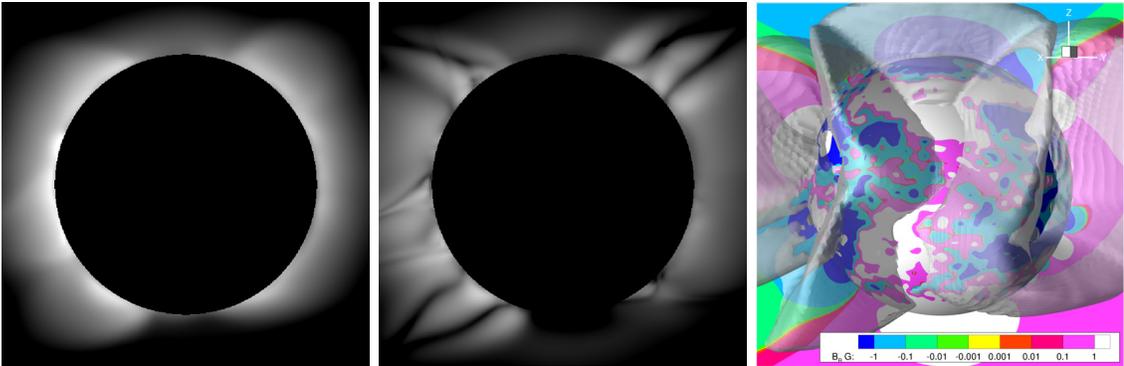


Figure 8.1: Synthetic images of Fe XIII 10747 Å for total intensity (Stokes I, left) and total linear polarization (Stokes P = $\sqrt{Q^2 + U^2}$, middle) for the simulated conditions on 2010 June 13 at 5:30 UT. To give a qualitative sense of how the polarization signal is related to the streamer structures we extract the 3D streamers viewed in front of the plane of the sky, which is the plane normal to the viewing position. Shown are white iso-surfaces of constant loop length ($L = 750$ Mm) and the $R = 1.001 R_{\odot}$ sphere and plane of the sky are colored with contours of the radial magnetic field.

²The full thermodynamic MHD model was not used, however the synthesis of EIT observables was used to frame the evolution at the solar surface.

Future Development of the LC Model

As with any model development project there will always more work to be done. Fortunately, due to the flexible physics modules developed for other applications of the SWMF, we expect the this model to continue to evolve for new and interesting applications. In Chapter 4, for example, we were content to test and formulate simple empirical models for a global coronal heating function. While this is more than appropriate for establishing a baseline model for capturing the ambient conditions of the corona, ideally we would like to further refine this implementation. Fruitful efforts to refine these heating functions that we wish to explore fall under two main categories: enhancing predictive capability, and implementing and testing more physical heating mechanisms.

Predictive Capability: One of the key goals driving heliospheric model development is to provide a suite of models and tools suitable for the forecasting of the changing conditions of the solar wind (a.k.a. Space Weather). In an sense this entails using a model to propagate observations of features and conditions observed near the Sun to the near Earth environment. While existing modules of the SWMF are quite suited for propagating the solar wind and CMEs from the sun to 1AU (see Tóth et al. (2005, 2011) and references therein) it is fundamentally important that the boundary and ambient conditions of the corona be realistic and robust for a range of conditions.

A powerful approach that we have begun to investigate is based on leveraging observational data in order to statistically estimate model parameters; a so-called ‘data assimilation’ approach. With this approach we would no longer need to restrict ourselves to applying a heating function that is user specified. Instead, in general terms, we would aim to drive the local heating rate applied in the model via a

robust data-assimilation method such as the Ensemble Kalman Filter method (EnKF) (see review by Evensen (2003)). At its essence, this method, which is widely used in oceanic and atmospheric sciences uses statistical measures gained through an ensemble Monte Carlo technique and subsequent comparison to data determine the best correction for parameters in a given model. In this application, we can take advantage of the fact that EUV and soft X-ray images provide a detailed snapshot of current conditions in the corona and this emission can be easily calculated within the model—thus providing a framework with which to assess agreement between model and observations. With every successive guided correction, the model relaxes towards the best-fit thermodynamic state and, in doing so, obtains a more realistic description of the actual corona that we observe. Most importantly, with this approach, the key parameter that sets the thermodynamic state of the corona (the local heating rate), is no longer an a-priory assumption of the researcher, but is now a useful output of the model itself. By examining the best fit scenarios for key events and conditions this unique analysis will provide insight into how coronal heating rates vary with magnetic topology and solar cycle.

Of course with any cutting edge research, a paradigm shift such as this; moving from static assumptions to using dynamic data-assimilation to guide the model will require significant effort. One of the major hurdles to this application is that the sheer size and number of computations involved in global 3D models makes ensemble forecasting resource intensive. However, with strategic assumptions and ingenuity in defining the ensemble model (such as mapping the 2D data product to a 2D local heating surface) we feel that this goal can be realistically achieved and will provide a new avenue for research and models of the solar corona.

Towards a Physical Coronal Heating Model As mentioned in Section 2.4 the physical mechanisms responsible for the heating of the corona are still the subject of much debate. A 3D thermodynamic MHD model with the express capability to simulate realistic conditions and observables thus provides an ideal laboratory to test various physical models for coronal heating. Of course the detailed micro physics cannot be resolved on global scales, but successive refinements of their macroscopic contributions can.

One current avenue under exploration for example is the replacement of empirical coronal heating models with a more physically motivated model, such as one involving the turbulent dissipation of Alfvén waves (Sokolov et al. 2009; Cranmer 2010). Because a frequency axis has already been implemented for other applications (Oran et al. 2009; van der Holst et al. 2011) it is possible to reformulate the empirical model of the coronal heating in terms of non-linear wave damping (=cascade). In this effectively 4D model, the evolution of Alfvén wave turbulence frequency can be tracked directly within the model, and various prescriptions for reflection and cascade processes implemented and studied. The evolution of the wave turbulence can also be tracked through the heliosphere via model coupling. Ultimately such a prescription could potentially provide a unique constraint on wave heating mechanisms, requiring models not only to reproduce the heating and structure that is observed in the corona but also the turbulence levels observed in-situ near Earth. Although these type of studies represent a prodigious undertaking, it is the transition from empirical to physical prescriptions of heating that will greatly enhance the physicality and descriptive power of the model on a more fundamental level.

Appendix A

Resolving the Transition Region in a 3D MHD Model

A Dimensional Argument for Equilibrium Length Scales in the Transition Region

While a full stability analysis on the thermodynamics of the transition region is beyond the scope of this document, the picture of the most basic thermodynamic properties and scale of the transition region can be obtained through simple dimensional analysis (see Chapter 4.3 of (Aschwanden 2004) for an extensive review of transition region dynamics). Starting with the assumption that heat conducted from the hot corona above is approximately balanced by the radiative losses of the transition region ($Q_c \sim Q_r$), we can write the 1D balance along a flux tube of constant cross-sectional area as:

$$\nabla \cdot [-\kappa_0 T^{5/2} \hat{B}(\hat{B} \cdot \nabla T)] \sim n_e^2 \Lambda(T_e). \quad (\text{A.1})$$

Now, turning to dimensional analysis and making the substitution ($\nabla \rightarrow 1/L$), where L is the characteristic length scale, this reduces to:

$$\kappa_0 T_e^{5/2} (T_e/L^2) \sim n_e^2 \Lambda(T_e), \quad (\text{A.2})$$

and we obtain an expression of the equilibrium scale, L_{eq} , as a function of n_e and T_e :

$$L_{eq} \sim \sqrt{\frac{\kappa_0 T_e^{7/2}}{n_e^2 \Lambda(T_e)}}. \quad (\text{A.3})$$

As expected we find a strong dependence of the characteristic length scale on the plasma heat conductivity $\kappa = \kappa_0 T_e^{5/2}$. For the relatively low temperatures of the chromosphere the thermal conductivity becomes exceedingly small, requiring a high temperature gradient to make up for this factor. The dependence of L_{eq} on electron temperature and density is illustrated with the contour plot shown in Figure A.1. For transition region temperatures and densities ($10^9 \lesssim n_e \lesssim 10^{11} \text{ cm}^{-3}$ and $5 \times 10^4 \lesssim T_e \lesssim 10^6 \text{ K}$) L_{eq} can be as small as a few kilometers in length, a tremendously small scale, considering it is a factor of 10^5 smaller than the solar radius. It is this property that makes accounting for the transition region within large-scale models of the Sun extremely difficult.

Although at first glance it sounds absurd, the assumption that these two terms balance is not a particularly bad one. First off, for most of the transition region, electron density values are larger than typical coronal values ($n_e \gtrsim 1 \times 10^9 \text{ cm}^{-3}$), making the n_e^2 dependence of the radiative loss term dominate for all but intense local heating values seen in active regions ($Q_h \gtrsim 10^{-4} \text{ ergs cm}^{-3} \text{ s}^{-1}$). Coronal heating serves a key indirect role by heating the plasma in the corona *above* the transition region, which is then converted into downward conductive heat flux but is not always directly

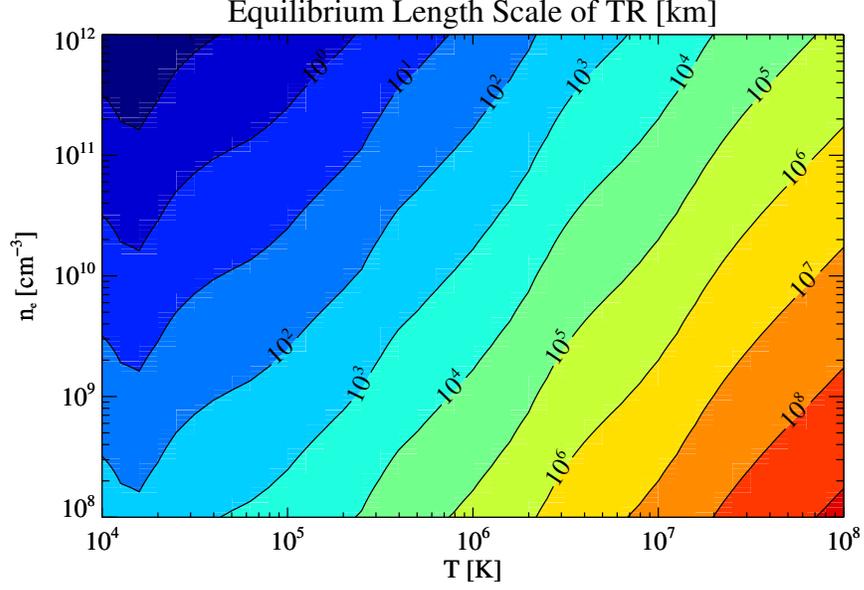


Figure A.1: Length scale contours for heat conduction and radiative loss balance given by Equation A.3.

important in the transition region. The other relevant term is the thermal energy flux of bulk plasma motions along the flux tube, the enthalpy flux:

$$\nabla \cdot \left(\vec{u} \frac{\gamma p}{\gamma - 1} \right). \quad (\text{A.4})$$

Which through dimensional analysis looks like:

$$\frac{U_0}{L_0} \frac{\gamma n_e k_B T_e}{\gamma - 1}. \quad (\text{A.5})$$

Where, U_0 is a characteristic velocity. The inclusion of this term into the balance argument (Equation A.1) produces a quadratic equation for L_0 . But, due to its reduced magnitude for transition region values, the solution is not particularly changed except for large values of U_0 . However, the enthalpy flux does play a key role in the corona for situations where for some reason or another the heat conduction

flux cannot balance radiative losses. For example this occurs for impulsively heated coronal loops in active regions. A heating mechanism brings the loop to high temperatures (2-3 MK) which is stable until the heating process shuts off. As the coronal portion of the loop begins to cool, the conductive flux into the transition falls off and cannot support the original equilibrium. Known as catastrophic cooling, this incites strong upflows of chromospheric material that fill the loop with cool dense plasma in an attempt to balance the deficit through the enthalpy term.

Broadening the Transition Region

Ultimately we need to use this dimensional analysis to derive a feasible set of constraints on the computational resolution for our 3D MHD model if we are to resolve the entire transition region. At the time of writing, including 1 km length scales within a 3D model of the corona is incredibly impractical and borderline insanity. Geometrically this would require on the order of 1000 radial cells in order to resolve the transition alone, and this would be needed over the entire lower boundary of the model. Given that a typical baseline simulation of the SC model in the SWMF is of the order $128 \times 256 \times 128$ (r, ϕ, θ) cells, this is already an order of magnitude increase in simulation size.

But that is the *easy* part! The largest difficulty comes from the time-stepping limits of an explicitly advanced MHD system. Known as the Courant-Friedrichs-Lewy (CFL) condition (Courant et al. 1967) this condition is almost universally applicable to hyperbolic systems and requires that the time-step not exceed the characteristic timescales of the eigenvalues (waves) and diffusion terms (e.g. heat conduction) to maintain stability. For ideal MHD the CFL limit is proportional to the cell size L , and represents the cell crossing time of a particular wave. For heat conduction however, the additional length derivative implies that the CFL condition goes like L^2 .

Assuming a minimum radial length in an ideal MHD simulation of the corona only is typically 10^3 km, adding electron heat conduction and resolving entire transition region would reduce the CFL limit by a factor of a million! The stability issue can be partially alleviated by the use of implicit methods for solving problematic terms (e.g. Tóth et al. (2008); van der Holst et al. (2011)), but accuracy is lost regardless if the explicit timescale is greatly exceeded). Although a factor of a million may not always be significant for some astrophysical systems (the sun will barely notice another million human lifetimes for example) it is *certainly* important when considering a potential Ph.D. project! All joking aside, this hard constraint presents a unique problem if the thermodynamics of the transition are required to be resolved in a global model.

Fortunately a clever solution to this modeling conundrum was developed by Mikić et al. (2006) and its utility demonstrated by Abbett (2007); Lionello et al. (2009). The broadening method aims to increase this length scale for transition region temperatures and densities, while still preserving the total energy budget along the loop. This amounts to artificially increasing the coefficient of thermal conductivity κ while simultaneously reducing by the same amount the radiative loss function. This is achieved functionally by fixing both $\kappa_0 T^{5/2}$ to a constant value of $\kappa_0 T_{mod}^{5/2}$ and reducing the radiative cooling term by the inverse factor $(T/T_{mod}^{5/2})$ for temperatures below a transition region value, $T < T_{mod}$. In this work we use $T_{mod} = 300,000\text{K}$. The effect of this modification on the equilibrium length scale, L_{eq} , is shown in Figure A.2 (see Figure A.1 for comparison). By comparing 3D models with this modification to 1D calculations without, Lionello et al. (2009) demonstrated this method to have little to no effect on final solution in the coronal portion of the simulated domain ($T > 800,000$ K).

The utility of this method is realized from the CFL problem discussed above. By using $T_e^{mod} = 300,000\text{K}$, L_{eq} is on the order of hundreds of kilometers when employing the chromospheric boundary discussed in Section 4.2.3. This generalized grid (Section 4.2.4) still imposes a much stricter CFL limit for the LC model than for the SC model, but it is not nearly as severe. In practice, after factoring in all the additional considerations (extra heating calculations, parallel message passing required for heat conduction, etc.), the total relative computation speed of the LC model is slower by a factor of around 10 to 20 for time-accurate simulations compared to the SC model. A more than acceptable trade-off considering the tremendous increase in descriptive power that is gained. (Note: for local time-stepping mode (Section 5.4) this efficiency difference is a much smaller factor, typically around 3-4.)

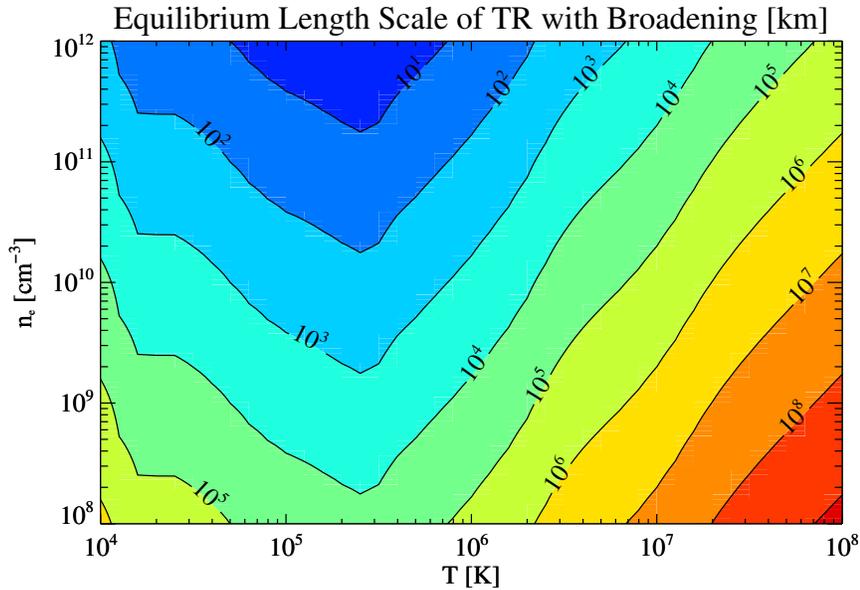


Figure A.2: Length scale contours for heat conduction and radiative loss balance given by the dimensional analysis (Equation A.3) when applying the transition region broadening method. Instead of the slope reversal occurring around $\sim 20,000$ K as it does in the unmodified case (Figure A.1) the reversal (scale increasing with T) occurs at $T = T_{mod} = 300,000\text{K}$. This allows the minimum scale needed in the simulation to be $\sim 50 - 100$ times larger, thus requiring a significantly smaller amount of cells to resolve the transition region (i.e. a feasible number).

Appendix B

Details of EUV image synthesis

As mentioned in Section 4.2.5 the line-of-sight synthesis method involves two main steps: (i) a characterization of detector response based on physical parameters that are calculated in the model and (ii) line-of-sight (LOS) integration through the 3D data set to create synthesized image.

Characterizing the Observable

Formally the blurring effect of an optically thin LOS can be written in the following terms: for a given detector observing an emission line with filter i , this line-of-sight (LOS) integral becomes:

$$R = \int n_e^2(l) f_i(T_e(l), n_e(l)) dl \text{ DN s}^{-1} \quad (\text{B.1})$$

where, $n_e(l)$ and $T_e(l)$ are the electron density and electron temperature at a given point along the LOS, and $f_i(T_e(l), n_e(l))$ is the calculated detector response.

Calculating $f_i(T_e(l), n_e(l))$ folds in two pieces of information. First a synthetic spectrum must be calculated for a unit for every specific density and temperature combination that is to be considered. This is typically done using the CHIANTI

spectral synthesis package (Landi et al. 2006) and it is up to the user to choose a specific set of abundance and ionization equilibrium tabulations. The second piece that must be known is instrument calibration parameters, which dictate how the spectrum is collapsed to a count on the detector CCD. For space based experiments, these calibration parameters are typically provided in some manner by the instrument team (though actually *locating* them can be incredibly difficult!).

A sense for how the EUV spectrum of coronal material changes as a function of temperature and how the effect is realized in imaging telescopes is given in Figure B.1. Calculated synthetic spectra for a parcel of coronal material at temperatures near the peak response of the four EIT filters are overplotted with the transmission functions for each filter, showing the effective spectral window that each probes. Because we are dealing with the EUV regime, it is not possible to make infinitely thin transmission windows and often times a given EUV filter may have additional line contributions that complicate $f_i(T_e(l), n_e(l))$. For example this effect can be seen looking at the broad and sometimes double peaked AIA filter response functions shown in Figure 6.4.

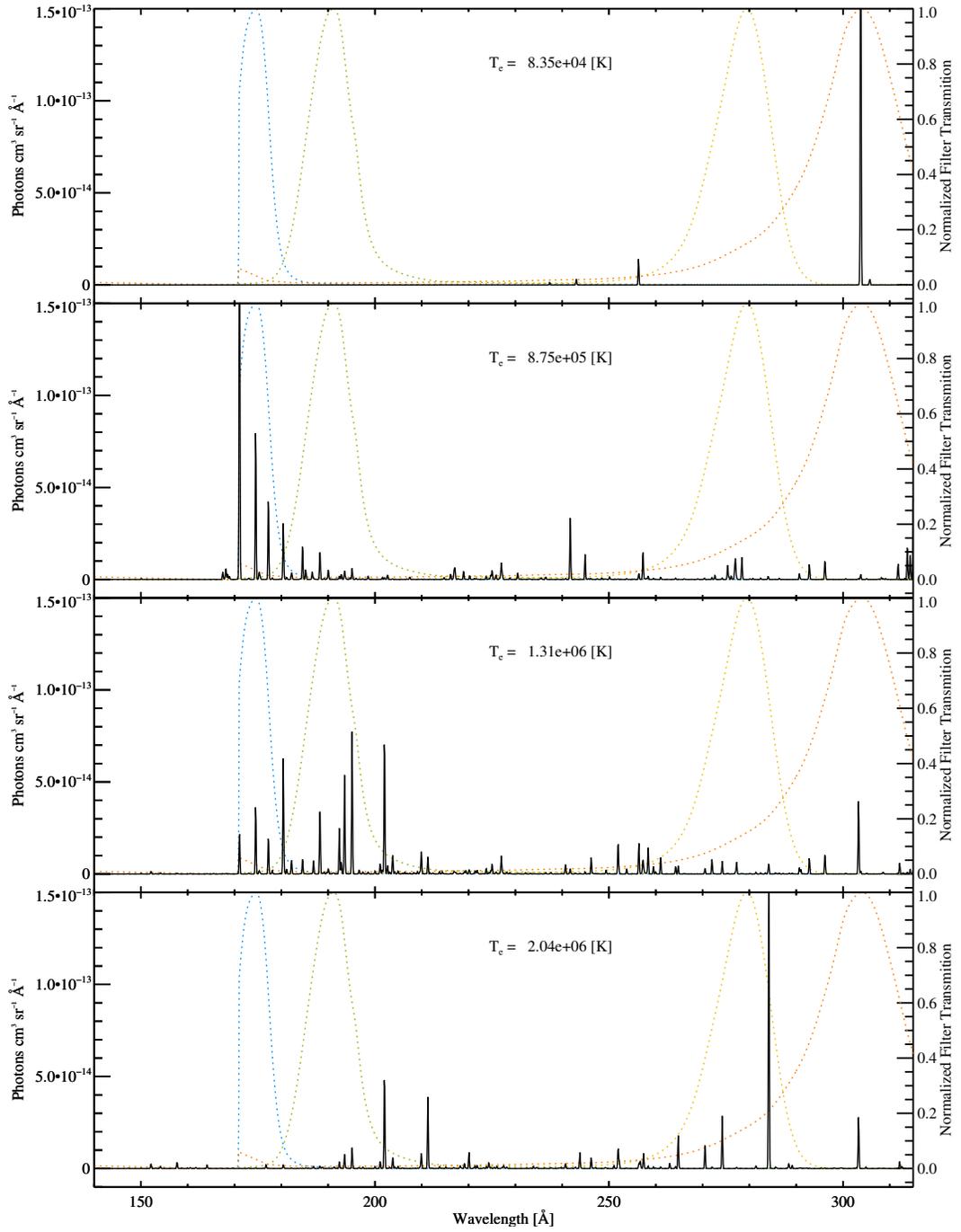


Figure B.1: Calculated synthetic spectra for a parcel of coronal material at temperatures near the peak response of the four EIT filters. Overplotted are the transmission functions for each filter showing the spectral window that it probes EIT 171Å (Blue), 193Å (Green), EIT 284Å (Yellow), and EIT 304Å (Red).

Implementing LOS Integration:

Now that the detector and plasma characterization is complete, the forward modeling step: actually using the model data to calculate an observable, must be implemented. This step will vary depending on the needs of particular model and methods used, and in our case this is implemented directly as a parallelized plot subroutine `write_plot_los` in the SWMF. Illustrated schematically in Figure B.2, this process involves defining the 3D location of the observing satellite in the 3D simulation coordinates and projecting the LOS of each pixel through the domain. Once the each specific LOS is defined, the MHD simulation can be interpolated to points along the LOS and the total emission is integrated along the LOS Equation B.1

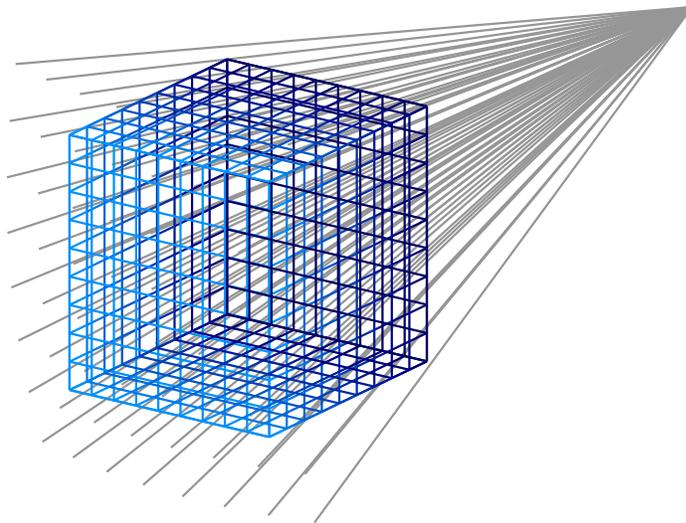


Figure B.2: Schematic illustration of the LOS integration process through a 3D grid described by Equation B.1. The each pixel element on the observing detector describes a unique path (gray) through the computational domain (blue to black). The intersection of the LOS with AMR blocks is calculated and the cell centered MHD values are interpolated to locations along the LOS.

In previous incarnations of this routine, the intersection of the LOS with AMR blocks was calculated for Cartesian geometry only, which greatly simplifies the calculation. However, because of the spherical grid requirement for resolving the

transition region (Section 4.2.4) the calculation had to be generalized for general geometries. For a general grid (e.g. the radially non-uniform (r, ϕ, θ) grid used by the LC model, solution blocks do not define regular planes on the cardinal directions at regular intervals, instead they come in all sizes and orientations. This complicates the determination of whether or not an arbitrary solution block will intersect a given LOS or not. Using a solution from the field of computational geometry (Chapter 21, Press et al. (2007)) we implement a general planar intersection and subsequent triangle bounding check to determine LOS intersection locations. Once two locations are found on a block, the MHD solution is interpolated to the LOS segment and this portion is added to the total integral.

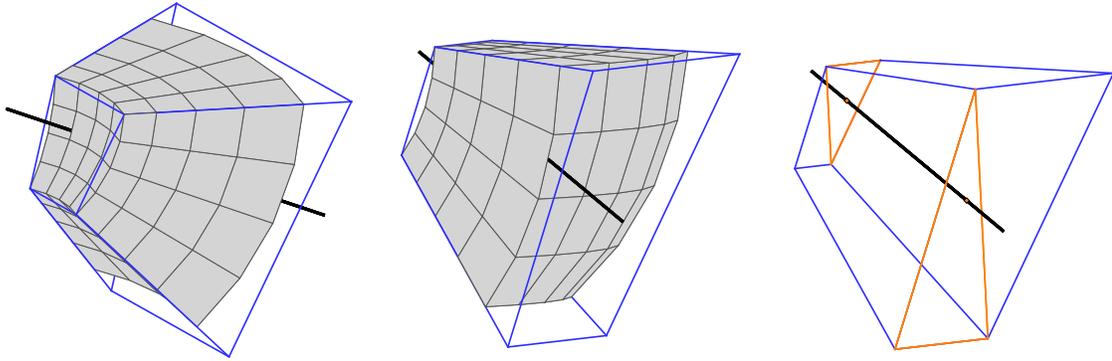


Figure B.3: Diagram showing the LOS intersection method for a general spherical block. A given LOS (black line) intersects a spherical block at an arbitrary angle (gray faces) shown from two different perspectives (right and middle panels). In order to calculate intersection, a bounding set of faces are generated (blue lines) that strictly contain the entire block. Each face is divided into two triangles, each of which is checked for intersection using a general formula to determine if the intersection of the line with the plane defined by the face is in or off of the triangle. The intersected triangles and point of intersection (orange colors) are shown in the right panel.

The Validity of the Steady State Assumption

As for the validity of the assumption of a steady state, optically thin response function, f_i , we benefit greatly due to the nature of low density, high temperature plasmas. As well described in the review by Mason & Fossi (1994), conditions of coronal plasma are such that collisional excitation and de-excitation processes are generally much faster than ionization and recombination timescales for the ions. Furthermore, the strong bound-bound allowed electric dipole transitions that are responsible for the strong EUV emission lines that are commonly observed and dominate the radiative loss calculation can be treated in the so called ‘coronal model approximation’. In this approximation the statistical equilibrium calculation for a given transition reduces to a two level system, greatly simplifying the problem.

A sense of the timescales relevant to the system is given in Figure B.4, which shows the collisional excitation and de-excitation timescales for the Fe IX 171, Fe XII 193, and Fe XIV 211Å spectral lines (solid lines) and the corresponding ionization and recombination timescales for the respective ions (dashed lines). The rates, R_i [$\text{s}^{-1} \text{cm}^3$], where i denotes a given excitation, de-excitation, ionization, or recombination process, are calculated with the CHIANTI package assuming a constant electron density of $n_0 = 10^8 \text{cm}^{-3}$. The relevant timescale is then expressed as $\tau_i = 1/(R_i n_0)$, which gives an inverse dependence of τ_i on n_0 ¹. This confirms the assumption that collisional excitation process dominate is a good one. As far as observation synthesis and the radiative loss calculation is concerned, in order for steady state assumption of f_i to be appropriate we must have the relevant dynamic timescales that we simulate occur at *larger* timescales than τ_i for a given emission line

¹These excitation/de-excitation rates, R_i , vary quite slowly over the density range of the corona and transition region, meaning that the relative order of magnitude difference between the ionization and recombination rates is roughly preserved

(around 10^1 to 10^2 s). In studying the low corona, we are fortunate that the relatively high density (5×10^7 - 10^9 cm^{-3}) provides small enough recombination timescales that the ion charge states are not yet ‘frozen-out’ as they will eventually become in the low-density solar wind.

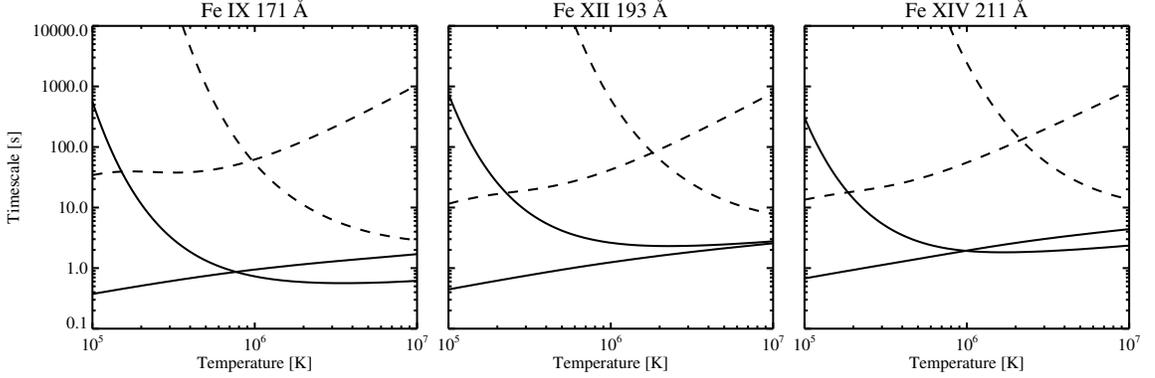


Figure B.4: Collisional excitation and de-excitation timescales for the Fe IX 171, Fe XII 193, and Fe XIV 211Å spectral lines (solid lines) and the corresponding ionization and recombination timescales for the respective ions (dashed lines). Excitation and ionization timescales decrease with temperature while the de-excitation and recombination timescales increase with temperature. The collisional excitation timescales are at least an order of magnitude smaller over the $0.5 < T_e < 2.0$ MK regime relevant to our study. The calculation is for $n_0 = 10^8 \text{ cm}^{-3}$.

Dynamic timescales relative to the system are the radiative loss rate, thermal conduction timescale, the flow characteristics (i.e. are the fluid conditions changing faster than τ_i ?), and the wave characteristics. Orders of magnitude for these timescales can be calculated assuming some macroscopic parameters for the system, L_0 , V_0 , T_0 , n_0 , which characterize typical length scales (uniformity), velocity, temperature, and density. A summary of their dependencies and a value for a chosen set of parameters is given in Table B.1. For the quiescent corona these timescales are far above even the ionization/recombination timescales.

As for the dependencies: first off the ratio $T_e/\Lambda(T_e)$ does not change by more than an order of magnitude between $2 \times 10^4 < T_e < 10^7$ K, implying that the radiative loss

timescale	formula	dependence	value ¹
Radiative Cooling	$n_e k_B T / \Lambda(T) n_e^2$	$T_0 / \Lambda(T) n_0$	3.8×10^3 s
Thermal Conduction	$n_e k_B T / \nabla \cdot F_c$	$n_0 L_0^2 / T_0^{5/2}$	1.8×10^2 s
Bulk Flow	$\sim L_0 / V_0$	L_0 / V_0	2×10^3 s
Fast-mode Wave ²	$\sim \lambda_f / c_f$	λ_f / c_f	2.5×10^2 s

¹Assuming $T_0 = 10^6$ K, $n_0 = 10^8$ cm⁻³, $L_0 = 20,000$ km, $v_0 = 10$ km s⁻¹.

²Assuming a fast-mode speed of $c_f = 400$ km s⁻¹ and a wavelength of $\lambda = 10^5$ km.

Table B.1: Brief comparison of dynamic timescales at play in the corona relevant to the steady state EUV synthesis assumptions.

timescale should not present a problem for any density value. The thermal conduction timescale on the other hand, with its L_0^2 dominated dependence, can in fact present a difficulty as we approach transition region length scales ($200 < L_0 < 2000$ km even with broadening). In addition to forcing the simulation to advance extremely slowly (appendix A) this implies that a steady state radiative loss term will not be completely physical for time-dependent changes in the transition region (i.e. temperature changes are occurring faster than the ions can equilibrate). However, this is not an issue for the initial calculation of pre-event conditions, which produces a roughly steady state corona. For time-dependent eruption simulations this will present a small effect in the coronal portion of the solution; in effect slightly altering the re-equilibration energy balance at the base of the corona after a wave/CME has passed (however this is something that we do not claim to be well reproduced anyway).

For bulk flow we have a similar case to the thermal conduction issue. Typical values of L_0 and V_0 for coronal flows outside of the fastest CMEs imply that bulk temperature and density change far slower than the recombination/ionization timescales. However, in the transition region (smaller L_0) strong flows due to transient upflows/downflows and/or explosive events can in fact produce measurable departures for ionization equilibrium (e.g. Rousev et al. (2001); Rousev & Galsgaard (2002)).

For our study, this presents same post-eruption energy balance issue as discussed above, but we view it as a most necessary trade-off considering the large increase in complexity and simulation time when implementing a non-equilibrium ionization rate calculation within a global 3D MHD model.

Lastly, concerning ourselves with the EUV signal produced by fast-mode waves, we are saved by the effectively large wavelength of the EUV waves. An order of magnitude analysis of the peak in Figure 6.9 or the width of a full wavelength in Figure 6.13 gives an estimate of $\lambda_0 \sim 0.15\text{-}0.2 R_\odot \sim 1\text{-}1.3 \times 10^5$ km. This allows ample time for the material to respond to the small 0.5–3% temperature perturbation imposed by the EUV wave even for the conservative estimates of c_f and λ_0 given in B.1. Of course this would not be true for short wavelength fast-mode waves or those traveling much faster, such as those propagating in the vicinity of active regions and/or coronal holes ($c_f > 1, 500$ km s⁻¹). Such a wave might imply non-equilibrium ionization effects altering the observed signal. An investigation of these types of waves (e.g. the 2000 km s⁻¹ waves observed by AIA following an eruption reported by Liu et al. (2011)) might rely on incorporating these effects into the LC model.

Appendix C

Interpreting synthesized EUV images from 3D models

One critical caveat when imaging the solar corona is that remote sensing images are fundamentally ambiguous in the sense that they are 2D realizations of a fully 3D, optically thin data set. For our purposes, it is best to frame the problem with the concepts of modeling an unresolved Differential Emission Measure (DEM) distribution and Hydrostatic Weighting Bias, well described in Aschwanden & Nitta (2000); Aschwanden & Acton (2001). These issues arise due to two main facts. (i) The spatial resolution of current imaging instruments (e.g. TRACE, SOHO, STEREO) all lie below the fundamental width of an isolated flow/field line. And (ii) any image is a line of sight integral over a range of heights, which are preferentially biased towards hotter flow lines with longer density scale heights. Thus at further distance off of the limb, the observation may be biased towards flow lines that may not be energetically important at the surface. Local DEM distributions can also be directly observed through coupled filter and tomographic inversions (Frazin et al. 2009).

Though the LOS integral for image synthesis Equation 4.5 includes the range of temperatures and densities in cells along the line of sight, it cannot fundamentally

account for the DEM distribution that is below the physical resolution of the model. In MHD, a given cell has a unique value for its thermodynamic properties, particularly n_e , and T , while a physical picture of the low β multi-hydrostatic corona below the resolution limit can be treated as a superposition of densities and temperatures, each confined to an isothermal flow/field line. In this sense, the true DEM distribution of a parcel of gas that contributes to an EUV image (e.g. the EIT instrument) is instead represented as a delta function in the simulation. One aspect of this limitation can be seen in difference between the data and synthesized limb profiles (Figure 4.7). Because the observational weighting bias shifts to higher temperatures further with distance from the surface, the observed limb profile cannot be represented in all four filters simultaneously with only the larger scale temperature equilibrium produced by the MHD model.

To further examine this issue in the context of the LC model we use filter ratios between the EUV images, which are nominally sensitive to temperature differences. In Figure C.1 we show filter ratio values for SOHO EIT observations on 1996 Aug 27 and the path in the filter ratio plane spanned by all possible filter ratios of the optically thin response functions $f_{195}(T, n_e)/f_{171}(T, n_e)$ and $f_{284}(T, n_e)/f_{195}(T, n_e)$ (Section 4.2.5). Unsurprisingly, the EUV data spans a much larger range than that allowed by a single temperature. To simply examine the effect that an unresolved DEM distribution may have on the synthesis and subsequent comparison to observational data we construct an ad hoc DEM by Gaussian convolution of the filter response functions with T:

$$f_i^{mod}(T_0, n_e) = \frac{1}{\sqrt{\pi}\sigma_T} \int_{10^4}^{10^7} f_i(T, n_e) e^{-\frac{(T-T_0)^2}{\sigma_T^2}} dT \quad (C.1)$$

and use $\sigma_T = 0.5T_0$ for this discussion. While we by no means posit that this DEM distribution should resemble the corona everywhere, it includes the basic temperature splitting features of those gaussian DEM distributions calculated from observations (e.g. Aschwanden & Acton (2001); Frazin et al. (2009)). We also show the effect of this modification in the right panel of Figure C.1.

The effect that this simple induced DEM distribution has on the synthesized ratios is shown in Figure C.2. It is clear comparing the limb tracks of the synthesized images to the temperature tracks in Figure C.1 that the LOS synthesis at the current model resolution does not produce a significant DEM distribution on its own (particularly at the limb). However, the improvement gained in terms of the relative location with respect to observations for the modified DEM synthesis suggests that this effect should not be overlooked when constructing more detailed models in the future. High resolution studies designed to approach the fundamental scale of isothermal separation between coronal loops, particularly those involving local, time-dependent heating for example, should be able to address this fundamental issue.

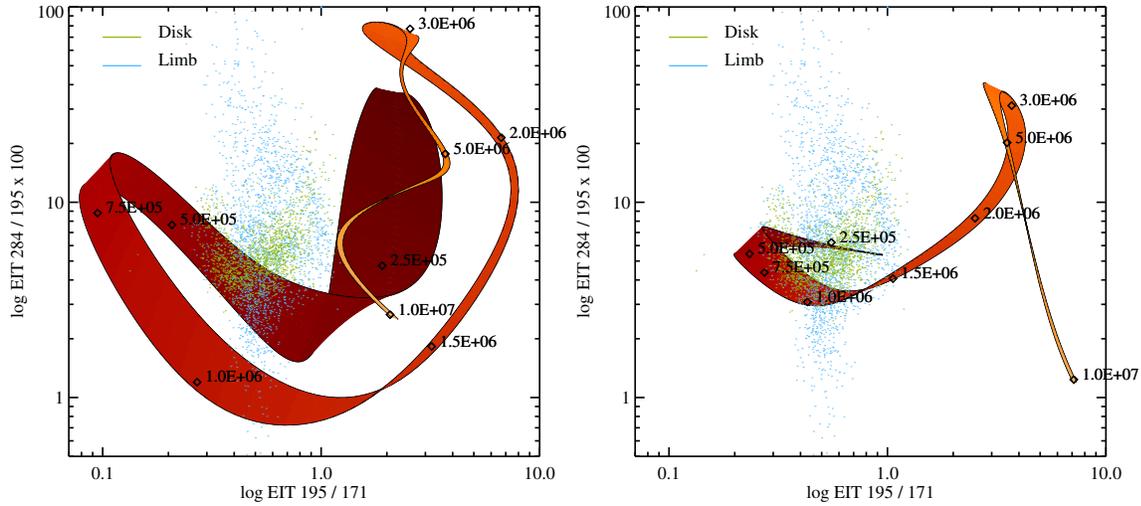


Figure C.1: EIT filter ratio path with no DEM modification (left) and ratio path with Gaussian convolution of response with $\sigma_T = 0.5T_0$ (right). The blue and green points represent EUV data on an off the limb (binned to 1000 points each). The curve path follows the ratio values $[f_{195}(T, n_e)/f_{171}(T, n_e)$ and $f_{284}(T, n_e)/f_{195}(T, n_e)]$ from $T = 2.5 \times 10^5 - 10^7$ K, the width of the curves represents the variation of the ratio values from $n_e = 1 \times 10^{6-12} \text{cm}^{-3}$ at a given temperature. This is intended to illustrate the large variation of filter ratio values with respect to an unresolved DEM distribution.

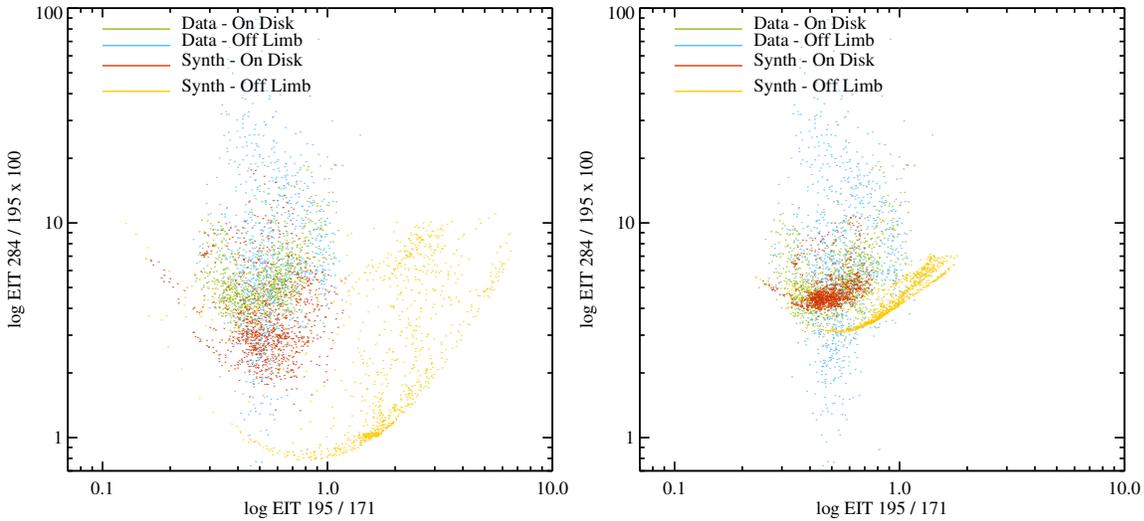


Figure C.2: Effect of simple DEM modification on the synthesized EIT filter ratios for Run D. LOS synthesis ratios with no DEM modification (left) and those with Gaussian convolution of response with $\sigma_T = 0.5T_0$ (right). While the location of the synthesized filter ratios improves with this DEM modification, the fine details of the local DEM distribution, realized by the variation of observed EIT filter ratio values, are difficult to reproduce with an MHD model involving large, global scales.

References

- Abbett, W. P. 2007, *Astrophysical Journal*, 665, 1469
- Alfvén, H. 1942, *Nature*, 150, 405
- Altschuler, M. D., Levine, R. H., Stix, M., & Harvey, J. 1977, *Solar Physics*, 51, 345
- Amari, T., Luciani, J. F., Mikić, Z., & Linker, J. 1999, *Astrophys. J. Lett.*, 518, L57
- Antiochos, S. K., Devore, C. R., & Klimchuk, J. A. 1999, *Astrophys. J.*, 510, 485
- Archontis, V., Moreno-Insertis, F., Galsgaard, K., Hood, A., & O’Shea, E. 2004, *Astronomy and Astrophysics*, 426, 1047
- Arge, C., Luhmann, J., Odstreil, D., Schrijver, C., & Li, Y. 2004, *Journal of Atmospheric and Solar-Terrestrial Physics*, 66, 1295
- Aschwanden, M. J. 2004, *Physics of the Solar Corona. An Introduction* (Springer)
- . 2009, *Annales Geophysicae*, 27, 3275
- Aschwanden, M. J., & Acton, L. W. 2001, *Astrophysical Journal*, 550, 475
- Aschwanden, M. J., Alexander, D., Hurlburt, N., Newmark, J. S., Neupert, W. M., Klimchuk, J. A., & Gary, G. A. 2000, *Astrophysical Journal*, 531, 1129
- Aschwanden, M. J., & Nitta, N. 2000, *Astrophysical Journal Letters*, 535, L59
- Aschwanden, M. J., Nitta, N. V., Wuelser, J., Lemen, J. R., Sandman, A., Vourlidas, A., & Colaninno, R. C. 2009, *Astrophysical Journal*, 706, 376
- Aschwanden, M. J., & Schrijver, C. J. 2002, *Astrophysical Journal Supplement*, 142, 269
- Attrill, G. D. R. 2010, *Astrophysical Journal*, 718, 494+
- Attrill, G. D. R., Engell, A. J., Wills-Davey, M. J., Grigis, P., & Testa, P. 2009, *Astrophysical Journal*, 704, 1296+

- Attrill, G. D. R., Harra, L. K., van Driel-Gesztelyi, L., & Démoulin, P. 2007a, *Astrophysical Journal Letters*, 656, L101
- Attrill, G. D. R., Harra, L. K., van Driel-Gesztelyi, L., Démoulin, P., & Wülser, J.-P. 2007b, *Astronomische Nachrichten*, 328, 760
- Aulanier, G., Török, T., Démoulin, P., & DeLuca, E. E. 2010, *Astrophysical Journal*, 708, 314
- Bercik, D. J., Fisher, G. H., Johns-Krull, C. M., , & Abbett, W. P. 2005, *Astrophysical Journal*, 631, 529
- Biesecker, D. A., Myers, D. C., Thompson, B. J., Hammer, D. M., & Vourlidas, A. 2002, *Astrophysical Journal*, 569, 1009
- Boerner, P., et al. 2011, *Solar Physics*, 193
- Braginskii, S. I. 1965, *Reviews of Plasma Physics*, 1
- Casini, R., & Judge, P. G. 1999, *Astrophysical Journal*, 522, 524
- Chen, P. F. 2011, *Living Reviews in Solar Physics*, 8, 1
- Chen, P. F., Fang, C., & Shibata, K. 2005, *Astrophysical Journal*, 622, 1202
- Chen, P. F., Wu, S. T., Shibata, K., & Fang, C. 2002, *Astrophysical Journal Letters*, 572, L99
- Chen, F., Ding, M. D., Chen, P. F., & Harra, L. K. 2011, ArXiv e-prints
- Cohen, O., Attrill, G. D. R., Manchester, W. B., & Wills-Davey, M. J. 2009, *Astrophysical Journal*, 705, 587
- Cohen, O., Attrill, G. D. R., Schwadron, N. A., Crooker, N. U., Owens, M. J., Downs, C., & Gombosi, T. I. 2010, *Journal of Geophysical Research*, 115
- Cohen, O., Sokolov, I. V., Roussev, I. I., & Gombosi, T. I. 2008, *Journal of Geophysical Research*, 113, A03104
- Cohen, O., et al. 2007, *Astrophysical Journal Letters*, 654, L163
- Courant, R., Friedrichs, K., & Lewy, H. 1967, *IBM Journal of Research and Development*, 11, 215
- Cranmer, S. R. 2010, *Astrophysical Journal*, 710, 676
- Dai, Y., Auchere, F., Vial, J. C., Tang, Y. H., & Zong, W. G. 2010, *Astrophysical Journal*, 708, 913

- De Pontieu, B., et al. 2007, *Science*, 318, 1574
- Delaboudinière et al. 1995, *Solar Physics*, 162, 291
- Delannée, C. 2009, *Astronomy and Astrophysics*, 495, 571
- Delannée, C., Török, T., Aulanier, G., & Hochedez, J. F. 2008, *Solar Physics*, 247, 123
- Downs, C., Roussev, I. I., van der Holst, B., Lugaz, N., Sokolov, I. V., & Gombosi, T. I. 2010, *Astrophysical Journal*, 712, 1219
- . 2011, *Astrophysical Journal*, 728, 2
- Eparvier, F. G., et al. 2004, in *Society of Photo-Optical Instrumentation Engineers (SPIE) Conference Series*, Vol. 5660, *Society of Photo-Optical Instrumentation Engineers (SPIE) Conference Series*, ed. C. A. Nardell, P. G. Lucey, J.-H. Yee, & J. B. Garvin, 48–55
- Evensen, G. 2003, *Ocean Dynamics*, 53, 343
- Fan, Y. 2008, *Astrophysical Journal*, 676, 680
- Frazin, R. A., Jacob, M., Manchester, W. B., Morgan, H., & Wakin, M. B. 2009, *Astrophysical Journal*, 695, 636
- Freeland, S. L., & Handy, B. N. 1998, *Solar Physics*, 182, 497
- Gallagher, P., & Long, D. 2010, *Space Science Reviews*, 1
- Garraffo, C., Cohen, O., Drake, J. J., & Downs, C. 2011, in *American Astronomical Society Meeting Abstracts #218*, 407.01–+
- Gopalswamy, N., et al. 2009, *Astrophysical Journal Letters*, 691, L123+
- Gosling, J. T., Bame, S. J., Mccomas, D. J., & Phillips, J. L. 1990, *Geophysics Research Letters*, 17, 901
- Groth, C. P. T., De Zeeuw, D. L., Gombosi, T. I., & Powell, K. G. 2000, *Journal of Geophysical Research*, 105, 25,053
- Howard, R. A., et al. 2008, *Space Science Reviews*, 136, 67
- Jacobs, C., Roussev, I. I., Lugaz, N., & Poedts, S. 2009, *Astrophysical Journal Letters*, 695, L171
- Kaiser, M. L., Kucera, T. A., Davila, J. M., St, Guhathakurta, M., & Christian, E. 2008, *Space Science Reviews*, 136, 5

- Khan, J. I., & Aurass, H. 2002, *Astronomy and Astrophysics*, 383, 1018
- Klassen, A., Aurass, H., Mann, G., & Thompson, B. J. 2000, *Astronomy and Astrophysics Supplement*, 141, 357
- Kozarev, K. A., Korreck, K. E., Lobzin, V. V., Weber, M. A., & Schwadron, N. A. 2011, *Astrophysical Journal Letters*, 733, L25+
- Landi, E., Feldman, U., & Dere, K. P. 2002, *Astrophysical Journal Supplement*, 139, 281
- Landi, E., Zanna, D. G., Young, P. R., Dere, K. P., Mason, H. E., & Landini, M. 2006, *Astrophysical Journal Supplement*, 162, 261
- Lemen, J. R., et al. 2011, *Solar Physics*, 172
- Lin, H., Kuhn, J. R., & Coulter, R. 2004, *Astrophysical Journal Letters*, 613, L177
- Lionello, R., Linker, J. A., & Mikic, Z. 2001, *Astrophysical Journal*, 546, 542
- Lionello, R., Linker, J. A., & Mikic, Z. 2009, *Astrophysical Journal*, 690, 902
- Liu, W., Title, A. M., Zhao, J., Ofman, L., Schrijver, C. J., Aschwanden, M. J., Pontieu, B. D., & Tarbell, T. D. 2011, *Astrophysical Journal Letters*, 736, L13+
- Liu, Y., & Lin, H. 2008, *Astrophysical Journal*, 680, 1496
- Long, D. M., Gallagher, P. T., McAteer, R. T. J., & Bloomfield, D. S. 2008, *Astrophysical Journal Letters*, L81+
- Low, B. C. 2010, *Solar Physics*, 266, 277
- Lugaz, N., Downs, C., Shibata, K., Roussev, I. I., Asai, A., & Gombosi, T. I. 2011, *Astrophysical Journal*, 738, 127
- Lugaz, N., Vourlidas, A., Roussev, I., & Morgan, H. 2009, *Solar Physics*, 256, 269
- Lugaz, N., Vourlidas, A., Roussev, I. I., Jacobs, C., Manchester, & Cohen, O. 2008, *Astrophysical Journal Letters*, 684, L111
- Ma, S., Raymond, J. C., Golub, L., Lin, J., Chen, H., Grigis, P., Testa, P., & Long, D. 2011, *Astrophysical Journal*, 738, 160
- Ma, S., et al. 2009, *Astrophysical Journal*, 707, 503
- Manchester, Gombosi, T., Dezeew, D., & Fan, Y. 2004, *Astrophysical Journal*, 610, 588
- Mason, H. E., & Fossi, B. C. M. 1994, *Astronomy and Astrophysics Review*, 6, 123

- McIntosh, S. W., de Pontieu, B., Carlsson, M., Hansteen, V., Boerner, P., & Goossens, M. 2011, *Nature*, 475, 477
- Mikić, Z., Linker, J. A., Schnack, D. D., Lionello, R., & Tarditi, A. 1999, *Physics of Plasmas*, 6, 2217
- Mikić, Z., Linker, J. A., Titov, V., Lionello, R., & Riley, P. 2006, SHINE Workshop (San Diego: SHINE), http://shadow.adnc.net/shine/Presentations/2006/CampaignEvents/CE1_May97/ZM/Mikic_SHINE_2006.pdf
- Mok, Y., Mikić, Z., Lionello, R., & Linker, J. A. 2005, *Astrophysical Journal*, 621, 1098
- Mok, Y., Mikić, Z., Lionello, R., & Linker, J. A. 2008, *Astrophysical Journal Letters*, 679, L161
- Moses, D., et al. 1997, *Solar Physics*, 175, 571
- O'Dwyer, B., Zanna, G. D., Mason, H. E., Weber, M. A., & Tripathi, D. 2010, *Astronomy and Astrophysics*, 521, A21+
- Olmedo, O., & Zhang, J. 2010, *Astrophysical Journal*, 718, 433
- Oran, R., Sokolov, I. V., Roussev, I. I., Van Der Holst, B., Manchester, W. B., & Gombosi, T. I. 2009, in *Astronomical Society of the Pacific Conference Series*, Vol. 406, *Numerical Modeling of Space Plasma Flows: Astronom-2009 Proceedings of the 2nd International Conference*, ed. N. V. Pogorelov, E. Audit, P. Colella, & G. P. Zank
- Parker, E. N. 1958, *Astrophysical Journal*, 128
- Parker, E. N. 1972, *Astrophysical Journal*, 174, 499
- Parker, E. N. 1988, *Astrophysical Journal*, 330, 474
- Patsourakos, S., & Vourlidas, A. 2009, *Astrophysical Journal Letters*, 700, L182
- Patsourakos, S., Vourlidas, A., & Kliem, B. 2010a, *Astronomy and Astrophysics*, 522, A100+
- Patsourakos, S., Vourlidas, A., & Stenborg, G. 2010b, *Astrophysical Journal Letters*, 724, L188+
- Patsourakos, S., Vourlidas, A., Wang, Y. M., Stenborg, G., & Thernisien, A. 2009, *Solar Physics*, 259, 49
- Pevtsov, A. A., Fisher, G. H., Acton, L. W., Longcope, D. W., Johns-Krull, C. M., Kankelborg, C. C., & Metcalf, T. R. 2003, *Astrophysical Journal*, 598, 1387

- Powell, K. 1999, *Journal of Computational Physics*, 154, 284
- Press, W. H., Teukolsky, S. A., Vetterling, W. T., & Flannery, B. P. 2007, *Numerical Recipes 3rd Edition: The Art of Scientific Computing*, 3rd edn. (New York, NY, USA: Cambridge University Press)
- Rochus, P. L., et al. 2004, in Presented at the Society of Photo-Optical Instrumentation Engineers (SPIE) Conference, Vol. 5171, Society of Photo-Optical Instrumentation Engineers (SPIE) Conference Series, ed. S. Fineschi & M. A. Gummin, 53–64
- Roussev, I., Doyle, J. G., Galsgaard, K., & Erdélyi, R. 2001, *Astronomy and Astrophysics*, 380, 719
- Roussev, I., & Galsgaard, K. 2002, *Astronomy and Astrophysics*, 383, 697
- Roussev, I. I., Forbes, T. G., Gombosi, T. I., Sokolov, I. V., Dezeeuw, D. L., & Birn, J. 2003a, *Astrophysical Journal Letters*, 588, L45
- Roussev, I. I., Lugaz, N., & Sokolov, I. V. 2007, *Astrophysical Journal Letters*, 668, L87
- Roussev, I. I., Sokolov, I. V., Forbes, T. G., Gombosi, T. I., Lee, M. A., & Sakai, J. I. 2004, *Astrophysical Journal Letters*, 605, L73
- Roussev, I. I., et al. 2003b, *Astrophysical Journal Letters*, 595, L57
- Schmidt, J. M., & Ofman, L. 2010, *Astrophysical Journal*, 713, 1008
- Schnack, D. D. 2009, *Lectures in Magnetohydrodynamics: With an Appendix on Extended MHD* (Springer)
- Schrijver, C. J., Aulanier, G., Title, A. M., Pariat, E., & Delannée, C. 2011, *Astrophysical Journal*, 738, 167
- Schrijver, C. J., Sandman, A. W., Aschwanden, M. J., & Derosa, M. L. 2004, *Astrophysical Journal*, 615, 512
- Sheeley, N. R., et al. 2008, *Astrophysical Journal Letters*, 674, L109
- Sokolov, I. V., Roussev, I. I., Skender, M., Gombosi, T. I., & Usmanov, A. V. 2009, *Astrophysical Journal*, 696, 261
- Spitzer, L. 1965, *Physics of fully ionized gases*, 2nd rev. ed. edn. (New York: Interscience Publication)
- Thompson, B. J., et al. 1999, *Astrophysical Journal Letters*, 517, L151

- Titov, V. S., & Démoulin, P. 1999, *Astronomy and Astrophysics*, 351, 707
- Tomczyk, S., et al. 2008, *Solar Physics*, 247, 411
- Tóth, G., Ma, Y., & Gombosi, T. I. 2008, *Journal of Computational Physics*, 227
- Tóth, G., Zeeuw, D. L. D., Gombosi, T. I., & Powell, K. G. 2006, *Journal of Computational Physics*, 217, 722
- Tóth, G., et al. 2005, *Journal of Geophysical Research*, 110, A12226
- . 2011, *Journal of Computational Physics*, In Press, Corrected Proof
- Tsuneta, S., et al. 1991, *Solar Physics*, 136, 37
- Uchida, Y. 1968, *Solar Physics*, 4, 30
- van der Holst et al. 2011, *Astrophysical Journal Supplement*, 194
- Veronig, A. M., Muhr, N., Kienreich, I. W., Temmer, M., & Snak, B. V. 2010, *Astrophysical Journal Letters*, 716, L57
- Veronig, A. M., Temmer, M., & Vršnak, B. 2008, *Astrophysical Journal Letters*, L113+
- Wang, H., Shen, C., & Lin, J. 2009, *Astrophysical Journal*, 700, 1716+
- Warmuth, A., Mann, G., & Aurass, H. 2005, *Astrophysical Journal Letters*, 626, L121
- Wills-Davey, M. J., & Attrill, G. D. R. 2009, *Space Science Reviews*, 149, 325
- Wills-Davey, M. J., Deforest, C. E., & Stenflo, J. O. 2007, *Astrophysical Journal*, 664, 556
- Wills-Davey, M. J., & Thompson, B. J. 1999, *Solar Physics*, 190, 467
- Withbroe, G. L. 1988, *Astrophysical Journal*, 325, 442
- Wu, S. T., Zheng, H., Wang, S., Thompson, B. J., Plunkett, S. P., Zhao, X. P., & Dryer, M. 2001, *Journal of Geophysical Research*, 106, null
- Wuelser, J., et al. 2004, in *Society of Photo-Optical Instrumentation Engineers (SPIE) Conference Series*, Vol. 5171, *Society of Photo-Optical Instrumentation Engineers (SPIE) Conference Series*, ed. S. Fineschi & M. A. Gummin, 111–122
- Yang, H., & Chen, P. 2010, *Solar Physics*, Online First, ISSN 1573-093X